Ultraviolet Photodissociation Dynamics of Small Molecules

Adsorbed on Water Ice Surfaces

（氷表面上に吸着した簡単な分子の紫外光分解）

AKIHIRO YABUSHITA

2002

Ultraviolet Photodissociation Dynamics of Small Molecules

Adsorbed on Water Ice Surfaces

（氷表面上に吸着した簡単な分子の紫外光分解）

Akihiro YABUSHITA

Department of Molecular Engineering
Graduate school of Engineering
Kyoto University

2002

CONTENTS

Chapter 1

General Introduction

The rapid growth currently taking place in the field of the photochemistry of small molecules adsorbed on water ice films is driven by their relevance in atmospheric chemistry[1-13] and astro-chemistry[14-17] as well as by scientific interest in fundamental questions concerning the photochemical reaction mechanisms. For deeper understanding of photochemistry on water ice films, it is also important to understand the ice microstructure and the interaction between an adsorbate and an ice surface.[18-29] Over the past decade, chemistry concerning ice itself or the interaction with adsorbate has been developed due in part to the relevance of surface chemistry to the atmospheric sciences, an area not normally associated with surface science. It has been established that reactions occurring on the surfaces of stratospheric cloud particles play a key role in the formation of the seasonal ozone hole over Antarctica.[30] A deeper understanding of the surface chemical properties of ice would also be valuable for several other areas of study. For instance, particles in dense interstellar dust clouds are believed to be coated with thin overlayers of ice[31] that may serve to mediate important astrophysical chemical processes.[32] Ice surface chemistry and structure may play an important role in the chemical behavior of comets.[33] Additionally, surface interactions between soil particulates and ice play a key role in the phenomenon of forest heave.[34]

The photochemistry of small molecules adsorbed on water ice films are relevant to astro-chemistry, and atmospheric chemistry. One of the major questions in the formation and evolution of condensed-phase molecules in interstellar environments is their production, which may proceed either via grain-surface chemistry of by accretion of simple molecules with subsequent processing by cosmic ray, ultraviolet photons, or a combination of both. Many experiments apply to ices in solar system environments when the ice composition, temperature, or bombarding flux is varied to simulate what is known about each icy-satellite, planetary, or cometary environment.[15] Under

1

atmospheric conditions, according to Honrath et al., NO_x levels in the interstitial air of surface snow in the polar regions are of magnitude 3 to 10 times those in the ambient air.[35] The high level NO_x comes from the solar photochemical reaction of NO_3^- in snow.[10] Dubowski et al. quantify the NO_2 fluxes released into the gas phase during the continuous $\lambda \sim 300$ nm photolysis of NO_3^- in sub-millimeter ice layers produced by freezing aqueous KNO_3 sprays on cold surfaces.[12,13]

The purpose of this study is to understand the nature of interaction between adsorbed molecules and ice surfaces, and the influence of which on the photodissociation dynamics. A powerful way to obtain insight into the dynamics of molecular processes at water ice surfaces involves the determination of translational and internal energy distributions of desorbed product species. Photochemical surface reactions are initiated by the absorption of photons by the adsorbate, and followed by various energy transfer and relaxation processes that eventually lead to nuclear motion along the reaction coordinates. Photofragments can contain large amounts of information in the final state distributions of the various translational and internal degrees of freedom. These include the angular distribution, the translational, vibrational, and rotational energy distributions, and populations of electronic states such as spin-orbit states. Despite this apparent wealth of information, these exist no straightforward way of quantitatively utilizing it to gain direct insight into the reaction mechanism and dynamics. One can often draw qualitative conclusions by comparing the product energy distributions with thermal distributions at the surface temperature or with gas phase photolysis results, or by examining how variations in the experimental conditions affect the final state distributions.

Depending on pressure, temperature, the substrate lattice structure and the angular distribution of incident H_2O flux, water ice on a cold substrate can exist in a number of structurally different forms.[36-43] The preparation of water ice films and their characteristics are presented in the next chapter. In chapter 3, I briefly state the two sets of experimental principles and techniques commonly used to obtain translational energy distributions and populations of electronic states such as spin-orbit states of

photodesorbed species, and adsorption states of small molecules on water ice surfaces. One experimental technique is the state resolved time-of-flight measurement of the photofragments from the photodissociation of small molecules on a water ice film. Another one is the infrared absorption spectroscopic measurement. For the goal of this study to understand the nature of interaction between adsorbed molecules and ice surfaces, and the influence of which on the photodissociation dynamics, four kinds of molecules having different behaviors are selected, which are $CFCl_3$, Cl_2, HCl, and N_2O_4. By using $CFCl_3$, Cl_2, and HCl molecules which have different interaction strength with ice molecules, the influence of the interaction with ice molecules on the photodissociation dynamics have been investigated by measuring the translational energy distributions and the spin-orbit branching ratios of the $Cl(^2P_{3/2})$ and $Cl^*(^2P_{1/2})$ photofragments. These studies are discussed in chapter 4, 5. In chapter 6, 7, it is discussed about the UV photodissociation dynamics of N_2O_4 adsorbed on amorphous and crystalline water ice films by measuring the translational and internal energy distributions of the NO photofragments with photofragment time-of-flight spectroscopy, and the surface adsorbed species on ice by temperature programmed desorption spectroscopy and infrared reflection absorption spectroscopy.

References

(1) Gane, M. P.; Williams, N. A.; Sodeau, J. R. *J. Chem Soc., Faraday Trans.* **1997**, *93*, 2747.

(2) Graham, J. D.; Roberts, J. T.; Anderson, L. D.; Grassian, V. H. *J. Phys. Chem.* **1996**, *100*, 19551.

(3) Pursell, C. J.; Conyers, J.; Denison, C. *J. Phys. Chem.* **1996**, *100*, 15450.

(4) Thomsen, C. L.; Reid, P. J.; Keiding, S. R. *J. Am. Chem. Soc.* **2000**, *122*, 12795.

(5) Peterson, M. C.; Honrath, R. E. *Geophys. Res. Lett.* **2001**, *28*, 511.

(6) Sumner, A. L.; Shepson, P. B. *Nature* **1999**, *398*, 230.

(7) Dubowski, Y.; Hoffmann, M. R. *Geophys. Res. Lett.* **2000**, *27*, 3321.

(8) Peterson, M. C.; Honrath, R. E. *J. Geophys. Res.* **1999**, *104*, 11695.

(9) Honrath, R. E.; Peterson, M. C.; Dziobak, M. P.; Dibb, J. E.; Arsenault, M. A.; Green, S. A. *Geophys. Res. Lett.* **2000**, *27*, 2237.

(10) Honrath, R. E.; Peterson, M. C.; Dziobak, M. P.; Dibb, J. E.; Arsenault, M. A. *J. Geophys. Res.* **2000**, *105*, 24183.

(11) Ogasawara, H.; Kawai, M. *Surf. Sci.* **2002**, *502-503*, 285.

(12) Dubowski, Y.; Colussi, A. J.; Hoffmann, M. R. *J. Phys. Chem. A* **2001**, *105*, 4928.

(13) Dubowski, Y.; Colussi, A. J.; Boxe, C.; Hoffmann, M. R. *J. Phys. Chem. A* **2002**, *106*, 6967.

(14) Chaabouni, H.; Schriver-Mazzuoli, L.; Schriver, A. *Low Temp. Phys.* **2000**, *26*, 712.

(15) Moore, M. H.; Hudson, R. L.; Gerakines, P. A. *Spectrochim. Acta* **2001**, *47A*, 843.

(16) Gerakines, P. A.; Moore, M. H.; Hudson, R. L. *Astron. Astrophys.* **2000**, *357*, 793.

(17) Borget, F. B.; Chiavassa, T.; Aycard, J. P. Chem. Phys. Lett. **2001**, *348*, 425.

(18) Schaff, J. E.; Roberts, J. T. *Surf. Sci.* **1999**, *426*, 384.

(19) Schaff, J. E.; Roberts, J. T. *J. Phys. Chem.* **1996**, *100*, 14151.

(20) Couturier-Tamburelli, I.; Chiavassa, T.; Pourcin, J. *J. Phys. Chem. B* **1999**, *103*, 3677.
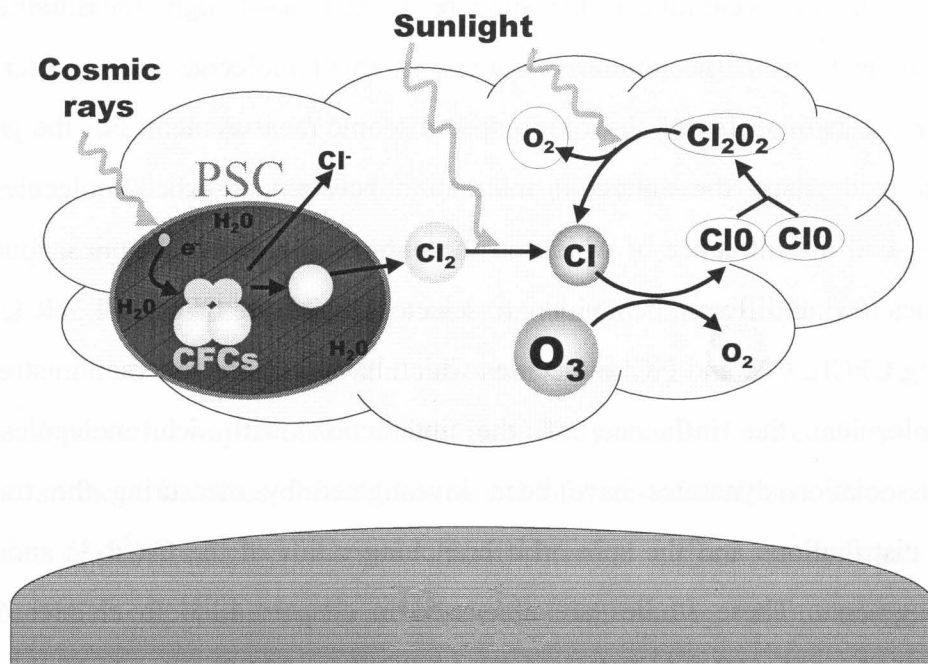
Figure 1.1 Cosmic-ray radiation produces an electron in icy grains in dense polar stratospheric clouds, which becomes a precursor to the solvated electron. The electron in the precursor state breaks a CFC to produce a Cl⁻ ion, which exists either as free ion, or as Cl_2 formed in a reaction with other species on PSCs. Then, sunlight produces Cl atoms by photodetachment of Cl- or photodissociation of Cl_2 to destroy O_3 via (Cl, ClO) reaction cycle.[44]

(21) Chaabouni, H.; Schriver-Mazzuoli, L.; Schriver, A. *J. Phys. Chem. A* **2000**, *104*, 6962.

(22) Haberkern, H.; Haq, S.; Swiderek, P. *Surf. Sci.* **2001**, *490*, 160.

(23) Borget, F.; Chiavassa, T.; Allouche, A.; Marinelli, F.; Aycard, J. *J. Phys. Chem. A* **2000**, *104*, 6962.

(24) Safarik, D. J.; Meyer, R. J.; Mullins, C. B. *J. Vac. Sci. Technol. A* **2001**, *19*, 1537.

(25) Ogasawara, H.; Horimoto, N.; Kawai, M. *J. Chem. Phys.* **2000**, *112*, 8229.

(26) Ogasawara, H.; Kawai, M. *Surf. Sci.* **2002**, *502-503*, 285.

(27) Monca, C.; Allouche, A. *J. Chem. Phys.* **2001**, *114*, 4226.

(28) Picaud, S.; Toubin, C.; Girardet, C. *Surf. Sci.* **2000**, *103*, 178.

(29) Bussolin, G.; Casassa, S.; Pisani, C.; Ugliengo, P. *J. Chem. Phys.* **1998**, *108*, 9516.

(30) Solomon, S. *Rev. Geophys.* **1988**, *26*, 131.

(31) Greenberg, J. M. *Chemistry in space*, NATO ASI series **1991**, *C323*, 227.

(32) Pirronello, V. *Chemistry in Space*, NATO ASI series **1991**, *C323*, 227.

(33) Festou, M. C.; Rickman, H.; West, R. M.; *Astron. Astrophys. Rev.* **1993**, *5*, 37.

(34) Dash, J. G. *J. Low Temp. Phys.* **1992**, *89*, 277.

(35) Honrath, R. E.; Peterson, M. C.; Guo, S.; Dibb, J. E.; Shepson, P. B., Campbell, B. *Geophys. Res. Lett.*, **1999**, *26*, 695.

(36) Kimmel, G. A.; Stevenson, K.P.; Dohnálek, Z.; Smith, R. S.; Kay, B. D. *J. Chem. Phys.* **2001**, *114*, 5284.

(37) Kimmel, G. A.; Dohnálek, Z.; Stevenson, K.P.; Smith, R. S.; Kay, B. D. *J. Chem. Phys.* **2001**, *114*, 5295.

(38) Stevenson, K. P.; Kimmel, G. A.; Dohnálek, Z.; Smith, R. S.; Kay, B. D. *Science* **1999**, *283*, 1505.

(39) Ikemiya, N.; Gewirth, A. A. *J. Am. Chem. Soc.* **1997**, *119*, 9919.

(40) Zondlo, M. A.; Onasch, T. B.; Warshawsky, M. S.; Tolbert, M. A.; Mallick, G.; Arentz, P.; Robinson, M. S. *J. Phys. Chem. B* **1997**, *101*, 10887.

(41) Sadtchenko, V.; Knutsen, K.; Giese, C. F.; Gentry, W. R. *J. Phys. Chem. B* **2000**, *104*, 2511.

(42) Sadtchenko, V.; Knutsen, K.; Giese, C. F.; Gentry, W. R. *J. Phys. Chem. B* **2000**, *104*, 4894.

(43) Sadtchenko, V.; Giese, C. F.; Gentry, W. R. *J. Phys. Chem. B* **2000**, *104*, 9421.

(44) Lu, Q.-B.; Sanche, L. *Phys. Rev. Lett.* **2001**, *87*, 078501

Chapter 2

Experimental

Two sets of experiments were performed. The time-of-flight (TOF) of the photofragments from the photodissociation of small molecules on a water ice film was conducted at Kyoto University and the infrared absorption spectroscopic (IRAS) measurements were carried out at Hokkaido University.

2.1 Measurements of Time-of-Flight (TOF) of the Photofragments by Resonance Enhanced Multiphoton Ionization (REMPI) Spectroscopy Technique at Kyoto.

2.1.1 State resolved molecules detection by REMPI spectroscopy. In this study, to detect photofragments in specific internal quantum states, resonance enhanced multiphoton ionization (REMPI) spectroscopic technique is used. A tunable probe laser is used to resonantly excite photofragments to an electronic excited state. The excited molecules are photoionized by one or more additional photons, and the resulting ions are detected with an electron multiplier. This method is sensitive only to molecules in specific quantum states, since the probe laser is absorbed only if it is tuned to a particular transition between quantum states (electric, vibrational, and rotational quantum numbers). The ion signal can be directly related to the number of molecules in the probed quantum state that are in the detection volume. By scanning the probe laser wavelength over one or several vibronic bands, the relative populations in the various internal states (rotational, spin-orbit, vibrational) can be determined from the measured line intensities, making use of known spectral line strengths and transition probabilities. Absolute populations can be obtained by calibrating the signal against reference spectra of the sample gas in thermal equilibrium at a known pressure and temperature.

2.1.2 Experimental techniques for TOF measurements of the photofragments. The experimental apparatus for state resolved surface photodissociation experiments consists of an ultrahigh vacuum system, a pulsed molecular beam, a photodissociation light source (excimer laser), a detection light source (dye laser) and a detection system

for desorbed products, as shown in Figure 2.1. The ice films were prepared on an Au substrate, details of which are presented in chapter 3. The Au substrates were prepared by dc glow-discharge sputtering, in which Ar^+ bombardment with low energy leads to atomic surface flatness of the sputtered films.[1] The substrate flatness was examined by scanning tunneling microscopy. The tilt angle was found to be at most 5°. This small tilt angle might cause an error within 1 % for calculation of the p- and s-polarization effect of the incident dissociation laser light on the photofragement yields. Typical grain sizes of the polycrystalline Au films were estimated to be submicrometers by our STM measurement. After the Au substrate was attached to a holder on an X-Y-Z stage in the vacuum chamber, it was cleaned by oxygen atoms produced from the 193 nm or 351 nm photodissociation of gaseous NO_2 at $T = 520$ K for 60 min. In this cleaning procedure, the excimer laser pulse was synchronized with expansion of NO_2 to Au. After this procedure, the Au substrate was annealed at 570 K for 5 min.

The small molecules were expanded with a pulsed molecular beam head (General Valve, 10 Hz). The pulsed gas expansion was synchronized with the dissociation laser trigger. The time delay between the molecular beam and photolysis laser triggers was typically set to 50 ms. The inset of Figure 2.1 shows the timing chart for the molecular beam, dissociation laser and probe laser pulses. The dissociation laser and probe laser pulses are pulsed lasers, repetition rate of which are10 Hz. The TOF method is ideally suited to measure velocity distributions of molecules in specific internal states by monitoring the signal as a function of time delay between dissociation and probe lasers. The distance between the substrate and the detection region was varied from 3 to 5 mm to change the effective flight lengths for neutral photofragments. A typical distance was set to 3 mm. Because the signal intensity did not depend on the time delay for 10-90 ms, the photofragments only from surface photodissociation were probed and unwanted gas phase photodissociation was totally avoided. To change the effective exposure of small molecules on ice films, the open gate time of the pulsed beam head was adjusted by changing the duration (300-500 μs) of the pulsed voltage to the beam head. The vacuum chamber was pumped by two turbo molecular pumps in tandem (600 and 50 L s^{-1}). The

chamber pressure was 0.5×10^{-8} and $(1\text{-}10) \times 10^{-8}$ Torr without and with sample molecules injection, respectively. The chamber pressure was monitored 50 cm away from the substrate with a cold cathode pressure gauge. The substrate temperature was controlled in the range $T = 85\text{-}700$ K by a combination of conductive cooling with liquid N_2 and resistive heating with an electric heater of a tantalum wire (0.35 mm diameter). The temperature can be maintained within 1 K.

Small molecules adsorbed on an ice film were photodissociated using an excimer laser (Lambda Physik, COMPex, 10 Hz). Photofragment TOF spectra were taken as a function of time delay, t, between photolysis and probe pulses. The time delay was controlled with a delay generator (Stanford Research). Neutral photofragments produced by the photolysis laser pulse were ionized through a resonance-enhanced multiphoton ionization (REMPI) process with an Nd^{3+}:YAG laser pumped dye laser (Lambda Physik, SCANmate). The subsequent ion signals were detected with a homemade TOF mass spectrometer (flight length = 25 cm) and normalized to the UV probe laser intensity.

2.2 Experimental Apparatus for Infrared Reflection Absorption Spectroscopy (IRAS) and Temperature-Programmed Desorption (TPD) Measurements at Hokkaido.

In this study, this spectroscopic technique is used to probe the structure of the ice and the ice surface. Infrared radiation (IR) is directed onto the sample and reflected from an underlying metal surface. The signal can be absorbed by both the bulk ice molecules, surface ice molecules and the adsorbate molecules on the ice surface. The gold surface is chemically inert, so it does not have a direct effect on the behaviour of the ice, but it will produce characteristic features in the IR spectrum. However a direct absorbtion spectrum is obtained by ratioing the ice spectrum with a 'background' spectrum of the gold film alone. This also eliminates spurious atmospheric signals from the spectrum.

All the measurements were carried out in an ultrahigh vacuum chamber system, which is shown in Figure 2.2. The chamber was equipped with a quadrupole mass spectrometer (ANELVA AQA-200) for desorbed gas analysis, an Ar-ion sputtering gun

for cleaning of metal surface, a vertically mounted xyz θ manipulator for controlling the sample direction, and BaF_2 windows (54 mm in diameter) specially made for UHV IRAS[24,25], cut off wavelength of which is around 900 cm^{-1}. The chamber was pumped by a turbomolecular pump (Leybold, 400 L/s) and an ion pump (ANELVA, 270 L/s), and the base pressure was 1×10^{-10} Torr. The Au(111) substrate was held on the sample holder with using Ta wires (0.3mm in diameter). The substrate could be heated by the Ta wire heaters to temperatures higher than 1000 K and cooled to 90 K with a liquid-nitrogen-cooled copper plate. Substrate temperature was measured with a chromel-alumel thermocouple attached to the side of the substrate. Gases were introduced into the chamber through a long nozzle set on a liner-translator, the end of that was ca. 1 cm away from the substrate during dosing processes. A pulsed valve (General Valve) was used to control the dosing amount of a gas.

For IR reflection absorption spectroscopy (IRAS) measurements, IR beam from FTIR (Fourier transform infrared spectrometer, BIO-RAD FTS-155) was introduced into a chamber through a BaF_2 window after p-polarized by a wire grid polarizer since only p-polarized light is effective for IRAS. The reflected IR beam from substrate came to a MCT (Hg-Cd-Te) detector cooled at a liquid N_2 temperature, and then recorded by a computer with passing through some amps and A/D converters electrically. The incidence angle of the IR beam was ca. 85°. The paths of the IR beam were purged with dry air to prevent the effect of an absorption by water vapor at the out side of the chamber, since such an absorption jams measuring an IR spectrum. All the spectra were recorded with a resolution of 4 cm^{-1} and the average of 200 scans.

Temperature-programmed desorption (TPD) spectra were measured with a quadrupole mass spectrometer, which measured the relative amount of molecules desorbed from the substrate, and a programmable temperature regulator (Chino KP-31E) to raise the substrate temperature at a ramp 4 k/s regularly. Both of them were controlled by a computer (NEC PC-9801RX).
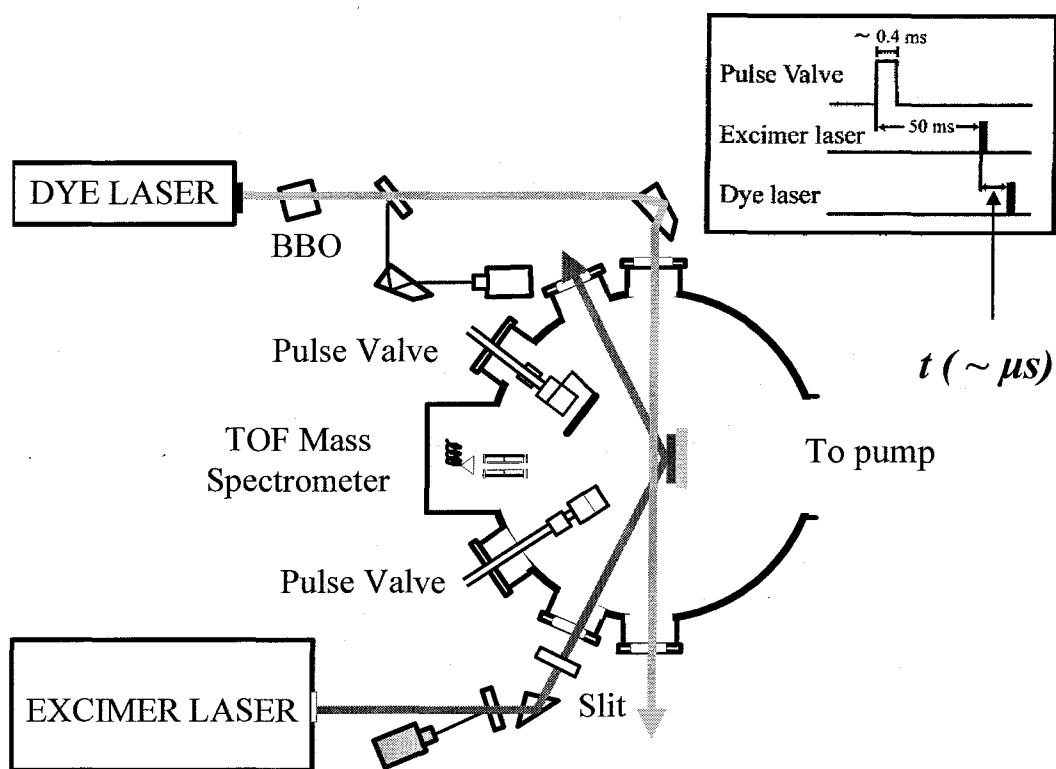
Figure 2.1 Schematic diagram of experimental setup. Using pulsed molecular beam, small molecules adsorbs on water an ice film prepared on a polycrystalline Au. The photofragments from the photodissociation of small molecules on the ice film are detected by the resonance-enhanced multiphoton ionization technique. The timing plot for measurement of a TOF spectrum is shown in the inset where the delay time t between dissociation and probe laser pulses corresponds to the TOF.
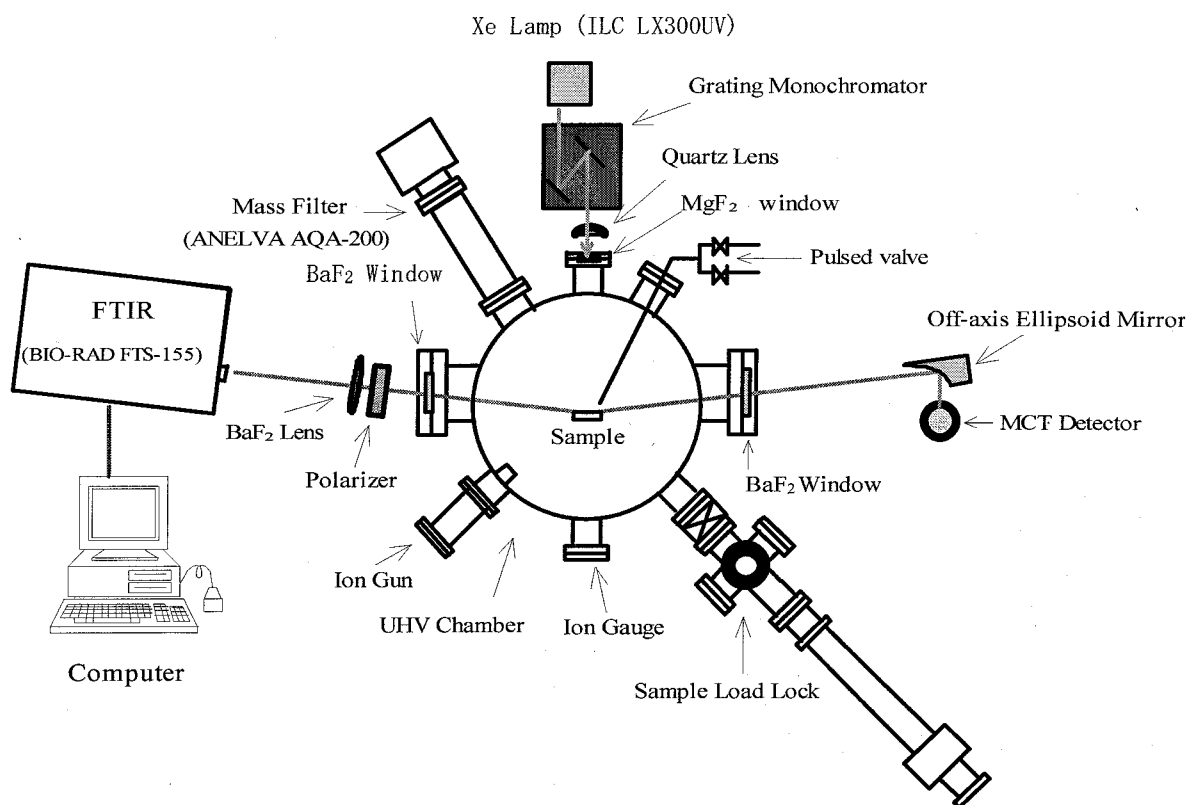
Figure 2.2 Schematic diagram of infrared reflection absorption spectroscopy apparatus.

Reference

(1) Kawasaki, M. *Appl. Surf. Sci.* **1998**, *135*, 1159.

Chapter 3

Water Ice Films

3.1 Structures of Water Ice Films on Metal Substrates. In order to characterize the ice structure, the conditions for which the ice film was obtained have to be defined with special care. The characteristics of structure depend on the external physical conditions (pressure, temperature, radiation, substrate), the nature of the interface (vacuum/ice, air/ice, gas/liquid/ice, etc.) and on the probe scale.[1] Molecular adsorption of water on surfaces in ultrahigh vacuum is usually accompanied by one or more preferential orientations of the molecule on the surface. This is usually with the oxygen-end down and one or both O-H bonds oriented away from the surface.[2] Both the substrate and water-water interactions play major roles in indicating the orientation of adsorbed water.

On hexagonal metal surfaces, water molecules favor the formation of a hexagonal two-dimensional lattice known as bilayer ice. This is a truncation of the naturally occurring hexagonal ice (I_h). Bernal et al.[3] formulated rules (BFP-rules) which define the structure of the three-dimensional I_h ice lattice. These rules have been extended to the hydrogen bonding of the water bilayer. The resulting proposed structure consists of water molecules within a bilayer which are hydrogen-bonded into hexagonal rings such that alternating molecules are raised or lowered by 0.048 nm relative to the central plane to give the proper tetrahedral bonding angles. Successive bilayers are joined by the raised molecules of one bilayer hydrogen-bonded to the lowered molecules of the next layer. The tetrahedral bonding configuration is maintained for water bound to the surface even for incomplete layers.[4] Half of the water molecules in this first bilayer forms direct bonds to the surface via an oxygen lone pair orbital and the other half is only held via hydrogen bonds to the first layer molecules.

The misfit between the I_h ice lattice and the fcc(111) surface is correlated with the bond strength between adsorbed layer and surface and therefore the desorption temperature in thermal desorption spectroscopy (TDS). The ice bilayers on fcc(111)

with the lowest desorption temperature in TDS are Ag(111), Cu(111), and Ag(111),[2,5-7] because water tends to form three-dimensional nanoclusters on these three surfaces due to the weak water-surface interaction. A 7% mismatch exists between the Ag(111) surface lattice (a = 0.289 nm, next nearest neighbor (NNN) distance 0.501 nm) and the triangular unit of crystalline ice in the I_h form (oxygen-oxygen: 0.274 nm at 90 K,[2] NNN: 0.475 nm), i.e., the surface unit cell is too large to accommodate a hydrogen-bonded bilayer while maintaining on-top adsorption sites for the H_2O molecules. Consequently, it has been predicted that a commensurate water overlayer will not form.[2] Indeed, at 80 K no evidence for long-range or short-range local bonding order was detected at low coverage.[8]

The experimental methods that show most promise for obtaining adsorbate structural data are those involving electron diffraction (LEED or photoelectron diffraction) or X-ray absorption fine structure. These techniques are useful for structural information pertaining to the location of water on a surface. As an example of water structure obtained by electron diffraction, Held and Menzel have performed detailed LEED-IV on the $(\sqrt{3} \times \sqrt{3})$ $R30°$ D_2O bilayer on Ru(0001), as is shown in Figure 3.1. One of the salient characteristics of bilayer water on close-packed metal surface is its ability to form long-range-ordered structures consisting of ice-like rings of water hexamers in registry with the hexagonal surface lattice. Accordin to Theil and Madey,[9] the prevailing long-range structure of water on close-packed metal surface is the $(\sqrt{3} \times \sqrt{3})$ $R30°$ structure. The variety of surfaces on which this structure has been observed, which is shown in Table 3.1, with measurements coming from both LEED and other diffraction techniques, as well as from scanning probe studies.

Clustered water is characterized by the presence of hydrogen bonds between two or more neighboring water molecules. Because of its remarkable ability to form hydrogen-bonding networks, water displays a variety of structures associated with clustering that span from dimmer to the diverse properties of liquid and solid water.

There are two primary factors that favor water clustering on solid surfaces, as pointed out by Griffiths et al.[10]: (1) weak water-surface interactions and (2) rapid surface

18

diffusion of water. Weak water-surface interactions, in comparison with water-water interactions, provide a thermodynamic basis for clustering. Strong water-surface interactions place water in an adsorption configuration in which water-water hydrogen-bonding interactions are structurally and/or thermodynamically unfavorable. Surface diffusion is necessary in that forming clusters requires adsorbed water molecules to find each other. Irrespective of the water-surface interaction, if diffusion is slow, clusters are unlikely to form until the coverage is sufficiently high. This is why the observations of monomerically adsorbed water were typically made at extremely low substrate temperatures where diffusion lengths are minimized. However, if diffusion is rapid and the water- surface interaction is structurally conductive, clustering is likely.

For the Au substrate, low energy electron diffraction (LEED) measurements showed that on Au(111) the first bilayer grows at 120 K in ($\sqrt{3} \times \sqrt{3}$) $R30°$ structure stretched to the substrate lattice constant.[11] Upon increasing H_2O coverage the LEED pattern structure fades away into a diffuse background intensity until an incommensurate pattern structure develops for the condensed layer regime. This pattern structure is also azimuthally oriented, namely rotated 30° with respect to the Au(111) substrate and comparable to the commensurate ($\sqrt{3} \times \sqrt{3}$) $R30°$ structure. On the other hand, scanning tunneling microscope (STM) revealed an amorphous wetting layer at 100 K with three-dimensional second layer nucleation.[12]

3.2 Preparation of Water Ice Films and Their Characteristics in This Study.
Infrared spectroscopic studies have been reported to investigate the structure and surface differences of the various water ice films. Jenniskens and Blake found that water ice formed by vapor deposition exists in three metastable amorphous forms and two crystalline forms.[13] When grown in a vacuum by vapor deposition on a cold substrate, amorphous ice dominates at temperature below 130 K.[14-16] From 130 K to 155 K a mixture of amorphous and cubic ice may exist.[17] The porosity of amorphous ice films depends on the temperature and rate of water deposition. Unless the water partial pressure is less than 10^{-9} Torr, pore-free ice film cannot be achieved.[15] Under our water

deposition conditions, that is, high water flux and low deposition temperature, the resulting amorphous ice films should be highly porous. Consulting the studies for preparation of ice, we prepared amorphous and crystalline ice films.[18-22]

At Hokkaido, ice films were prepared on an Au(111) single crystal. After water vapor was deposited at temperatures below 100 K, the substrate temperature was increased. A significant change in IRAS spectrum appeared. The bulk OH stretching band at 3370 cm^{-1} shifted to the crystalline OH stretching band at 3250 cm^{-1} with the substrate temperature, while the free or dangling OH stretching band of the surface water at 3700 cm^{-1} and the HOH bending band at 1654 cm^{-1} decreased in intensity. The spectrum at 140 K is basically identical to that of crystalline ice.[23,24] Since these spectral changes start at 120 K, the phase change of amorphous to crystalline ice occurs above 120 K. It was found that amorphous ice transforms into cubic ice on gold at 130 K by Chaabouni et al.,[22] and at 136.8±1.6 K by Bar-Nun et al.[25] We prepared an amorphous ice film by depositing water vapor on Au below 100 K. A crystalline ice film was prepared by annealing the amorphous ice film at 130 K for > 25 min and then was cooled down to an appropriate temperature T. Wang and Koel also measured IRA spectra of water films on Au(111).[26] The free OH peak decreased as the annealing temperature was increased, disappearing between 110 and 135 K. However, according to Jenniskens et al., the crystallization was not complete and the amorphous component was still intimately mixed with the cubic state in the crystallites.[27] The interfaces of crystallites were disordered and grain boundaries were formed. Sadtchenko et al. observed the grain boundaries in the crystalline ice films by observing the uptake behavior of HCl.[28] According to them, (a) the ratio of the net surface area of the grain boundaries to the net open area of the crystalline ice film is quite low, and (b) the average size of the grain boundaries is small and their density is high.

At Kyoto, water ice films were prepared on the polycrystalline Au substrates with (111) domains. The Au substrates were prepared by dc glow-discharge sputtering, in which Ar^+ bombardment with low energy leads to atomic surface flatness of the sputtered films.[29] The substrate flatness was examined by scanning tunneling

microscopy. The tilt angle was found to be at most 5°. This small tilt angle might cause an error within 1 % for calculation of the p- and s-polarization effect of the incident dissociation laser light on the Cl yields. Typical grain sizes of the polycrystalline Au films were estimated to be submicrometers by our STM measurement. After the Au substrate was attached to a holder on an X-Y-Z stage in the vacuum chamber, it was cleaned by oxygen atoms produced from the 193 nm or 351 nm photodissociation of gaseous NO_2 at $T = 520$ K for 60 min. In this cleaning procedure, the excimer laser pulse was synchronized with expansion of NO_2 to Au. After this procedure, the Au substrate was annealed at 570 K for 5 min.

An amorphous ice film was prepared by deposition of water on the polycrystalline Au substrate at 85 K with a pulsed molecular beam at the angle of incidence of 45°. Stagnation pressure was 20 Torr of water vapor. According to Stevenson et al., Kimmel et al., and Ikemiya and Gewirth, they call the amorphous ice film as "amorphous solid water (ASW)".[12, 30-32] The structure of the microporous ASW depends on variables such as substrate temperature, the angle of incidence and flux of the water molecular beam, as is shown in Figure 3.2. Stevenson et al. reported N_2 adsorption on ASW grown at 22 K as a function of film thickness for various deposition angles.[32] The deposition at 45° polar angle showed one-third of that at 60° deposition. A linear dependence of the N_2 deposition with the film thickness was observed when the ASW film was prepared only with off-normal deposition angle. N_2 is trapped in the pore structure of ASW. The adsorption of N_2 by the ASW films grown with molecular beams is less than that by P-ASW grown with background dosing. P-ASW stands for "highly porous amorphous solid water". The porosity/morphology of the P-ASW prepared by the background dosing was higher than the ASW prepared by the molecular beam method, as is shown in Figure 3.2.[30-32] This difference is due to the difference in the pore structures. In the present experiment, we tested the P-ASW with the background deposition of water vapor at 90 K for 60 min on the polycrystalline Au substrate, which is characterized by a high surface area and low density. Ikemiya and Gewirth observed the cross-sectional view of P-ASW on Au(111).[12] The H_2O islands do not have atomically flat surfaces. The

height of the planar monolayer water film is about 0.15 nm directly above the Au surface, while the cluster reaches to 0.45 nm. The H_2O clusters appear only atop the amorphous film and not the bare Au(111) surface. Unless otherwise noted, we used the ASW for experiment, which was prepared with the molecular beam method. Sato et al. estimated that the exposure of H_2O necessary to obtain 1 monolayer (ML) of ice film on the Au(111) substrate was 3 langmuir at 90 K.[33] In our experiment, the exposure was 1800 langmuir, which resulted in formation of 600 ML of H_2O on Au for background deposition, and more than 90 ML for direct adsorption by the molecular beam method.

A crystalline ice film was prepared by annealing the ASW at 130 K for > 5 min. Annealing ASW, which is a metastable state of ice, crystallizes it to form a polycrystalline ice (PCI) film. In addition, another preparation method was tested. After background deposition of water vapor at 130 K for 60 min, the ice film was annealed at 130 K for > 30 min. Four types of water ice films prepared in this study are summarized in Table 3.2.

TABLE 3.1 : Ordered 2D overlayers of water on solid surface (all observations were with LEED unless otherwise noted)[34]

Substrate	Orderd pattern	Temperature
Au(111)	$(\sqrt{3} \times \sqrt{3})\,R30°$	$120^{\,a}$
Pt(111)	$(\sqrt{3} \times \sqrt{3})\,R30°$	$100^{\,b}$
	$(\sqrt{37} \times \sqrt{37})\ R25.3°$ and $(\sqrt{39} \times \sqrt{39})\ R16.1°$	130^{d}
	domains^{c} Hexagonal	$160^{e,f}$
Ru(0001)	$(\sqrt{3} \times \sqrt{3})\,R30°$	95^{g}
	$(\sqrt{3} \times \sqrt{3})\,R30°{}^{h}$	$80\text{-}175^{i}$

^{a} From ref. 11. ^{b} From ref. 35. ^{c} Detected with He atom scattering. ^{d} From ref. 36 ^{e} From ref. 37. ^{f} From ref. 38. ^{g} From ref. 39. ^{h} Slit spots detected. ^{i} From ref. 40.

TABLE 3.2 : Preparation of water ice films

state of ice film	preparation of water ice film
polycrystalline	After direct adsorption of water at 85 K with pulsed molecular beam, the ice film was annealed at 130 K for > 5 min. The state of the ice film is PCI (polycrystalline ice).
polycrystalline	After background adsorption of water vapor at 130 K, the ice film was annealed at 130 K for > 30 min. The state of the ice film is PCI (polycrystalline ice).
amorphous	Prepared by the molecular beam method of water vapor at 85 K. The state of the ice film is ASW (amorphous solid water).
amorphous	Prepared by background background adsorption at 90 K. The state of the ice film is P-ASW (highly porous amorphous solid water).
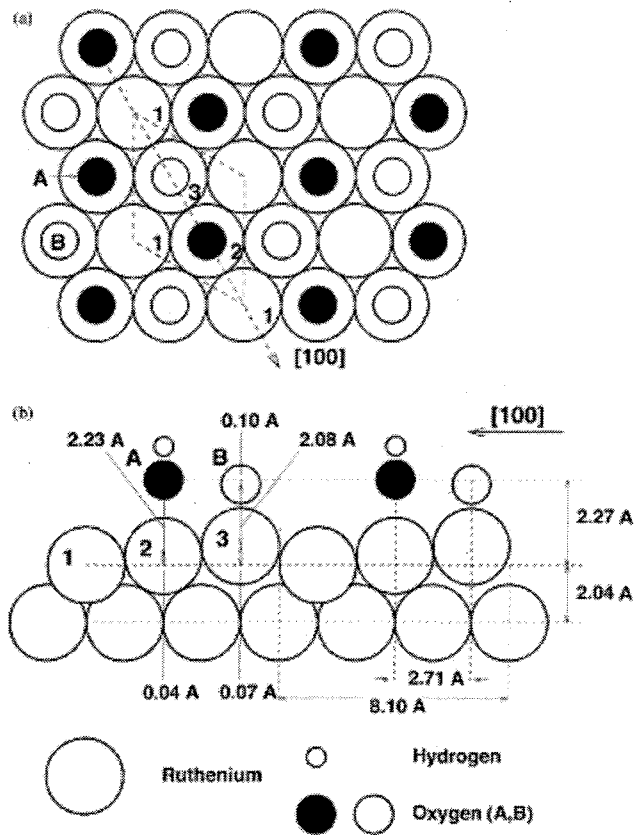
Figure 3.1 Schematic representation of the best-fit of geometry of the $(\sqrt{3} \times \sqrt{3})$ $R30°$ D_2O bilayer on $Ru(0001)$ obtained from LEED-IV analysis at 100 K. (a) Top view of the surface and (b) a cut through the surface along the [110]-direction (as shown in 'a'). Atom types are indicated in the bottom. Ru atoms labeled 1,2 and 3 correspond to those in the center of water hexagonal (no water bonded), those binding to second-layer water and those binding to first-layer water, respectively. From ref. 41.
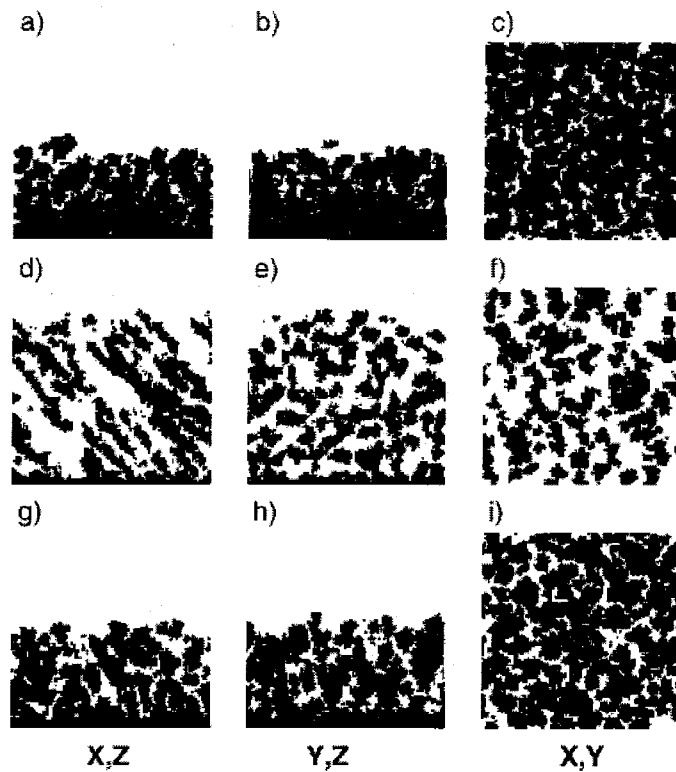
Figure 3.2 Three-dimensional ballistic deposition simulations of 50 ML films. The x and y dimensions are 130 lattice units. The particles were annealed four steps after initially striking the surface. The figure shows slices of the simulated films which are one unit thick from three different perspectives: (a), (d), and (g) show films in the plane y=65. (b), (e), and (h) show films in the plane x=65. (c), (f), and (i) show films in the plane z=z_max/2, where z_max is the highest point in the film. In these views, portions of the film which appear disconnected from the rest of the film are in fact connected out of the plane of the figure. For (a)–(c) θ=0°. These films are relatively dense density=0.87) with small pores. For (d)–(f) θ=70° and the incident particles were parallel to the x-z plane. The density of this film is 0.50. (d)Similar to the 2D simulations, large, angular pores develop for larger angles of incidence. (f) Viewed at a constant z, the film is seen to have an irregular array of columns. The columns are of variable shape and orientation. Both (e) and (f) demonstrate that the film growth is highly correlated in the direction transverse to the plane of incidence. For (g)–(i) the incident particles had a random cosine distribution of incident polar angles (with random azimuthal angle) to simulate background dosing. The density of this film is 0.76. From ref. 31.

References

(1) Wettlaufer, H. R.; Dash, J. G.; Untersteiner, N. *Ice Physics and the Natural Environment*, NATO ASI Series, Vol. 56, Springer, Berlin, 1999.

(2) Theil, P. A.; Madey, T. E. *Surf.* Sci. Rep. **1987**, *7*, 211.

(3) Bernal, J. D.; Fowler, R. H. *J. Chem. Phys.* **1993**, *1*, 515.

(4) Doering, D. L.; Madey, T. E. *Surf. Sci.* **1982**, *123* 305.

(5) Kay, B. D.; Lykke, K. R.; Creighton, J. R.; Ward, S. J. *J. Chem. Phys.* **1989**, *91*, 5120.

(6) Hinch, B. J.; Dubois, L. H. *J. Chem. Phys.* **1992**, *96*, 3262.

(7) Smith, R. S.; Huang, C.; Wang, E. K. C.; Kay, B. D. *Surf. Sci. lett.* **1996**, *367*, L13.

(8) Klaua, M.; Madey, T. E. *Surf. Sci.* **1984**, *136*, L42.

(9) Theil, P. A.; Madey, T. E. *Surf. Sci. Rep.* **1987**, *7*, 211.

(10) Griffiths, K.; Kasza, R. Esposto, F. J.; Callen, B. W.; Bushby, S. J.; Norton, P. R. *Surf. Sci.* **1994**, *307-309*, 60.

(11) Pirug, G.; Bonzel, H. P. *Surf. Sci.* **1998**, *405*, 87.

(12) Ikeyama, N.; Gewirth, A. A. *J. Am. Chem. Soc.* **1997**, *119*, 9919.

(13) Jenniskens, P.; Blake, D. F. *Science*, **1994**, *265*, 753.

(14) Sadtchenko, V.; Knutsen, K.; Giese, C. F.; Gentry, W. R. *J. Phys. Chem. B* **2000**, *104*, 2511.

(15) Zondlo, M. A.; Onasch, T. B.; Warshawsky, M. S.; Tolbert, M. A.; Mallick, G.; Arentz, P.; Robinson, M. S. *J. Phys. Chem. B* **1997**, *101*, 10887.

(16) Berland, B. S.; Brown, D. E.; Tolbert, M. A.; George, S. M. *Geophys. Res. Lett.* **1995**, *22*, 3493.

(17) Eizenberg, D.; Kauzmann, W. *The structure and Properties of water*; Oxford University Press: New York, 1969.

(18) Hessinger, J.; White B. E.; Pohl, R. O. *Planet Space Sci.* **1996**, *44*, 937.

(19) Schaff, J. E.; Roberts, J. T. *Surf. Sci.* **1999**, *426*, 384.

(20) Couturier-Tamburelli, I.; Chiavassa, T.; Pourcin, J. *J. Phys. Chem. B* **1999**, *103*,

3677.

(21) Dohnálek, Z.; Ciolli, R. L.; Kimmel, G. A.; Stevenson, K. P.; Smith, R. S.; Kay, B. D. *J. Chem. Phys.* **1999**, *110*, 5489.

(22) Chaabouni, H.; Schriver-Mazzuoli, L.; Schriver, A. *J. Phys. Chem. A* **2000**, *104*, 6962.

(23) Tolbert, M. A.; Middlebrook, A. M. *J. Geophys. Res.* **1990**, *95*, 22423.

(24) Schaff, J. E.; Roberts, J. T. *J. Phys. Chem.* **1996**, *100*, 14151.

(25) Bar-Nun, A.; Dror, J.; Kochavi, E.; Laufer, D. *Phys. Rev. B* **1987**, *35*, 2427.

(26) Wang, J.; Koel, B. E. *Surf. Sci.* **1999**, *436*, 15.

(27) Jenniskens, P.; Banham, S. F.; Blake, D. F.; McCoustra, M. R. S. *J. Chem. Phys.* **1997**, *107*, 1232

(28) Sadtchenko, V.; Giese, C. F.; Gentry, W. R. *J. Phys. Chem. B* **2000**, *104*, 9421.

(29) Kawasaki, M. *Appl. Surf. Sci.* **1998**, *135*, 1159.

(30) Kimmel, G. A.; Stevenson, K.P.; Dohnálek, Z.; Smith, R. S.; Kay, B. D. *J. Chem. Phys.* **2001**, *114*, 5284.

(31) Kimmel, G. A.; Dohnálek, Z.; Stevenson, K.P.; Smith, R. S.; Kay, B. D. *J. Chem. Phys.* **2001**, *114*, 5295.

(32) Stevenson, K. P.; Kimmel, G. A.; Dohnálek, Z.; Smith, R. S.; Kay, B. D. *Science* **1999**, *283*, 1505.

(33) Sato, S.; Yamaguchi, D.; Nakagawa, K.; Inoue, Y.; Yabushita, A.; Kawasaki, M. *Langmuir* **2000**, *16*, 9533.

(34) Henderson, M. A. *Surf. Sci. Rep.* **2002**, *46*, 1.

(35) Fisher, G. B; Gland, G. L. *Surf. Sci.* **1980**, *94*, 446.

(36) Glebov, A.; Graham, A. P.; Menzel, A.; Toennis, J. P. *J. Chem. Phys.* **1997**, *106*, 9382.

(37) Starke, U.; Materer, N.; Barbieri, A.; Doell, R.; Heinz, K.; Van Hove, M. A.; Somorjai, G. A. *Surf. Sci.* **1993**, *287-288*, 432.

(38) Starke, U.; Heinz, K. Materer, N.; Wander, A.; Michl, M.; Doll, R.; Van Hove, M. A.; Somorjai, G. A. *J. Vac. Sci. Technol.* **1992**, *A 10*, 2521.

(39) Thiel, P. A.; Hoffman, F. M.; Weinberg, W. H. *J. Chem. Phys.* **1981**, *75*, 5556.

(40) Doering, D. L; Madey, T. E. *Surf. Sci.* **1980**, *94*, 446.

(41) Held, G.; Menzel, D.; *Suf. Sci.* **1994**, *316*, 92.

Chapter 4

Photodissociation of Chlorine Molecules Adsorbed on Amorphous and Crystalline Water Ice Films

Abstract

The photodissociation dynamics of chlorine molecules adsorbed on amorphous and crystalline water ice films was investigated at 351 nm. The ice films were prepared on a gold polycrystalline substrate at 80–140 K. TOF spectra of the photofragment chlorine atoms, measured with the REMPI technique, were simulated with a composite of two translational energy distributions: a Gaussian distribution and a flux-weighted Maxwell-Boltzmann distribution. For both amorphous and crystalline ice films, the Gaussian distribution is characterized by the average energy $<E_t> = 0.38 \pm 0.02$ eV, while the Maxwell-Boltzmann one by $<E_t> = 0.12 \pm 0.01$ eV. The Gaussian distribution is attributable to the chlorine atoms produced from the direct photodissociation of Cl_2, while the Maxwell-Boltzmann characterizes those having undergone strong relaxation processes. The observed translational energy distributions for amorphous and crystalline ice films were similar to each other, but the relative contribution of the two energy distributions as well as the photodissociation yield of Cl atoms depend on the states of the ice films. Free OH groups and surface morphology of an ice film surface have a strong influence on the photodissociation quantum yield. The adsorbate-water interaction for Cl_2 and an ice surface is discussed on the basis of the measurements of TOF, IRA, and TPD spectra.

4.1 Introduction

The photochemistry of molecules adsorbed on water ice films has received considerable attention in recent years from atmospheric and astro-chemistry points of view, in which the interaction between an adsorbate and an ice surface has been investigated.[1-9] Adsorption, desorption, surface mobility, and bulk diffusion of reagents and reaction products may all depend on the ice microstructure. Morphology may have a significant effect on the reactivity of ice films.[10-12] Pores have been observed to facilitate trapping of large quantities of gases in the bulk of amorphous ice films. A high density of surface defects may also lead to an increase in the hydrogen bonding abilities of ice surface and pore. Chemical reactions on ice surface were studied for atmospherically important inorganic chlorides.[13-16] The dark reactions of the chlorides on ice surface release Cl_2 to the air due to the chemically active nature of the ice surface. The interaction between water and Cl_2 has been studied experimentally and theoretically.[17-25] The geometry of the $Cl_2\cdots OH_2$ complex was observed by the pulse-jet technique with Fourier transform microwave spectroscopy.[25] The Cl_2 molecule points toward the lone pair electrons on the oxygen atom. An ab initio study predicts the interaction energy for $Cl_2\cdots(OH_2)_4$ to be 0.12 ± 0.01 eV.[23] In addition, a weak hydrogen-bond-like interaction between Cl_2 and H_2O is expected, which was reported for the case of $Br_2\cdots HOH$ by Ramondo et al.[26] Since the electronegativity of Cl is larger than Br, this type of interaction would be more effective for $Cl_2\cdots HOH$ than for $Br_2\cdots HOH$. The low interaction energy is in good agreement with the laboratory measurement that Cl_2 desorbs rapidly from the water ice surface.[13] Banham et al. reported that the desorption temperature of Cl_2 from a water ice surface was ca. 110 K.[19] Graham and Roberts studied the interaction of Cl_2 with amorphous ice using TPD spectroscopy.[21] They found that an exposure of 0.09 langmuir at 100 K was sufficient to saturate the surface with Cl_2, because Cl_2 does not condense into multilayers at 100 K. Cl_2 desorbed mainly at 125 K. A secondary ion mass spectrometric measurement reported by Donsig et al. implied that Cl_2 reacts with ice above 130 K to form HOCl

and HCl.[20]

The ultraviolet absorption spectrum of Cl_2 in the gas phase is continuous between 250 and 450 nm. The absorption spectrum at 351 nm is dominated (99%) by the $1_u(^1\Pi_u)$ excited electronic state, which produces two ground-state chlorine atoms $Cl(^2P_{3/2})$. The $0_u(B\ ^3\Pi_u)$ state, which produces a spin-orbit excited-state chlorine atom $(Cl^*(^2P_{1/2}))$ and a ground-state chlorine atom (Cl), contributes less than 1%.[27-31] The photodissociation of Cl_2 in adsorbed and condensed states has been investigated by laser spectroscopic techniques.[32-35] Giorgi et al. reported the 351 nm photodissociation dynamics of Cl_2 adsorbed on LiF(001) at 25-70 K.[35] The translational energy distributions consist of the following three channels. The direct photodissociation channel of adsorbed $Cl_2(ad)$ resulted in the formation of Cl atoms with an average translational energy of 0.35-0.40 eV. An additional channel with the higher translational energy was attributed to the photodissociation of a metastable molecule, $Cl_2\cdots Cl(ad)$. The third channel was assigned to Cl atoms having collided with other Cl_2 molecules adsorbed on the surface. In this work, we have investigated the UV photodissociation dynamics of Cl_2 adsorbed on amorphous and crystalline water ice films by measuring the translational energy distributions of the $Cl(^2P_j)$ fragments with TOF photofragment spectroscopy. Free OH groups on the ice film surface have a strong influence on the photodissociation quantum yield. Since free OH groups exist on the polar stratospheric cloud ice surface, it is interesting to study the difference in chemical reactivities of amorphous and crystalline ice films.[36]

4.2 Experimental

Details of water ice films are described in chapter 3.

4.2.1 Measurement of TOF spectra of the photofragment $Cl(^2P_j)$ atom. Surface photodissociation of Cl_2 adsorbed on crystalline and amorphous water ice films was performed with a combination of a pulsed molecular beam, excimer laser, and dye laser. The ice films were prepared on an Au substrate, as discussed below. The Au substrate

prepared with a sputtering technique was mainly composed of domains with (111) structure. The present experimental setup is schematically shown in Figure 3.1. The gas mixture of Cl_2 with N_2 diluent (ca. 17%) was expanded with a pulsed molecular beam head (General Valve, 10 Hz). A typical stagnation pressure of the gas valve was 100 Torr. The pulsed gas expansion was synchronized with the dissociation laser trigger. The time delay between the molecular beam and photolysis laser triggers was typically set to 50 ms. The inset of Figure 3.1 shows the timing chart for the molecular beam, dissociation laser and probe laser pulses. Because the signal intensity did not depend on the time delay for 10-90 ms, the Cl photofragments only from surface photodissociation were probed and unwanted gas phase photodissociation was totally avoided. To change the effective exposure of Cl_2 on ice films, the open gate time of the pulsed beam head was adjusted by changing the duration (300-500 μs) of the pulsed voltage to the beam head. The vacuum chamber was pumped by two turbo molecular pumps in tandem (600 and 50 L s^{-1}). The chamber pressure was 0.5×10^{-8} and $(1-10) \times 10^{-8}$ Torr without and with sample gas injection, respectively. The chamber pressure was monitored 50 cm away from the substrate with a cold cathode pressure gauge. Under these pressure conditions, Cl_2 formed a submonolayer-to-multilayer on the ice films, depending on both the substrate temperature and the effective exposure of Cl_2 from the pulsed molecular beam head, as discussed below. The substrate temperature was controlled in the range $T =$ 85-700 K by a combination of conductive cooling with liquid N_2 and resistive heating with an electric heater of a tantalum wire (0.35 mm diameter). The temperature can be maintained within 1 K.

Cl_2 molecules adsorbed on an ice film were photodissociated using an excimer laser (Lambda Physik, COMPex, 10 Hz, typically less than 0.5 mJ cm^{-2} pulse^{-1}) at 351 nm. Photofragment TOF spectra were taken as a function of time delay, t, between photolysis and probe pulses. The time delay was controlled with a delay generator (Stanford Research). Neutral Cl photofragments produced by the photolysis laser pulse were ionized through a (2+1) REMPI process at 235.336 nm for $Cl(^2D_{3/2}-{}^2P_{3/2})$ and 235.205 nm for $Cl^*(^2P_{1/2}-{}^2P_{1/2})$ with an Nd^{3+}:YAG laser pumped dye laser (Lambda

Physik, SCANmate, 0.2 mJ pulse^{-1} at UV). For each spin-orbit state, the REMPI intensity , I, depends both on the quantum state population, N, and on the ionization efficiency, S. Thus, $I(\mathrm{Cl}^*)/I(\mathrm{Cl}) = [N(\mathrm{Cl}^*)/N(\mathrm{Cl})] \times [S(\mathrm{Cl}^*)/S(\mathrm{Cl})]$. The scaling factor $f = S(\mathrm{Cl}^*)/S(\mathrm{Cl})$ was reported to be 1.06 ± 0.17 by Regan et al.[37] The subsequent ion signals were detected with a homemade TOF mass spectrometer (flight length = 25 cm) and normalized to the UV probe laser intensity.

To simulate the TOF spectra, we used a composite of two different energy distributions; a Gaussian, $P_G(E_t)$, and a flux weighted Maxwell-Boltzmann, $P_{MB}(E_t)$. $P_{MB}(E_t)$ is characterized by the average kinetic energy, $<E_t> = 2k_B T_{trans}$, where k_B is the Boltzmann constant and T_{trans} is the translational temperature. Conversion from the energy distribution to the TOF distribution was performed using the Jacobian listed by Zimmerman and Ho.[38] In our simulation, it was assumed that (a) photofragments are detected at a point detection region of REMPI, (b) photofragments come into the gas phase from a round substrate area (12 mm diameter) with a $\cos^n \theta$ distribution, where θ is a departing polar angle from the substrate. The diameter of the effective photoirradiation area was determined by a round aperture in front of the reaction chamber window for the dissociation laser. The distance between the substrate and the detection region was varied from 3 to 5 mm to change the effective flight lengths for neutral photofragments. A typical distance was set to 3 mm. The simulation procedure mentioned above was tested by the 351 nm photodissociation of Cl_2 adsorbed on a cooled sapphire substrate. The main part of the observed TOF spectrum for the photoproduct Cl was reproduced by the translational energy distributions reported for Cl_2 on LiF by Giorgi et al.[35]

Unless otherwise noted, typical experimental conditions were $P = 4 \times 10^{-8}$ Torr, $T = 85$ K, and 0.5 mJ cm^{-2} pulse^{-1} at 351 nm, and Cl was probed. The pressure P is the observed chamber pressure minus the background pressure of 0.5×10^{-8} Torr and is assumed to represent an effective exposure of Cl_2 to the ice surface. This pressure and substrate temperature condition corresponded to about a monolayer of Cl_2 on the ice film, as discussed in the Results.

4.2.2 Measurement of IRA spectra and TPD spectra. Infrared and TPD measurements were carried out in an ultrahigh vacuum chamber, which was described in detail previously.[39] An Au(111) single-crystal substrate (12 mm in diameter, 1.5 mm thick, 99.999% purity) was cleaned by repeated Ar-ion sputtering at 800 K and was annealed at 900 K. Ozone was used for the surface cleaning purpose. Ice films were prepared on Au(111) as discussed below. Before and after Cl_2 gas was deposited on ice films by the pulsed molecular beam head, IRA spectroscopic measurements were performed. The IR beam from a FTIR spectrometer (BIO-RAD, FTS-155) was p-polarized by a wire grid polarizer and then was introduced into the vacuum chamber through a BaF_2 window with the incident angle of the IR beam of 85°. IRA spectra were recorded with 4 cm^{-1} resolution and 200 scans. The paths of the IR beam were purged with dry air to reduce the effects of moisture. TPD spectra of the adsorbates were obtained with a quadrupole mass spectrometer (ANELVA, AQA-200) that was located at ~35° with respect to the substrate surface normal.

4.3 Results

4.3.1 IRA spectra of water ice films with Cl_2 adsorbed. Figure 4.1 shows the IRA spectra of an amorphous ice film with and without exposure to Cl_2 gas. The IR absorption of the free OH group disappeared after deposition of Cl_2. Schaff and Roberts reported in their IRAS study that adsorption of hydrogen bond donors adsorbed on the surface of amorphous ice was accompanied by disappearance of the free OH group.[40] On amorphous ice a part of Cl_2 would form the hydrogen-bond-like interaction with the H atom of a free OH group.[26] On crystalline ice, because the surface concentration of free OH groups on a crystalline ice film was reported to be six times less than on an amorphous ice film,[40] Cl_2 interacts with the lone pair on the O atom.[4] An ab initio study predicted that Cl_2 pointed toward the lone pair on the O atom of $(OH_2)_4$.[23]

4.3.2 TOF spectra of photofragment Cl atoms from the 351 nm photodissociation.
4.3.2.1 Translational energy distributions. Figure 4.2 shows typical TOF spectra, $S(t)$,

of Cl and Cl* atoms obtained from the photolysis of Cl_2 adsorbed on amorphous and crystalline water ice films. The formation yield of Cl on amorphous ice was lower than on crystalline ice film by an order of magnitude. Both Cl and Cl* atoms have the same threshold TOF of 1.35 ± 0.05 μs. The Cl atoms have both fast and slow components in their broad TOF distributions, while the Cl* atoms have mostly fast one. The TOF spectra were simulated with a composite of normalized TOF functions, $S_G(t)$ and $S_{MB}(t)$. These functions correspond to a Gaussian distribution $P_G(E_t)$ and a flux-weighted Maxwell-Boltzmann translational energy distributions $P_{MB}(E_t)$, respectively:

$$S(a, r, t) = aS_G(t) + (1-a)S_{MB}(t), \tag{4.1}$$

$$P_G(E_t) = [w(2\pi)^{1/2}]^{-1}\exp[-2(E_t-<E_t>)^2/w^2], \tag{4.2}$$

$$P_{MB}(E_t) = (k_B T_{trans})^{-2} E_t \exp[-E_t/(k_B T_{trans})], \tag{4.3}$$

where a is a coefficient, t is the TOF of the photofragment, and w is the energy width. As marked in Figure 4.2, the TOF distribution consists of channels A (Gaussian) and B (Maxwell-Boltzmann). The angular distribution of the photofragments from the substrate, $\cos^n \theta$, $n = 2$, was adopted for channel A according to Giorgi et al.[35] The Gaussian distribution for Cl is characterized by $<E_t> = 0.38 \pm 0.02$ eV and $w = 0.37 \pm 0.02$ eV for both amorphous and crystalline ice. $<E_t>$ for Cl* atoms is higher than that of Cl by about 0.1 eV. For channel B, the TOF spectra of Cl* show a small contribution, because Cl* that is spin-orbit excited by 0.109 eV is easily relaxed to the ground-state Cl atom by collisional relaxation processes on the ice surface. The contribution of channel B is larger for Cl than Cl*. Thus, a broad angular distribution for channel B is expected if this channel is attributable to the photofragment atoms that are translationally relaxed by collisions with adsorbed Cl_2 on the ice surface and/or surface water molecules before leaving the ice surface. Hence, $n = 0$ was adopted for the angular distribution. The Maxwell-Boltzmann energy distribution of channel B is characterized by the average

energy $2k_B T_{trans}$ = 0.12 ± 0.01 eV. These translational energy parameters $<E_t>$ and $2k_B T_{trans}$ were found to be independent of photolysis laser intensity up to 5 mJcm^{-2}, pressure P up to 10 × 10^{-8} Torr, and the states of ice films (amorphous or crystalline). The time-integrated TOF signal intensity ratios $I(Cl^*)/I(Cl)$ were 0.20 ± 0.04 for both amorphous and crystalline ice films. After correction for the relative sensitivity of the each REMPI transition, the ratio of the quantum state population is $N(Cl^*)/N(Cl)$ = 0.21 ± 0.07. Other than channels A and B, a very weak signal appeared at the very fast TOF region, t = 1.2 μs. This signal intensity increased with P. Its translational energy distribution is consistent with the $Cl_2 \cdots Cl$ intermediate mechanism proposed by Giorgi et al.[35] However, the intensity was too weak to study further in the present experimental conditions.

A reference experiment was performed on the polycrystalline Au substrate with (111) domains. Cl_2 was deposited directly on Au. In this case, the average energy $<E_t>$ was 0.20 ± 0.02 eV for submonolayer coverage of Cl_2 while $<E_t>$ increased up to 0.35 ± 0.02 eV for the higher coverage. The production of the Cl fragments from Cl_2 adsorbed on an Au surface at 351 nm is attributed to the electron-mediated process for the submonolayer condition because photoabsorption by the Au substrate is much stronger than that of the thin Cl_2 layer. Hence, the surface-mediated photodissociation results in the low $<E_t>$ for the submonolayer coverage condition. However, for the higher coverage condition, the top layer of the multilayered Cl_2 is directly photolyzed.[35] Hence, the direct photoabsorption by Cl_2 molecules results in the higher $<E_t>$ = 0.35 ± 0.02 eV. $<E_t>$ of the multilayer Cl_2 adsorbed on Au is close to that for channel A on ice films (0.38 ± 0.02 eV). Since channel A for the present ice experiment results from the direct photodissociation of a monolayer of Cl_2 on water ice molecular layers, multilayered molecules, irrespective of water or chlorine, work in the same way as a soft surface for Cl atoms that are departing from the surface. The departing Cl atom is recoiling against an effectively infinite mass of the ice water surface. Due to strong interaction of the water ice surface with adsorbed Cl_2, the photofragments are translationally relaxed.

4.3.2.2 Effect of Cl_2 coverage on photodissociation yield. Figure 4.3 shows the total

Cl photodesorption yield as a function of P or Cl_2 coverage on amorphous and crystalline ice films. The total yield is defined as time-integrated Cl intensity of the TOF spectrum. The yield on crystalline ice film increases linearly up to $P \sim 2.5 \times 10^{-8}$ Torr, while that on the amorphous ice film increases linearly up to $P \sim 7.5 \times 10^{-8}$ Torr. The two different curvatures observed in Figure 4.3 suggest the formation of the first monolayer of Cl_2 on ice. Because of the larger effective surface area, P is higher for the amorphous ice film than the crystalline ice film. In addition, the photodissociation yield of Cl_2 on the amorphous ice film is lower than that on the crystalline ice by an order of magnitude.

Contributions of the slowly moving Cl photofragments in TOF distribution were measured as a function of $P = 2\text{-}5 \times 0^{-8}$ Torr. The ratio of $I_B/(I_A+I_B)$ was 0.3 for the amorphous ice film, which is slightly smaller than 0.4 on crystalline ice. I_A and I_B stand for intensities of the fast moving Cl photofragment (Channel A of Figure 4.2) and slow one (Channel B), respectively.

4.3.2.3 Laser intensity dependence and temporal dependence of Cl photofragment yields. The photolysis laser power dependence of the Cl signal intensity was measured for 0-5 mJ cm^{-2} at 351 nm. The signal intensity increased linearly with laser intensity. These results suggest that one photon is involved in the photodissociation processes. The typical laser intensity used in the present experiment was 1 mJ cm^{-2} $pulse^{-1}$ at 351 nm, which satisfies the condition of one-photon dissociation.

For measurement of the relative absorption cross section of Cl_2 on PCI and P-AWS, the Cl signal intensity decay was measured as a function of irradiation time after Cl_2 was deposited (less than 1 ML) on the ice films. Since the Cl_2 was not supplied on the film during measurement, the light intensity was reduced to 0.1-0.3 mJ/pulse. The residual amount of Cl_2 on an ice film is given by N;

$$N = N_0 \exp(-\sigma n_{h\nu}), \qquad (4.4)$$

where N_0 is the initial amount of Cl_2, σ is the photodissociation cross section.[41] $n_{h\nu}$ is the number of photons irradiated and ranged up to 2×10^{18} photons for crystalline ice and 40×10^{18}. The semilogarithmic plots of the signal intensities were approximated by a single-exponential decay. From an initial part of the slopes the absorption cross sections were determined to be $\sigma(ASW)/\sigma(PCI) = 0.04$-$0.06$. The fact that the relative absorption cross section is in good agreement with the relative yields ratio 0.06 from Figure 4.3 suggests that Cl_2 molecules adsorb randomly on the crystalline and amorphous ice film.

4.3.2.4 Polarization effect of the photolysis laser light on signal intensity. The polarization dependence of the photodesorption yield of Cl on the angle of polarization of the dissociation laser was investigated by changing the direction of the electric vector of the incident laser light from parallel (p-polarization) to perpendicular (s-polarization) with respect to the plane of incidence. The angle of incidence was fixed at $\pi/4$. The excimer laser light was linearly polarized using a pile-of-plates polarizer. The degree of polarization, ρ, of the dissociation laser was 0.88 at 351 nm, which was used for correction of the observed results. The pressure range was $P = 0.5$-5.0×10^{-8} Torr. The polarization ratios observed for the crystalline and amorphous ice (ASW) were $I_s/I_p = 1.2 \pm 0.1$ and 1.8 ± 0.2, respectively. For the P-ASW that was prepared by background dosing of water, $I_s/I_p = 0.35 \pm 0.05$. These results are shown in Table 4.1.

Because electron transfer from a metal surface through the water layer is prohibited, it is unlikely that the dissociation on the ice film takes place via surface-mediated processes.[42] As a test, Cl_2 was deposited directly on a polycrystalline Au substrate with (111) domains and was irradiated at 351 nm. The ratio I_s/I_p was 0.60 ± 0.03 at 351 nm, which was unchanged for $P = (1$-$4) \times 10^{-8}$ Torr. This ratio is close to what is calculated for Au metal photoabsorption, $(1 - R_s)/(1 - R_p) = 0.65$, where R_s and R_p are the reflection coefficients of the Au substrate. Another possible surface-mediated photoprocess involves excitation by the electric field induced on the Au surface, details of which are described in the Appendix. The theoretically calculated ratio is $I_s/I_p = 0.58$ for the randomly oriented adsorbate case.

4.3.3 Detection of photochemical products on the ice surface with TPD and REMPI.

TPD and REMPI experiments were performed to investigate photochemical products on and in amorphous ice films. TPD spectra were recorded after irradiating Cl_2 (1 ML) on an amorphous ice film (7 ML) at 90 K for several tens of minutes. The light source was a Xe lamp (ILCLX300UV, 300W) attached with a paraboloidal reflector, a water cell, and a UV-pass filter. During TPD, Cl^+, Cl_2^+, HCl^+, and H_2O^+ were detected by the mass spectrometer attached with an electron bombardment ionizer (70 eV). A search for other signals was unsuccessful. Cl^+ and Cl_2^+ appeared at 100-105 K. The TPD signal intensity of H_2O^+ peaked at 157 K. HCl^+ appeared mostly at 100-105 K, which corresponds to the Cl_2 desorption temperature. Weak HCl^+ signals appeared at 157 K, which corresponds to the H_2O sublimation temperature. In a separate TPD experiment without photoirradiation, HCl gas was deposited on an amorphous ice film. HCl^+ desorbed at 157 K. This result is in accord with the report of Graham et al. who recorded TPD spectra after exposing a 35 ML ice film on Pt(111) to gaseous Cl_2 at 100 K.[21] In their experiment HCl evolved from the ice surface at the H_2O sublimation temperature. Therefore, even if HCl were formed in or on the ice film, HCl signals would evolve at $T > 157$ K. However, in our experiment, most of the HCl^+ signals appeared at 100-105 K, which is much lower than the expected TPD temperature for HCl. These results imply that the HCl^+ signal did not come from the reaction of water with the photoprepared Cl atom but was produced by ion-molecule reactions in the ionizer of the mass spectrometer.

To avoid ion-molecule reactions in the ionizer, the REMPI method was utilized as a different way of detection of HCl from the 351 nm photodissociation of Cl_2 on amorphous ice at 90 K. First, the REMPI-TOF signal of HCl was sought by changing the time delay t and probe laser wavelength. Cl signals were observed, while no HCl signals were detected. Second, after irradiating Cl_2 on an amorphous ice film at 90 K for several minutes with the excimer laser at 351 nm, the substrate temperature was increased from $T = 90$ to 180 K while observing the REMPI signal of HCl $V^1\Sigma^+(v'=11)$-$X^1\Sigma^+(v''=0)$ Q(2) at 237.54 nm. The dose rate of Cl_2 exposure ranged from

1 to 50 ML. No HCl signal was detected. Hence, it was concluded that Cl atoms from the 351 nm photodissociation of Cl_2 on the ice films do not react with water molecules to form HCl on the water ice surface.

4.3.4 Resonance enhanced multiphoton ionization detection of Cl photofragments for temperature-programmed photodetachment spectroscopy (REMPI-TPPS). Photodesorbed Cl signal intensities were measured with the REMPI method as a function of substrate temperature T. The temperature ramp was 2 K s^{-1}. This experiment is characterized by the way in which the ice surface was exposed to the pulsed Cl_2 molecular beam between the photodissociation laser shots, as shown in the inset of Figure 3.1. We refer to this measurement as REMPI-TPPS. Figure 4.4 shows the REMPI-TPPS spectra of Cl from the 351 nm photodissociation of Cl_2 on amorphous and crystalline ice films. For both ice films, a monotonic decrease of the signal intensity was observed with T, because the sticking probability of Cl_2 on ice decreases with T.

The upper inset of Figure 4.4 shows a conventional TPD spectrum of H_2O on Au(111). H_2O desorbs from the Au(111) substrate mainly at 157 K and to some extent at 187 K. These desorption temperatures are in good agreement with values reported previously.[43] The lower inset spectrum of Figure 4.4 shows a REMPI-TPPS spectrum of NO from the 193 nm photodissociation of N_2O_4 adsorbed directly on a crystalline ice film. The spectrum is characterized by two different desorption temperatures, 155 and 173 K.[44] The 155 K peak corresponds to the H_2O sublimation temperature. The 173 K peak is due to the adduct formation of NO_2 with H_2O or due to trapped N_2O_4 in the ice film. For the crystalline ice film that has the grain boundaries, we can infer that some retained in the film. Due to the electronic quenching effect by the OH interaction, N_2O_4 trapped in the grain boundaries has a lower photodissociation quantum yield than that on the ice surface. This quenching effect disappears at the ice sublimation temperature where an enhancement of the NO signal intensity was observed. For the amorphous ice film, however the signal intensity decreased monotonically with T because N_2O_4 was not trapped in the ice.

The difference between REMPI-TPPS spectra for Cl_2 and N_2O_4 on crystalline ice

may result from the difference between the strengths of interaction with water ice. An ab initio study by Geiger et al. predicted the interaction energy for $Cl_2\cdots(OH_2)_4$ to be 0.12 ± 0.01 eV.[26] They described that four water molecules are sufficient for the calculation of binding geometry in a much larger number of water molecules. According to a TPD experiment by Rieley et al. the desorption activation energy of N_2O_4 from water ice surface is 0.41 eV.[5] The enthalpy of sublimation of H_2O is 0.41 eV.[45] Consequently, Cl_2 molecules on the ice film completely desorb from the water ice films below the water sublimation temperature and are not trapped in the grain boundaries of the crystalline ice film. Hence, for Cl_2 on both amorphous and crystalline ice films, the signal intensity decreases monotonically with increasing T.

4.4 Discussion

4.4.1 Photodissociation mechanisms of Cl_2 on ice films.
On the basis of the translational energy distributions of Cl observed in Figure 4.2, the broad Gaussian distribution (channel A) has an average energy $<E_t> = 0.38 \pm 0.02$ eV for both amorphous and crystalline ice films. The one-photon energy of 351 nm light corresponds to 3.53 eV, and the bond dissociation energy, D_0, of Cl_2 is 2.475 eV. The interaction energy for $Cl_2\cdots(OH_2)_4$ is 0.12 ± 0.01 eV.[23] If this interaction energy is representative of the bond energy of a Cl_2 to an ice surface, the maximum translational energy for each Cl atom would be $E_t^{max} = (h\nu - D_0 - 0.12)/2 = 0.46$ eV, close to what we observed for channel A, $<E_t> = 0.38 \pm 0.02$ eV. Thus, channel A could be attributable to the direct photodissociation of Cl_2 on the ice surface. In addition, the threshold TOF implies the translational energy of the fastest photofragment. Using 1.35 ± 0.05 μs and a flight length of 3.0 ± 0.3 mm, the maximum translational energy is 0.9 ± 0.2 eV, which is in agreement with the available energy of $h\nu - D_0 = 1.04$ eV in the 351 nm photodissociation of surface-adsorbed Cl_2. The broad distribution of the kinetic energy could be explained by relaxation processes on the ice surface.

Channel B, a flux weighted Maxwell-Boltzmann distribution with an average energy

of 0.12 ± 0.01 eV or $T_{trans} = 770 \pm 40$ K, is attributed to Cl atoms that have relaxed by collisions with water ice molecules and/or other Cl_2 molecules, losing a substantial amount but not all of their energy. If collisional relaxation is strong, the translational temperature of channel B would be expected to approach the substrate temperature, T. Cl atoms would be partially accommodated to the substrate temperature. However this totally relaxed channel was not observed in the present photodissociation of Cl_2 on ice. One notices that the calculated interaction energy for $Cl_2 \cdots (OH_2)_4$ (0.12 ± 0.01 eV) is weak compared to those for HOCl (0.38 eV) and HCl (0.27 eV) with such $(OH_2)_4$ water clusters because Cl_2 has no dipole moment, that is, electrostatic dipole-dipole interactions are mostly responsible for binding in the clusters $X \cdots (H_2O)_4$ (X = HOCl, HCl, H_2O, Cl_2).[23] Therefore, we infer that the non-observation of a lower temperature channel is attributed to the weak interaction energy between Cl_2 and H_2O.

4.4.2 Effect of interaction between Cl_2 and free OH groups on dissociation processes. The total Cl yields on amorphous and crystalline ice films are shown in Figure 4.3 as a function of pressure P that is a measure of Cl_2 exposure on the ice film. Rieley et al. reported that the curvature of an adsorption is correlated with the formation of the first molecular layer of the reactant in their experiment on N_2O_4.[3,5] In our experiment, the exposure or the pressure P required for formation of a monolayer of Cl_2 on the amorphous ice film is about 3 times larger than on the crystalline ice film, because the effective surface area is 3 times larger for the amorphous ice. The lower production yield of Cl photofragments from the monolayer Cl_2 on an amorphous film is due to the interaction between Cl_2 and the surface OH group, i.e., photoexcited Cl_2 is more rapidly quenched on an amorphous surface than on a crystalline surface. In Figure 4.3, for the coverage higher than monolayer, the increase rate of the total Cl yield is suppressed for crystalline ice, while it is enhanced for amorphous ice. Rieley et al. reported a suppression effect in the N_2O_4 photodissociation yield over a monolayer region on a water ice surface.[3,5] The enhancement on the amorphous ice after monolayer coverage suggests that the first layer of Cl_2 molecules covers the surface OH groups that quench the photoexcited Cl_2 molecules and hence the dissociation efficiency increases

with the coverage. These results indicate that the hydrogen-bond-like interaction between Cl_2 and OH on amorphous ice is stronger than the Cl_2-oxygen interaction of $Cl_2 \cdots OH_2$ on crystalline ice.

Using TPD and Fourier transform infrared reflection absorption spectroscopy (FTIRAS), Schaff and Roberts investigated the difference in surface chemical behavior between amorphous and crystalline ice.[40] As to the differences, there are four possible explanations; surface area, porosity, permeability, and the existence of the OH groups. FTIRAS measurements showed that adsorption of good hydrogen bond donors on amorphous ice surface is accompanied by the disappearance of the vibrational mode of the OH groups. For compounds not having hydrogen-bond-like interactions, the TPD spectra from amorphous and crystalline ice were essentially identical, whereas the spectra were different for compounds forming hydrogen-bond-like interactions. Therefore, they concluded that the differences in surface area, porosity and permeability were less significant factors in the interaction of adsorbates with ice surfaces. In the present experiment, the IR absorption of the OH group disappeared as a result of Cl_2 adsorption on amorphous ice film. The dissociation quantum yield is smaller on amorphous ice. These results are largely attributed to the existence of the free OH groups on the amorphous ice surface.

4.4.3 Adsorption states of Cl_2 on ice films and photodissociation quantum yields.
We examined the polarization dependent desorption yields of Cl. The ratios for the PCI, ASW, and P-ASW are shown in Table 4.1. For the two PCI surfaces, the ratios are the same. For crystalline ice, the water molecules form stacks of graphite-like sheets. The surface morphology is expected to be similar to each other for two PCI surfaces and independent of its preparation. Hence, the polarization ratios are the same for the two PCI surfaces. Assuming that (a) orientation of Cl_2 on the ice surface is random, and (b) the transition dipole moment of Cl_2 at 351 nm is mostly perpendicular to the molecular axis,[27] the theoretically calculated ratio is I_s/I_p = 1.3–2.7 (600 ML) and 1.8–2.7 (90 ML).(Details of the calculation are shown in Appendix.) These ratios are in fair agreement with what we observed for PCL, I_s/I_p = 1.2 ± 0.1.

43

The I_s/I_p ratio is higher for the ASW than for the crystalline ice film. Since the total signal intensity ratios of $I(Cl^*)/I(Cl)$ were close to each other, the relative contribution of $1_u(^1\Pi_\upsilon)$ and $0_u(B\ ^3\Pi_\upsilon)$ should be the same. The difference in the I_s/I_p ratio must be attributable to the different surface morphology. According to Kimmel et al., sticking on the sides of the existing structures in the film leads to some limited shadowing on the surface and the formation of relatively small pores.[46] For large angles of incidence of the water molecular beam in the case of the molecular beam preparation, the high points in the water ice film intercept a larger flux of the particles from the gas phase and thus cast "shadows" over the regions behind them on the surface. Their various simulation results suggest that the role of the shadowing instability and the amount of diffusion are of primary importance for determining the morphology of the ASW films grown by the directionally selected molecular beam method. For a large angle of incidence, the large pores associated with the shadowing remain for a 50 M film. The pores tend to form with a particular orientation that is roughly aligned with the incident beam direction. The film structure is coral-like columns and angled pores. As to the present I_s/I_p ratios, Cl_2 molecules adsorbed on the ASW prepared by molecular beam method have a tendency to be oriented along the growing angle of the ASW features.[47] A plausible explanation would be that the Cl_2 molecules trapped in the large and aligned pores have the lower dissociation quantum yield. Only Cl_2 adsorbed on the top surface, vertical with respect to the plane of the substrate, can dissociate with a relatively large dissociation quantum yield.

For ASW and P-ASW, the I_s/I_p ratios are totally different (Table 4.1). We do not understand in detail why the polarization ratio for the amorphous ice film (P-ASW) grown by background deposition is low compared to that for the direct adsorption ice film (ASW) prepared by the molecular beam, but the discrepancy is probably related to the large difference in morphology of the two ice films. According to Kimmel et al., the density of an ASW film is approximately 0.60, which is considerably lower than the background dosing film (P-ASW) because the P-ASW films prepared by background dosing have a random network of relatively small pores and there is no preferred

orientation for the pores. For incident angles greater than 45°, the average pore size begins to increase and there is a mixture of smaller pores and large pores.[46] A plausible explanation about the large difference in the I_s/I_p ratios is that an ice surface and a pore wall are characterized by dangling OH, and the adsorption energies on the defective surface with a large number of pores is higher than that on the nondefective surface because multi-hydrogen bond interaction can occur on the defective surface. The pores may provide unique adsorption sites with significantly lower barriers for formation of higher Cl_2 hydrates. If this is the case, then the phototransitions of Cl_2 adsorbed on ASW and P-ASW are not the same due to the difference in the degree of interaction of OH with Cl_2; that is, the contribution of the Cl_2 $0_u(B\ ^3\Pi_{0+})$ excited electronic state to the 351 nm absorption spectra increases. Thus, it would be reasonable to assume that a strong interaction of the free OH group with Cl_2 molecules affects on the dissociation dynamics.

4.5 Appendix

4.5.1 Photoexcitation of Cl_2 by the standing wave at the Au metal and adsorbate boundary. The absorption A_{mol} by an adsorbate will be dependent on its molecular orientation determining the direction of the transition dipole moment μ with respect to the total electric field vector $\mathbf{E}$ at the surface

$$A_{mol} \approx (\mathbf{E} \cdot \boldsymbol{\mu})^2 .$$
(A-1)

The induced field intensities parallel or perpendicular to the surface are calculated with complex refractive indexes. Details of the relevant electromagnetic theory are given by McIntyre[48] and Richter et al.[49] The mean-square electric field strength of the different components in the standing wave at the boundary is then given by assuming unity amplitude of the incident wave. The electric field intensities for Au for the incident angle $\phi = \pi/4$ are $|E_{Xp}|^2 = 0.29633$, $|E_{Ys}|^2 = 0.212778$, $|E_{Zp}|^2 = 0.94833$. The transition

dipole moment of Cl_2 is perpendicular to the molecular axis at 351 nm in the gas phase. A_{mol} has three components, A_X, A_Y, and A_Z. According to Figure 4.5, we assume that the detection probability is proportional to $2\pi r dr/(r^2 + l^2)$ for $l = 3$ mm and $0 \leqq r \leqq 6$ mm (Figure 4.5). For both crystalline and amorphous ice surfaces, the angular distribution of the fragments from surface is assumed to be $\cos^2\theta$ and independent of the angle α on the basis of our analysis of the TOF spectra. The $\cos^n\theta$ distribution (n = 2.15) was reported in the experiment on an LiF(001) surface by Giorgi et al.[35]

$$A_X = |E_{X,p}|^2 |\mu|^2 \left[\int (\cos\psi\cos\theta\cos\varphi - \sin\psi\sin\varphi)^2 \cos^2\theta\sin\theta \frac{2\pi r}{l^2 + r^2} d\psi d\varphi d\theta dr \right.$$
$$\left. + \int (-\cos\psi\cos\theta\sin\varphi - \sin\psi\cos\varphi)^2 \cos^2\theta\sin\theta \frac{2\pi r}{l^2 + r^2} d\psi d\varphi d\theta dr \right], \tag{A-2}$$
$$= 1.72\pi^3 |E_{Xp}|^2 |\mu|^2$$

$$A_Y = |E_{Y,s}|^2 |\mu|^2 \left[\int (\sin\psi\cos\theta\cos\varphi + \cos\psi\sin\varphi)^2 \cos^2\theta\sin\theta \frac{2\pi r}{l^2 + r^2} d\psi d\varphi d\theta dr \right.$$
$$\left. + \int (-\sin\psi\cos\theta\sin\varphi + \cos\psi\cos\varphi)^2 \cos^2\theta\sin\theta \frac{2\pi r}{l^2 + r^2} d\psi d\varphi d\theta dr \right], \tag{A-3}$$
$$= 1.72\pi^3 |E_{Yp}|^2 |\mu|^2$$

$$A_Z = |E_{Z,p}|^2 |\mu|^2 \left[\int (-\sin\theta\cos\varphi)^2 \cos^2\theta\sin\theta \frac{2\pi r}{l^2 + r^2} d\psi d\varphi d\theta dr \right.$$
$$\left. + \int (\sin\theta\sin\varphi)^2 \cos^2\theta\sin\theta \frac{2\pi r}{l^2 + r^2} d\psi d\varphi d\theta dr \right], \tag{A-4}$$
$$= 0.86\pi^3 |E_{Zp}|^2 |\mu|^2$$

where ψ, φ and θ are defined by Euler angles. Then, the signal intensity ratio, I_s/I_p is given by (A-5),

$$\frac{I_s}{I_p} = \frac{A_Y}{A_X + A_Z/\xi} = 0.58, \tag{A-5}$$

where

$$\xi = \left| \varepsilon_{eff} \right|^2 = \left| \sqrt{\varepsilon_{vac} \cdot \varepsilon_{sub}} \right|^2 = \left| \varepsilon_{sub} \right| = \left| n \right|^2 . \qquad \text{(A-6)}$$

ϕ is the angle of incidence ($\phi = 45°$ in this experiment). According to Ying and Ho the microscopic field that the surface-adsorbed molecules feel is equivalent to the geometric mean of the macroscopic fields between the vacuum and the substrate sides.[50] The effective dielectric constant of Au $\varepsilon_{eff} = 2.54$ was adopted for the calculation.

4.5.2 Photoexcitation of Cl$_2$ by the standing wave at the water ice film and adsorbate boundary. Since the water ice film is transparent at 351 nm and the Au substrate reflect light, the induced filed intensities at the ice film and adsorbate boundary are calculated for the ice-Au bilayer case with the complex refractive indexes. The results are a function of ice film thickness d. Using reported density of a porous crystalline ice (PCI) film (0.93 gcm^{-3})[51,52] and a calculated area for 8 water molecules (0.95×0.78 nm^2)[53], we estimate that our typical deposition condition of 600 ML corresponds to $d = 209$ nm. This estimate is reasonable according to a similar experiment for backfilling preparation of water ice films.[54] Due to uncertainty in these parameters, it is safe to say that $d = 210 \pm 20$ nm. For 90 ML of PCI, $d = 31 \pm 3$ nm. Using eqs A-5 and A-6 with $\varepsilon_{ice} = 3.2$, the ratios of I_s/I_p are calculated to be 1.3–2.7 (600 ML) and 1.8–2.7 (90 ML).

TABLE 4.1: Effect of states of ice film on polarization ratios

state of ice film	preparation of water ice film	Is/Ip^a
polycrystalline	direct adsorption and annealing[b]	1.2 ± 0.1
	background adsorption[c]	1.2 ± 0.1
amorphous	direct adsorption[d]	1.8 ± 0.2
	background adsorption[e]	0.35 ± 0.05

[a] $Cl(^2P_{3/2})$ signal intensity ratio for s-polarized photolysis laser over that for p-polarized laser. [b] After direct adsorption of water at 85 K with pulsed molecular beam, the ice film was annealed at 130 K. The state of the ice film is PCI (porous crystalline ice). [c] Prepared by background adsorption of water vapor at 130 K PCI. [d] Prepared by molecular beam method of water vapor at 85 K. The state of the ice film is ASW (amorphous solid water). [e] Prepared by background adsorption at 90 K. the state of the ice film is P-ASW (highly porous amorphous solid water).
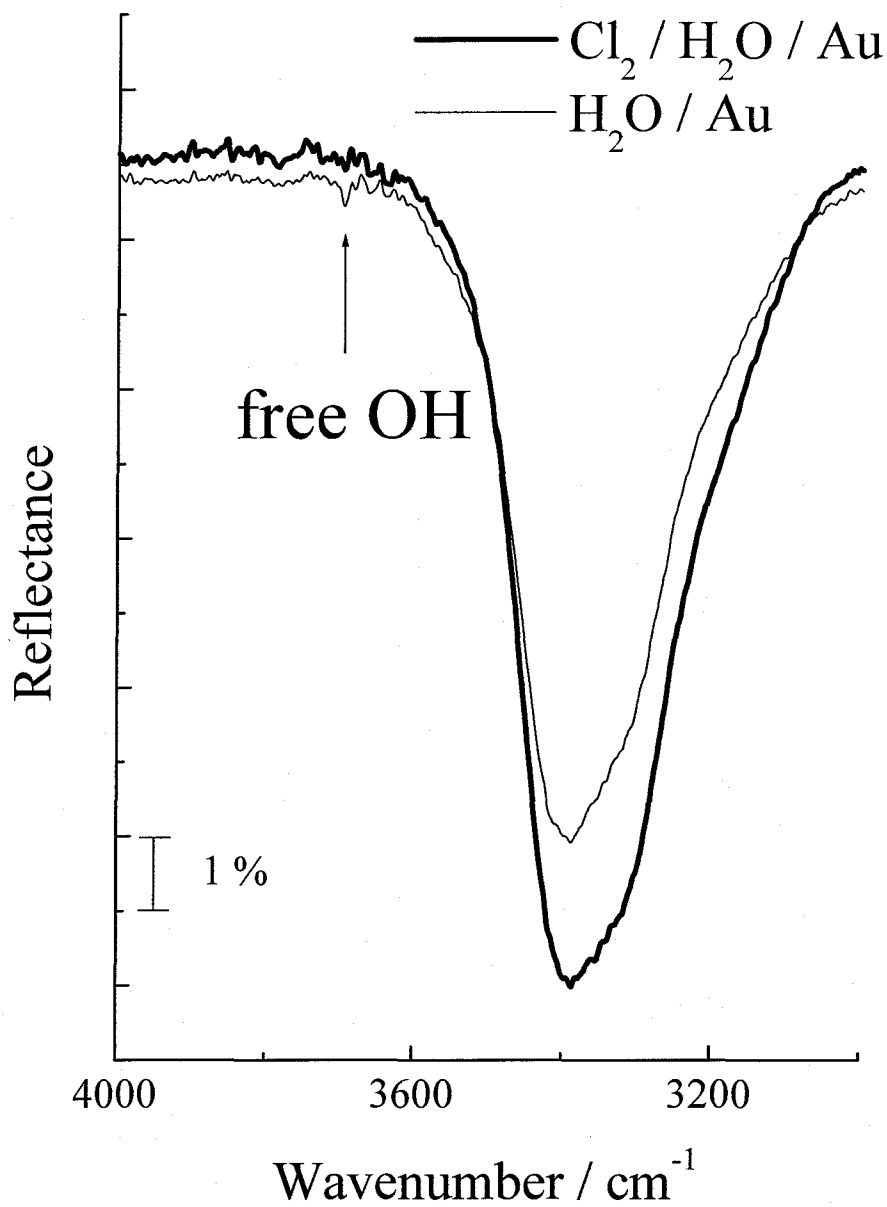
Figure 4.1 IR reflection absorption spectra of amorphous ice adsorbed on an Au(111) crystalline surface at 90 K with (solid curve) and without (fine curve) adsorption of Cl_2.
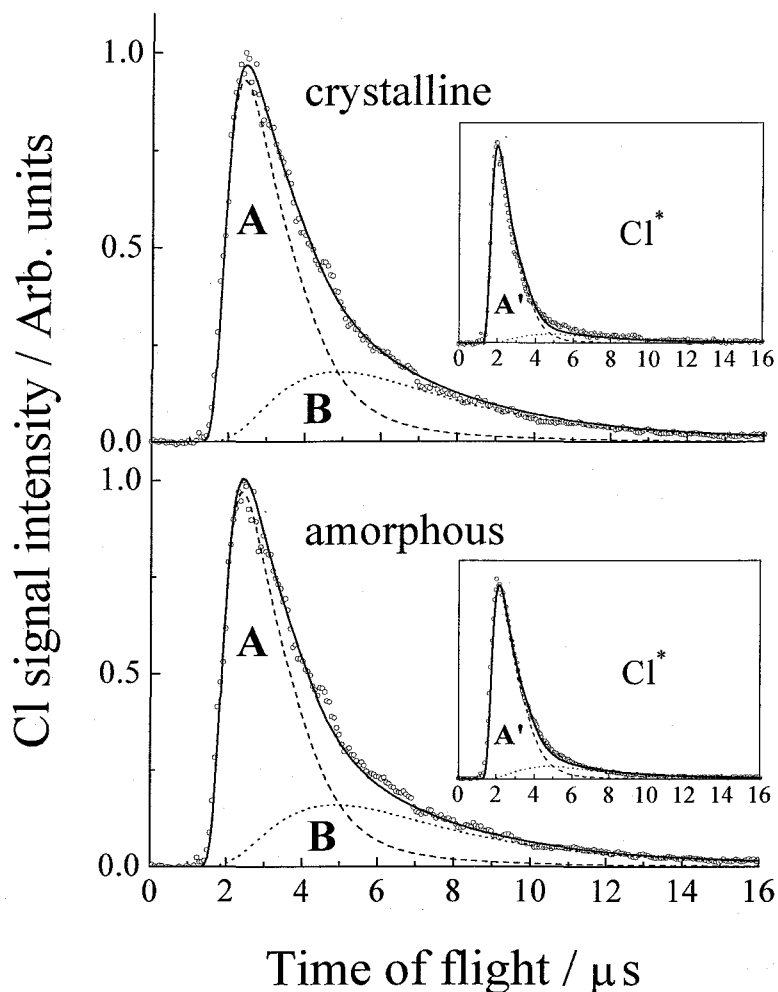
Figure 4.2 Time-of-flight spectra (open circle) of Cl($^2P_{3/2}$) from the 351 nm photodissociation of Cl_2 on a crystalline ice film (upper part) and amorphous one (lower part) as a function of delay time between dissociation and probe laser pulses. Substrate temperature T = 86 K and pressure P = 4×10^{-8} Torr. These spectra consist of two distributions; a Gaussian distribution marked with A (broken line) defined by eq 4.2 with $<E_t>$ = 0.38 ± 0.02 eV, and a flux-weighted Maxwell-Boltzmann translational energy distribution marked with B (dotted line) defined by eq 4.3 with T_{trans} = 770 ± 40 K. The smooth solid curves are the sum of these two distributions defined by eq. 4.1. The insets show the TOF spectra for Cl*($^2P_{1/2}$), which consist mostly of channel A. P = 0.3×10^{-8} Torr for crystalline ice and 4×10^{-8} Torr for amorphous ice.
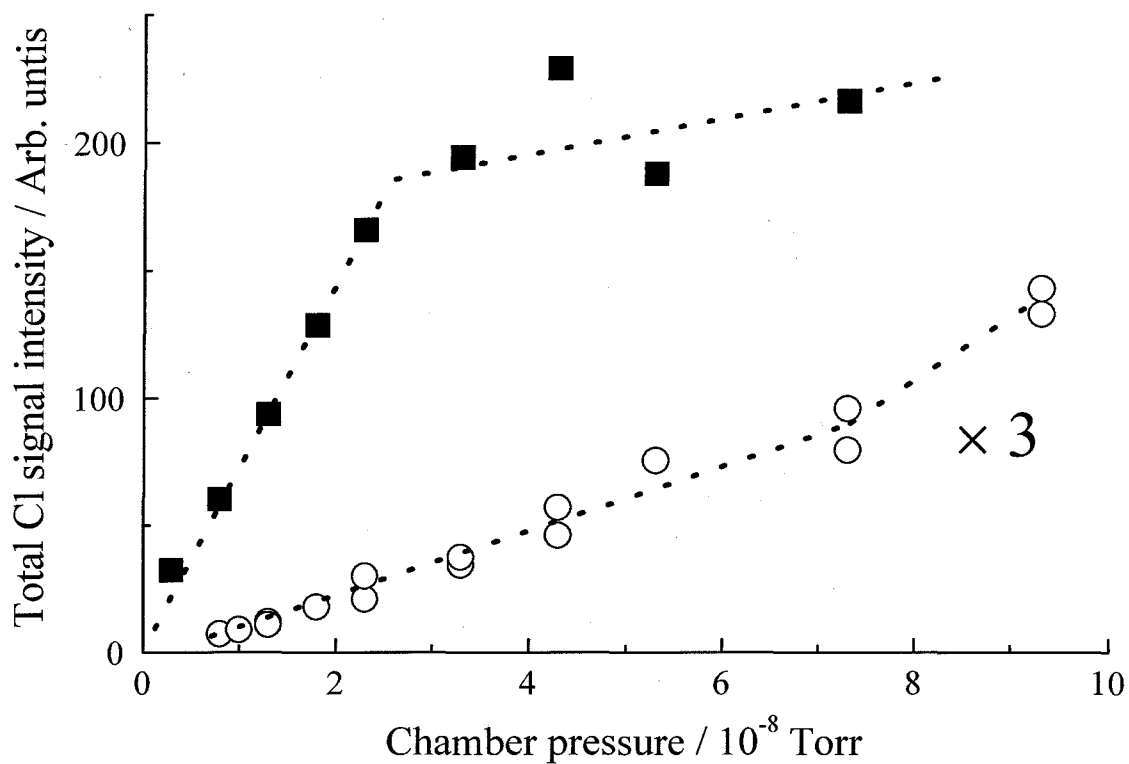
Figure 4.3 Effect of pressure, P, on time-integrated $Cl(^2P_{3/2})$ intensities of the time-of-flight spectra from the 351 nm photodissociation of Cl_2 on crystalline ice (filled square) and amorphous one (open circle). Substrate temperature T = 86 K. The curvatures suggest formation of the first monolayer of Cl_2 on the ice films.
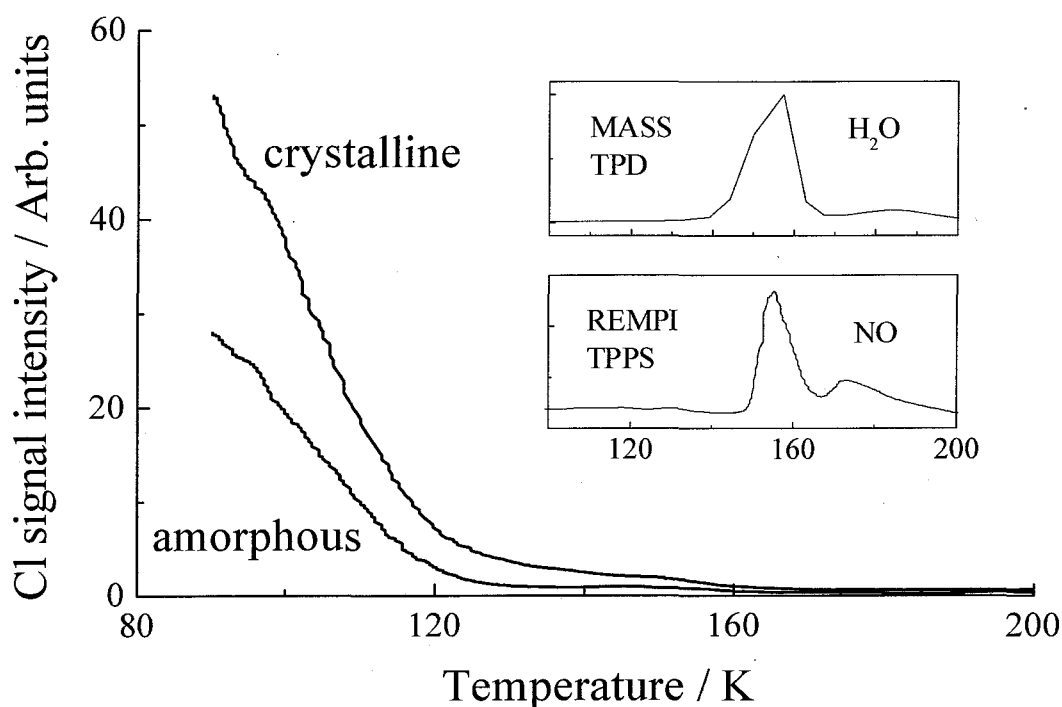
Figure 4.4 Temperature programmed photodetachment spectra (TPPS) of the REMPI signal intensities of $Cl(^2P_{3/2})$ from the photodissociation of Cl_2 on amorphous and crystalline ice films. $P = 10\times10^{-8}$ Torr. Note that this exposure was relatively high. The substrate temperature was increased at a rate of 2 K s^{-1}. The curve of the upper inset shows the temperature programmed desorption spectrum of H_2O on Au(111) measured by a mass spectrometer. (ref. 39) The lower inset shows a REMPI-TPPS of NO(v = 0, Q-head) from the 193 nm photodissociation of N_2O_4 on a crystalline ice film. (ref. 44)
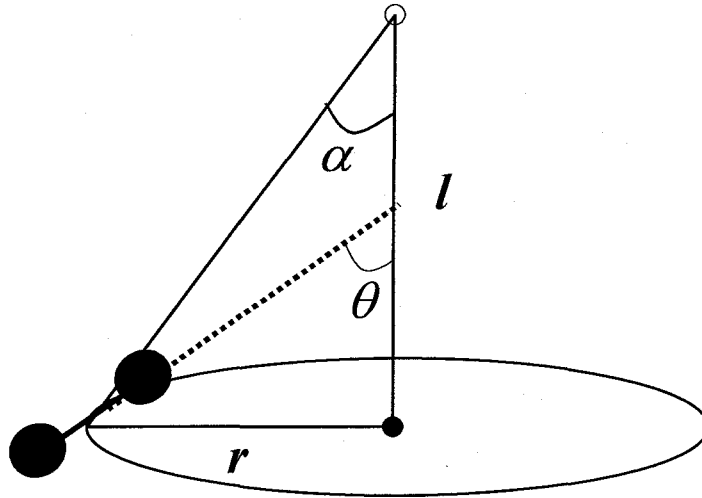
Detection point

Figure 4.5 Detection of the photofragment from the surface. A circle indicates an irradiation area on the substrate. l (= 3 mm) is the distance between the substrate and the detection point. r_{max}(= 6 mm) is the maximum radius of the irradiation area.

References and Notes

(1) Rieley, H.; Colby, D. J.; McMurray, D. P.; Reeman, S. M. *Surf. Sci.* **1997**, *390*, 243.

(2) Gane, M. P.; Williams, N. A.; Sodeau, J. R. *J. Chem. Soc., Faraday Trans.* **1997**, *93*, 2747.

(3) Rieley, H.; Colby, D. J.; McMurray, D. P.; Reeman, S. M. *J. Phys. Chem. B* **1997**, *101*, 4982.

(4) Graham, J. D.; Roberts, J. T.; Anderson, L. D.; Grassian, V. H. *J. Phys. Chem.* **1996**, *100*, 19551.

(5) Rieley, H.; McMurray, D. P.; Haq, S. *J. Chem. Soc., Faraday Trans.* **1996**, *92*, 933.

(6) Chaabouni, H.; Schriver-Mazzuoli, L.; Schriver, A. *Low Temp. Phys.* **2000**, *26*, 712.

(7) Dubowski, Y.; Colussi, A. J.; Hoffmann, M. R. *J. Phys. Chem. A* **2001**, *105*, 4928.

(8) Gerakines, P. A.; Moore, M. H.; Hudson, R. L. *Astron. Astrophys.* **2000**, *357*, 793.

(9) Moore, M. H.; Hudson, R. L.; Gerakines, P. A. *Spectrochim. Acta* **2001**, *47A*, 843.

(10) Sadtchenko, V.; Knutsen, K.; Giese, C. F.; Gentry, W. R. *J. Phys. Chem. B* **2000**, *104*, 2511.

(11) Sadtchenko, V.; Knutsen, K.; Giese, C. F.; Gentry, W. R. *J. Phys. Chem. B* **2000**, *104*, 4894.

(12) Sadtchenko, V.; Giese, C. F.; Gentry, W. R. *J. Phys. Chem. B* **2000**, *104*, 9421.

(13) Molina, M. J.; Tso, T.-L.; Molina, L. T.; Wang, F. C.-Y. *Science* **1987**, *238*, 1253.

(14) Tolbert, M. A.; Rossi, M. J.; Golden, D. M. *Science* **1988**, *240*, 1018.

(15) Hanson D. R.; Ravishankara, A. R. *J. Phys. Chem.* **1992**, *96*, 2682.

(16) Abbatt, J. P. D.; Molina, M. J. *Geophys. Res. Lett.* **1992**, *19*, 461.

(17) Johnsson, K.; Engdahl, A.; Oius, P.; Nelander, B. *J. Phys. Chem.* **1992**, *96*, 5778.

(18) Johnsson, K.; Engdahl, A.; Oius, P.; Nelander, B. *J. Mol. Struct.* **1993**, *293*, 137.

(19) Banham, S. F.; Horn, A. B.; Koch, T. G.; Sodeau, J. R. *Faraday Discuss.* **1995**, *100*, 3121.

(20) Donsig, H. A.; Herridge, D.; Vickerman, J. C. *J. Phys. Chem. A* **1998**, *102*, 2302.

(21) Graham, J. D.; Roberts, J. T. *J. Phys. Chem. B* **2000**, *104*, 978.

(22) Dahl, T.; Røeggen, I. *J. Am. Chem. Soc.* **1996**, *118*, 4152.

(23) Geiger, F. M.; Hicks, J. M.; de Dois, A. C. *J. Phys. Chem. A* **1998**, *102*, 1514.

(24) Liu, Z. F.; Siu, C. K.; Tse, J. S. *Chem. Phys. Lett.* **1999**, *311*, 93.

(25) Davey, J. B.; Legon, A. C.; Thumwood, J. M. A. *J. Chem. Phys.* **2001**, *114*, 6190.

(26) Ramondo, F.; Sodeau, J. R.; Roddis, T. B.; Williams, N. A. *Phys. Chem. Chem. Phys.* **2000**, *2*, 2309.

(27) Matsumi, Y.; Tonokura, K.; Kawasaki, M. *J. Chem. Phys.* **1992**, *97*, 1065.

(28) Maric, D.; Burrows, J. P.; Meller, R.; Moortgat, G. K. *J. Photochem. Photobiol. A: Chem.* **1993**, *70*, 205.

(29) Samartzis, P. C.; Sakellariou, I.; Gougousi, T.; Kitsopoulos, T. N. *J. Chem. Phys.* **1997**, *107*, 43.

(30) Samartzis, P. C.; Bakker, B. L;. Rakitzis, T. P.; Parker, D. H.; Kitsopoulos, T. N. *J. Chem. Phys.* **1999**, *110*, 5201.

(31) Alexander, A. J.; Kim, Z. H.; Kandel, S. A.; Zare, R. N.; Rakitzis, T. P.; Asano, Y.; Yabushita, S. *J. Chem. Phys.* **2000**, *113*, 9022.

(32) Liberman, V.; Hasse, G.; Osgood, R. M. *Jr. J. Chem. Phys.* **1992**, *96*, 1590.

(33) Kawasaki, M.; Sato, H.; Nishi, N. *J. Appl. Phys.* **1989**, *65*, 792.

(34) Cousins, L. M.; Leone, S. R. *Chem. Phys. Lett.* **1989**, *162*, 155.

(35) Giorgi, J. B.; Naumkin, F. Y.; Polanyi, J. C.; Raspopov, S. A.; Sze, N. S.-K. *J. Chem. Phys.* **2000**, *112*, 9569.

(36) Wei, X.; Miranda, P. B.; Shen, Y. R. *Phys. Rev. Lett.* **2001**, *86*, 1554.

(37) Regan, P. M.; Langford, S. R.; Ascenzi, D.; Cook, P. A.; Orr-Ewing, A. J.; Ashfold, M. N. R. *Phys. Chem. Chem. Phys.* **1999**, *1*, 3247.

(38) Zimmermann, F. M.; Ho, W. *Surf. Sci. Rep.* **1995**, *22*, 127.

In our simulation procedure for the TOF spectra, the following equation $I(t, L, r_s)$ was used as a signal intensity function, because a) multiphoton-ionization detection of Cl is performed at a point that has a flight length L and hence signal intensity is reduces by a factor of L^{-2}, and b) the Cl photofragments come out to the gas phase from the substrate at a radius r_s and hence signal intensity is enhanced by a factor of $2\pi r_s$: $I(t, L, r_s) = 2\pi S(t,$

L) $r_s L^{-2}$ (Figure 4.5)

(39) Sato, S.; Senga, T.; Kawasaki, M. *J. Phys. Chem. B* **1999**, *103*, 5063.

(40) Schaff, J. E.; Roberts, J. T. *J. Phys. Chem.* **1996**, *100*, 14151.

(41) Zhou, X.-L.; Zhu, X.-Y.; White, J. M. *Surf. Sci. Rep.* **1991**, *13*, 73.

(42) Gilton, T. L.; Dehnbostel, C. P.; Cowin, J. P. *J. Chem. Phys.* **1989**, *91*, 1937.

(43) Smith, R. S.; Huang, C.; Wong, E. K. L.; Kay, B. D. *Surf. Sci.* **1996**, *367*, L13

(44) Yabushita, A.; Inoue, Y.; Senga, T.; Kawasaki, M.; Sato, S. *J. Phys. Chem. A* submittted

(45) Thiel, P. A.; Madey, T. E. *Surf. Sci. Rep.* **1987**, *7*, 211.

(46) Kimmel, G. A.; Dohnálek, Z.; Stevenson, K.P.; Smith, R. S.; Kay, B. D. *J. Chem. Phys.* **2001**, *114*, 5295.

(47) Marinelli, F.; Allouche, A. *Chem. Phys.* **2001**, *272*, 137.

(48) McIntyre, J. D. E. *Adv. Electrochem. Electrochem. Eng.* **1973**, *9*, 68.

(49) Richter, L. J.; Buntin, S. A.; King, D. S.; Cavanagh, R. R. *Chem. Phys. Lett.* **1991**, *186*, 423.

(50) Ying, Z. C.; Ho, W. *J. Chem. Phys.* **1990**, *93*, 9089.

(51) Westley, M. S.; Baratta, G. A.; Baragiola R. A. *J. Chem. Phys.* **1998**, *108*, 3321.

(52) Brown, D. E.; George, S. M.; Huang. C.; Wong, E. K. L.; Rider, K. B.; Smith, R. S.; Kay, B. D. *J. Phys. Chem.* **1996**, *100*, 4988.

(53) Hara, Y.; Hashimoto, N. T.; Nagaoka. M. *Chem. Phys. Lett.* **2001**, *348*, 107.

(54) Scovell, D.L.; Pinkerton, T.D.; Medvedev, V.K.; Stuve, E.M. *Surf. Sci.* **2000**, *457*, 365.

Chapter 5

Ultraviolet Photodissociation Dynamics of Cl_2 and $CFCl_3$ Adsorbed on Water Ice Surfaces

Abstract

A difference in the UV photodissociation dynamics of chlorine and tricholorofluorocarbon has been observed when those molecules were adsorbed on water ice surfaces. This difference is mostly attributable to the difference in the interaction of the adsorbed molecule with surface water molecules of ice. In the photodissociation of Cl_2 at 300-414 nm, the branching ratios of the formation of Cl $(^2P_{1/2})$ with respect to $Cl(^2P_{3/2})$ are different from those reported in the gas phase photodissociation. However, in the photodissociation of $CFCl_3$ at 193 nm, the ratio is in good agreement with that reported in the gas phase photodissociation. The kinetic energy distributions of the photofragment chlorine atoms reflect the interaction between the adsorbates and the surface water molecules.

5.1 Introduction

Chemistry on water ice films depends on the nature of interaction between adsorbed molecules and ice surfaces. The interactions of adsorbed molecules with the surfaces of amorphous and crystalline water ice films were investigated using thermal desorption spectroscopy (TDS), infrared absorption spectroscopy (IRAS), and X-ray photoelectron spectroscopy[1,2] for carbon suboxide,[3] ozone,[4] thiophen,[5] cyanoacetylene,[6] chlorodifluoromethane,[7] ammonia,[8] and trichlorofluoromethane.[9] Theoretical calculations were carried out to study the interactions of small nonpolar compounds,[10] acetone and methanol,[11] hydrogen chloride and hydrogen fluoride[12] with ice surfaces. The reactivity of ice surfaces toward certain molecules varies appreciably with phase and morphology of ice. Schaff and Roberts reported compounds possessing a functional group capable of accepting a hydrogen bond from the OH group of water ice show one or more thermal desorption states from an amorphous ice surface that are absent from crystalline ice.[2]

Photochemical reactions on ice have attracted attention because of their relevance in atmospheric processes.[13,14] Ice mediates chemical- and radiation-induced processes in interstellar, cometary, or planetary conditions.[15] In this paper, we have performed photodissociation of Cl_2 and $CFCl_3$ by measuring the translational energy distributions and the spin-orbit branching ratios of the $Cl(^2P_{3/2})$ and $Cl^*(^2P_{1/2})$ photofragments. The low-temperature study of the interaction of Cl_2 with water ice surfaces was reported by Banham et al.[16] The desorption temperature of Cl_2 from an water ice surface is 110 K. A TPD study for the interaction of Cl_2 with an amorphous ice surface was reported by Graham and Roberts.[17] They found that an exposure of 0.09 L at 100 K is sufficient to saturate the surface with Cl_2, because Cl_2 does not condense into Cl_2 multilayers at 100 K. Cl_2 desorbed mainly at 125 K. A secondary ion mass spectrometric measurement by Donsig et al. implied that Cl_2 reacts with ice above 130 K to form HOCl and HCl.[18] The interaction between an water ice surface and $CFCl_3$ has been investigated experimentally.[9,19] Horn et al. have studied the adsorption of $CFCl_3$ on the D_2O ice

surface at 110 K using reflection-absorption infrared spectroscopy.[19] They conclude that CFCl$_3$ molecules are weakly and reversibly adsorbed onto the surface of ice film. According to Ogasawara et al. the bond between the ice surface and CFCl$_3$ is a hydrogen bond between chlorine and free OH.[9]

5.2 Experimental

Details of water ice films are described in chapter 3.

Surface photodissociation of Cl$_2$ adsorbed on crystalline and amorphous water ice surfaces was carried out in an ultrahigh vacuum chamber, which was equipped with two turbo molecular pumps in tandem, a pulsed molecular beam, an excimer laser, and a dye laser. The experimental details are described elsewhere.[20] In brief, ice films were prepared on polycrystalline Au substrates with (111) domains.[21] Two types of ice films were used in this experiment: porous amorphous solid water (P-ASW) and polycrystalline ice (PCI) films. The P-ASW film was grown by deposition of water on the polycrystalline Au substrate at 86-99 K with the backfilling method.[22-24] The PCI film was prepared by depositing water vapor at 130 K for 60 min and annealing for 25 min. The exposure was typically 1800 L (1 L = 1 × 10^{-6} Torr s), which resulted in the formation of 600 ML of H$_2$O on the Au substrate.[25] An amorphous ice film is characterized by the existence of free OH groups and the porosity of ice surface, while a crystalline ice film has grain boundaries.[20] The gas mixture of Cl$_2$ with N$_2$ diluent was introduced into a vacuum chamber and exposed with the backfilling method. CFCl$_3$ molecules without diluent was introduced into a vacuum chamber. The chamber pressure was 0.5 × 10^{-8} without sample molecules injection. From our previous experiment,[20] we supposed that Cl$_2$ or CFCl$_3$ formed a submonolayer on the ice films at 90 K after exposure of several L. Cl$_2$ was photodissociated at 300-414 nm with the YAG pumped dye laser (Lambda Physik, SCANmate, 1 mJcm^{-2}pulse^{-1} at UV). CFCl$_3$ was photodissociated at 193 nm with an ArF excimer laser (Lambda Physik, COMPex, 10 Hz, typically reduced to 0.4 mJcm^{-2}pulse^{-1} by optical filters). While the adsorbed

molecules were photoirradiated, the sample molecule was slowly introduced accordingly, in order to keep amount of the adsorbate constant. Actually, the sample molecule was introduced through a leakage valve, typically in the range of 10^{-9} Torr, to keep the signal intensity constant at a fixed time delay between photolysis and probe pulses. Another YAG pumped dye laser pulse (Lambda Physik, SCANmate, 0.2 mJpulse^{-1} at UV) was used to ionize the photofragment by (2 + 1) REMPI at 235.336 nm for Cl($^2P_{3/2}$) and 235.205 nm for Cl*($^2P_{1/2}$) with a lens (f = 0.20 m). For each spin-orbit state, the REMPI intensity, I, depends both on the quantum state population, N, and on the ionization efficiency. Thus, $I(Cl^*)/I(Cl) = [N(Cl^*)/N(Cl)] \times f$. The scaling factor f was reported to be 1.06 ± 0.17 by Regan et al.[26] The subsequent REMPI signals of the chlorine atoms were detected by a TOF mass spectrometer and normalized to the UV probe laser intensity. The distance, l, between the substrate and the detection region was varied from 3 to 5 mm to change the effective flight lengths for neutral photofragments, which was set typically to 3 mm. TOF spectra were taken as a function of time delay, t, between photolysis and probe pulses, which correspond to the flight time between the substrate and the detection region.

The TOF spectra were collected with the detector located along the surface normal. In order to simulate the obtained TOF spectra, we used a composite of normalized TOF functions, $S_G(t)$ and $S_{MB}(t)$. These functions correspond to a Gaussian translational energy distribution $P_G(E_t)$ and a flux-weighted Maxwell-Boltzmann translational energy distributions $P_{MB}(E_t)$, respectively. $P_G(E_t)$ is characterized by the average energy, $<E_t>$, and the energy width, w. $P_{MB}(E_t)$ is characterized by the average kinetic energy $<E_t>$ = $2k_B T_{trans}$ where k_B is the Boltzmann constant and T_{trans} is the translational temperature. Conversion from the energy distribution to the TOF distribution was performed using the Jacobian listed by Zimmerman and Ho.[27] The details of the simulation of the TOF spectra were described in our previous paper.[20]

$$S(C, t) = CS_G(t) + (1-C)S_{MB}(t), \tag{5.1}$$

$$P_\mathrm{G}(E_t) = [w(2\,\pi\,)^{1/2}]^{-1}\exp[-2(E_t\text{-}<E_t>)^2/w^2],$$ (5.2)

$$P_\mathrm{MB}(E_t) = (k_\mathrm{B}T_\mathrm{trans})^{-2}\,E_t\,\exp[-E_t/(k_\mathrm{B}T_\mathrm{trans})],$$ (5.3)

where C is a coefficient, and t the time of flight of the photofragments.

5.3 Results

5.3.1 Photodissociation of CFCl$_3$ on water ice surfaces at 193 nm.

Cl and Cl* photofragments from the 193 nm photodissociation of CFCl$_3$ adsorbed on amorphous and crystalline water ice surfaces were observed, which have both fast and slow components. Typical TOF spectra are shown in Figure 5.1. Solid curves are a best-fit $S(C, t)$ of eq 5.1. The fast component (channel A) is a Gaussian distribution. The slow one (channel B) is a flux-weighted Maxwell-Boltzmann distribution. Both Cl and Cl* photofragments have the same threshold TOF of 0.80 ± 0.05 μs. On the assumption that the angular distribution of the photofragments from the substrate is a function of $\cos^n \theta$, where θ is the desorption polar angle, the best fitting value of the exponent(n) for the TOF spectra was decided to be 2 for channel A. The Gaussian distribution for Cl is characterized by $<E_t>_\mathrm{Cl}$ = 0.42 ± 0.02 eV, and w = 0.91 ± 0.09eV, for both amorphous and crystalline ice. For Cl*, $<E_t>_{\mathrm{Cl}*}$ is 0.71 ± 0.03 eV and w = 0.65 ± 0.06eV. For the slow Maxwell-Boltzmann distribution, n = 0 was adopted for the angular distribution. The energy distribution is characterized by $2k_\mathrm{B}T_\mathrm{trans}$ = 0.09 ± 0.01eV (540 ± 50 K) for crystalline ice, and $2k_\mathrm{B}T_\mathrm{trans}$ = 0.17 ± 0.01eV (1000 ± 50 K) for amorphous ice. These translational energy parameters $<E_t>$ and $2k_\mathrm{B}T_\mathrm{trans}$ were found to be independent of photolysis laser intensity for 0.1-1 mJcm^{-2}pulse^{-1} and under an exposure of 1 L.

The contributions of channel B to the total TOF spectra of Cl on amorphous and crystalline ice are 35 ± 7 %, while that for Cl* is 49 ± 7 %. Table 5.1 summarizes these results for the energy distributions.

The time-integrated TOF signal intensity ratios $I(\mathrm{Cl}^*)/I(\mathrm{Cl})$ were 0.24 ± 0.02 for both

amorphous and crystalline ice surfaces. After correction for the relative sensitivity of the each REMPI transition, the ratio of the quantum state population is $N(Cl^*)/N(Cl) = 0.25 \pm 0.02$, which is close to the ratio observed in the gas phase photodissociation at 193 nm (Table 5.2).

5.3.2 Photodissociation of Cl_2 on water ice surfaces at 300-414 nm. The TOF spectra of Cl and Cl^* atoms from the photodissociation of Cl_2 on water ice surfaces are essentially the same as those described previously.[20] Figure 5.2 shows typical TOF spectra, $S(C, t)$, of Cl and Cl^* atoms from the 351 nm photodissociation of Cl_2. The exponent $n = 2$ for the angular distribution of the photofragments was adopted for channel A according to Giorgi et al.[28] The Gaussian distribution of Cl is characterized by $<E_t>_{Cl} = 0.38 \pm 0.02$ eV and $w = 0.37 \pm 0.02$ eV for both amorphous and crystalline ice. $<E_t>_{Cl^*}$ is 0.48 ± 0.02 eV and $w = 0.37 \pm 0.02$ eV. The average energies of channel B, $2k_BT_{trans}$, are 0.13 ± 0.01 eV for Cl and Cl^*. These translational energy parameters $<E_t>$ and $2k_BT_{trans}$ were found to be independent of photolysis laser intensity up to 5 mJcm^{-2}pulse^{-1}, under an exposure of 1 L and the states of ice surfaces (amorphous or crystalline).

The time-integrated TOF signal intensity ratios $I(Cl^*)/I(Cl)$ on polycrystalline ice surface at 300-414 nm are almost independent of the dissociation wavelengths as shown in Table 5.2. In the TOF spectra, the Cl atoms have an appreciable portion of the slow component in their broad TOF distributions while the Cl^* atoms have only a limited portion of this component in their narrow TOF distributions. The contributions of channel B to the total TOF spectra of Cl on amorphous and crystalline ice are $35 \pm 5\%$, while that for Cl^* is 13 ± 2 %. We assumed that a) the contribution of channel B should be the same for both Cl^* and Cl, and b) the electronically excited state Cl^* atoms are internally relaxed to the ground state Cl atom. Based on this assumption and after correction for the relative sensitivities, the population ratios, $N(Cl^*)/N(Cl)$, are listed in Table 5.2, which are different from those reported in the gas phase photodissociation.[29]

5.3.3 Effects of the states of water ice surfaces on Cl photofragment yields and photodissociation cross sections. The Cl signal intensity from the photodissociation of

CFCl$_3$ was 6 ± 2 times weaker on P-ASW than on PCI under the same exposure conditions, and that of Cl$_2$ was about 10 times weaker. For measurement of the relative photodissociation cross sections of CFCl$_3$ or Cl$_2$ on amorphous and crystalline ice surfaces, the decay curve of the Cl signal intensity was measured as a function of irradiation time after the sample molecules were once exposed on ice surfaces at 90 K under 1 L condition.

Since the photodissociation process follows a simple exponential law, eq 5.4 determines the photodissociation cross section, σ_{diss}.

$$N = N_0\exp(-\sigma_{diss}n_{hv}),\qquad\qquad (5.4)$$

where N is the residual amount of the sample molecules on an ice surface, N_0 the initial amount of the sample molecules, and n_{hv} the number of photons irradiated.[30] From the initial part of the slopes of these curves, we derived σ_{diss}, or the absorption cross section σ_{abs} times dissociation quantum yield ϕ, σ_{diss}(P-ASW)/σ_{diss}(PCI) = σ_{abs}(P-ASW)ϕ(P-ASW)/σ_{abs}(PCI)ϕ(PCI) = 1.2 for CFCl$_3$, and 0.15 for Cl$_2$.

5.3.4 Photodissociation of HCl on water ice sufaces at 193 nm. As a reference experiment, the ice surface at 89-93 K was exposed with a mixture gas of HCl and N$_2$ up to a few Langumir exposure, and then, was irradiated at 193 nm. No REMPI signal of chlorine atoms was observed. The interaction between HCl and ice is completely different from that for Cl$_2$ and CFCl$_3$.[31-33] By using a combination of the infrared transmission spectroscopy and Monte Carlo *ab initio* simulations, Devlin et al. reported that HCl dissolves into ice layers to form H$^+$ + Cl$^-$ at the surface of ice film even at 50 K.[32] The process of dissociation is shown in Figure 5.3. The three steps are the formation of a single Cl-H$\cdots$O hydrogen bond to a water molecule in the ice surface; the formation of a second O-H$\cdots$Cl hydrogen bond to a nearby dangling OH group; and the formation of an additional O-H$\cdots$Cl hydrogen bond, which is followed by dissociation of HCl to form a contact ion pair, in which the Cl$^-$ ion remains in contact with the newly formed H$_3$O$^+$ (hydronium) ion. In the final stage of dissociation, the H$^+$

ion (a proton) diffuses away from the Cl⁻ ion along the ice surface. Near 90 K, the formation of contact hydronium-chloride ion pairs abruptly occurs, resulting in an ionic hydrate layer rich in Zundel cations.[34] Thus, no photodissociation of HCl occurred on the ice surface at 89-93 K.

5.4 Discussion

5.4.1 Photodissociation mechanisms of $CFCl_3$ on water ice surfaces.

The photodissociation of $CFCl_3$ at 193 nm in the gas phase leads to the following reaction with a non-thermal translational energy distribution for the photofragments:[35]

$$CFCl_3 + h\nu \rightarrow CFCl_2 + Cl \qquad (5.5)$$

At higher laser fluence a fraction of the nascent $CFCl_2$ radicals absorbs a further photon and dissociates into $CFCl + Cl$ in the gas phase. In the present experiment since ArF laser fluence is less than 0.4 $mJcm^{-2}pulse^{-1}$, this secondary process does not occur. Therefore, reaction 5.5 is the dominant primary process. The UV photodecomposition of $CFCl_3$ on an ice surface was studied by Ogasawara and Kawai.[9] They reported no IR absorption peaks assignable to adsorbed $CFCl_2$ in IRAS during the irradiation with 193 nm light. Because $CFCl_3$ is weakly and reversibly adsorbed onto the surface of ice film, the $CFCl_2$ fragment was removed from the surface immediately after photodecomposition.[19]

Based on the thermodynamic data, $D_0(CFCl_2-Cl) = 3.25$ eV, and the maximum available energy for the 193 nm photodissociation would be 3.17 eV. In the present experiment, the maximum translational energy of the Cl photofragment, $E_t^{max}(Cl) = 2.6 \pm 0.3$ eV from the threshold TOF gives the maximum center-of-mass translational energy, E_t^{max} (Cl + $CFCl_2$) = 3.5 ± 0.4 eV, which is in fair agreement with the calculated maximum available energy. Thus, the fast TOF component with the Gaussian distribution could be attributable to the direct photodissociation of $CFCl_3$ on the ice

surface. In the gas phase, the average kinetic energy of the product chlorine atoms from the photodissociation of $CFCl_3$ at around 190 nm was reported to be 1.0 eV.[35,36] Based on the average translational energies $<E_t>$ of Table 5.1, the energy relaxation of the chlorine photofragments is efficient on the ice surface. Due to rapid energy flow to ice, some of chlorine photofragments from the photodissociation of $CFCl_3$ are translationally relaxed by surface water molecules. Thus, the average kinetic energy $<E_t>$ of channel A is lower than that in the gas phase. The discrepancy with $<E_t>_{Cl}$ – $<E_t>_{Cl*}$ could be due to the fact that the Cl channel deposits a greater fraction of available energy in $CFCl_2$ internal excitation.[37,38]

For Channel B processes, flux weighted Maxwell-Boltzmann distributions with $2k_B T_{trans}$ = 0.09 ± 0.01eV for PCI and 0.17 ± 0.01eV for P-ASW were observed. This process is attributed to the photofragment atoms that have translationally relaxed by collisions with water-ice molecules and/or other $CFCl_3$ molecules.

The branching ratios $[Cl^*]/[Cl]$ from the 193 nm photodissociation of $CFCl_3$ on the ice surfaces are essentially the same as that in the gas phase. The interaction of $CFCl_3$ with the ice surface is so limited that the electronic structure of the molecule is not affected by adsorption on ice. In fact, the solubility of $CFCl_3$ in water is 0.0086 mol $kg^{-1}bar^{-1}$, which is much lower than 0.095 mol $kg^{-1}bar^{-1}$ for Cl_2.[39,40]

5.4.2 Photodissociation mechanisms of Cl_2 on water ice surfaces.

Adsorption states of Cl_2 on ice surfaces have been described in our previous paper.[20] We examined the polarization dependent yields of Cl on water ice surfaces with s- and p-polarized dissociation laser light. Supposing Cl_2 is randomly oriented on the ice surface, the theoretically calculated polarization ratio is I_s/I_p = 4/3. This ratio is close to what we observed for PCI, I_s/I_p = 1.2 ± 0.1. Therefore, orientation of Cl_2 on the ice surface is likely to be random.

Based on the thermodynamic data, $D_0(Cl-Cl)$ = 2.475 eV, the maximum available energy for the 351 nm photodissociation would be 1.1 eV. The interaction energy for Cl_2 $\cdots(OH_2)_4$ is 0.12 ± 0.01 eV.[41] The maximum translational energy for each Cl atom is calculated to be E_t^{max} = $(h\nu - D_0 - 0.12)/2$ = 0.46 eV. This value is close to the average

energy we observed for channel A, that is, 0.38 ± 0.04 eV for Cl, and 0.48 ± 0.04 eV for Cl*. Thus, channel A could be attributable to the direct photodissociation of Cl$_2$ on the ice surface.

According to a theoretical calculation by Bianco,[42] Cl$_2$ molecules adsorbed on the surface water molecules do not nucleate due to repulsive force between Cl$_2$ molecules. Actually Cl$_2$ does not condense into Cl$_2$ multilayers at 100 K.[17] The hydrolysis of molecular chlorine and its reverse reaction have been studied by *ab initio* molecular dynamics.[43] The hydrolysis reaction involves Cl$_2$ and H$_2$O molecules to produce solvated chlorine and hydrogen ions. Static secondary ion mass spectrometry measurements reported by Donsig et al. imply that Cl$_2$ reacts with ice above 130 K to form HOCl and HCl.[18] Therefore, Cl$_2$ strongly interacts with water molecules of the ice surface. The solubility of Cl$_2$ in water is much larger than that of CFCl$_3$.[39,40] Hence, the reaction dynamics differs from that for CFCl$_3$.
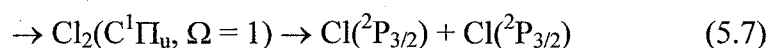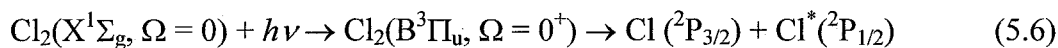
5.4.3 The interaction between ice and molecules. Sadtchenko et al. reported that CCl$_4$ adsorption on ice prepared at 130 K results in the formation of metastable two-dimensional islands, while CCl$_4$ adsorption on ice prepared at 95 K proceeds through formation of three-dimensional clusters in the pores of microscopically rough ice.[44] CFCl$_3$ is likely to have the similar nature to CCl$_4$ on an ice surface.[19] Based on the study for CCl$_4$, it is likely that CFCl$_3$ adsorbed on the ice surface can nucleate. Therefore, CFCl$_3$ photoprepared at 193 nm is electronically quenched efficiently. The photofragments from the photodissociation of isolated CFCl$_3$ adsorbed on the ice surface are mostly detected. Hence, the photodissociation dynamics resemble that in the gas phase and the ratios σ_{abs}(P-ASW)/σ_{abs}(PCI) and ϕ(P-ASW)/ϕ(PCI) are considered to be close to unity. Actually the ratio σ_{abs}(P-ASW)ϕ(P-ASW)/σ_{abs}(PCI)ϕ(PCI) was 1.2. However, under the same exposure condition of CFCl$_3$ on the higher porous ice surface (P-ASW) or the lower porous ice surface (PCI), the Cl signal intensity from the photodissociation was weaker on the P-ASW surface than the PCI surface. This can be explained by assuming that the nucleation occurs more heavily on P-ASW than PCI, that is, the electronic quenching is more efficient on P-ASW than on PCI.

According to Geiger et al.[41] and Bianco,[42] Cl_2 molecules on the ice surface interact with water with attractive force of the order of 0.1 eV. Due to the repulsion force between Cl_2, nucleation cannot occur.[17] Hence, the electronic quenching of the photoprepared Cl_2 by neighbor Cl_2 would not occur. the Cl signal intensity from the photodissociation was weaker on the P-ASW surface than the PCI surface, and also the ratio $\sigma_{abs}(\text{P-ASW})\phi(\text{P-ASW})/\sigma_{abs}(\text{PCI})\phi(\text{PCI})$ was 0.15. Photoprepared Cl_2 is more rapidly electronically quenched on the P-ASW surface than on the PCI surface due to the interaction between Cl_2 and the surface water. In other words, the ratio $\phi(\text{P-ASW})/\phi(\text{PCI})$ is much less than unit because the surface OH groups are more abundant on P-ASW than PCI, which interact with Cl_2. Hence, the photodissociation dynamics on ice is different from that in the gas phase.

5.4.4 Adiabaticity of Cl_2 potential curves. The water-Cl_2 complex, Cl_2-H_2O has a dipole moment of 0.24 Debye, and Cl_2-$3H_2O$ has that of 0.54 Debye, which are calculated by Bianco at the MP2 level of theory using effective core potentials for all the heavy atoms.[42] The bond length of Cl_2 (2.011 A in the isolated molecule) is enlongthened to 2.037 A for Cl_2-$3H_2O$.[42] A schematic diagram of a chlorine molecule adsorbed on the surface water molecules is depicted in Figure 5.4. Since the interaction of the adsorbed Cl_2 with H_2O is relatively strong and the potential curves are strongly distorted, adiabaticities of the Cl_2 potential curves change so much that the spin-orbit branching ratios of the $Cl(^2P_{3/2})$ and $Cl^*(^2P_{1/2})$ photofragments are different from the isolated molecules.

When Cl_2 absorbs a UV photon, it dissociates through either the parallel or perpendicular transitions:

$$Cl_2(X^1\Sigma_g, \Omega = 0) + h\nu \rightarrow Cl_2(B^3\Pi_u, \Omega = 0^+) \rightarrow Cl\,(^2P_{3/2}) + Cl^*(^2P_{1/2}) \qquad (5.6)$$

$$\rightarrow Cl_2(C^1\Pi_u, \Omega = 1) \rightarrow Cl(^2P_{3/2}) + Cl(^2P_{3/2}) \qquad (5.7)$$

Gaseous Cl_2 has an absorption continuum in the region of 300-400 nm and weak

absorption at $\lambda < 250$ nm. The absorption spectrum at 351 nm is dominated (99%) by the C $1_u(^1\Pi_u)$ state that is correlated with the formation of two Cl atoms, while the 0_u(B $^3\Pi_u$) state which produces one Cl^* and one Cl contributes to photoabsorption less than 1%.[29,45] The Cl^*/Cl branching ratio, following gas phase photolysis of Cl_2 has been extensively measured in the region 310-470 nm and results show variation in the dissociation wavelength. Samartzis et al. reported the branching ratios for the Cl_2 photodissociation at 310-470 nm.[29] Their branching ratios $N(Cl^*)/N(Cl)$ at 300, 325, 351, 400 and 414 nm, are 0, 0, 0.003, 0.43, and 0.66, respectively. However, those on PCI at the corresponding wavelengths are 0.30, 0.29, 0.29, 0.24, and 0.15, respectively (Table 5.2).

The nuclear kinetic energy operator gives rise to a non-adiabatic interaction on the adiabatic potential.[46] The Rosen-Zener-Demkov (RZD) type non-adiabatic transition from the C $^1\Pi_u$ state to the third 1_u ($^3\Sigma^+_{1u}$) state of Cl_2 that is correlated adiabatically with Cl + Cl^* is responsible for the production of Cl^*.[47,48] The photodissociation wavelength dependence of the product branching ratio $N(Cl^*)/N(Cl)$ depends on the degree of interaction of the potential curve.[29] The ratios are well reproduced by the RZD transition mechanism.

The 330 nm absorption band of the adsorbed chlorine is expected to be shifted only slightly toward shorter wavelength from an analogy with bromine and iodine water complexes.[49] Thus, the UV Franck-Condon region for Cl_2 is not affected by the interaction with ice. The interaction of the adsorbed Cl_2 with H_2O is relatively strong at the asymptotic region of the potential curves. Potential energies rise at the longer internuclear distances. Thus, the degree of the RZD interaction between the electronically excited potential curves of Cl_2 could be similar even though the photoprepared state is different at different UV wavelength. In other words, the product branching ratios $N(Cl^*)/N(Cl)$ become almost independent of the positions of Franck-Condon excitation (or the initial excitation position of the potential curves) , but depend solely on the RZD interaction at longer internuclear distances.

TABLE 5.1: Average translational energies of $Cl(^2P_{3/2})$ and $Cl^*(^2P_{1/2})$ photofragments from $CFCl_3$ and Cl_2 adsorbed on ice surfaces

parent molecule	detected species	Gaussian distribution for Channel A		Maxwell-Boltzmann distribution for Channel B		
		average energy[a] (eV)	coefficient C^a	average energy[a] (eV)	translational temperature[a] (K)	coefficient C^a
CFCl₃	Cl	0.42 ± 0.02	0.65 ± 0.07	0.17 ± 0.01 (P-ASW)[b] 0.09 ± 0.01 (PCI)[c]	1000 ± 50 (P-ASW) 540 ± 50 (PCI)	0.35 ± 0.07
	Cl*	0.71 ± 0.03	0.49 ± 0.07	0.17 ± 0.01 (P-ASW) 0.09 ± 0.01 (PCI)	1000 ± 50 (P-ASW) 540 ± 50 (PCI)	0.49 ± 0.07
Cl₂	Cl	0.38 ± 0.04	0.65 ± 0.05	0.13 ± 0.01	770 ± 40	0.35 ± 0.05
	Cl*	0.48 ± 0.04	0.87 ± 0.02	0.13 ± 0.01	770 ± 40	0.13 ± 0.02

[a] Average energy, translational temperature and coefficient appear in eq. 5.1 [b] P-ASW stands for porous amorphous solid water ice surface. [c] PCI stands for polycrystalline ice surface.

TABLE 5.2: Branching ratios of $Cl^*(^2P_{1/2})$ and $Cl(^2P_{3/2})$ from photodissociation of $CFCl_3$ and Cl_2 on a polycrystalline ice surface and in the gas phase

adsorbate	wavelength (nm)	ice surface		gas phase
		$I(Cl^*)/I(Cl)^a$	$N(Cl^*)/N(Cl)^b$	
$CFCl_3$	193	0.24 ± 0.02	0.25 ± 0.02	0.30^c
Cl_2	300	0.20 ± 0.03	0.30 ± 0.05	0^d
	325	0.19 ± 0.02	0.29 ± 0.03	0^d
	351	0.19 ± 0.01	0.29 ± 0.02	0.003^d
	400	0.16 ± 0.01	0.24 ± 0.02	0.43^d
	414	0.10 ± 0.01	0.15 ± 0.02	0.66^d

^{a} Experimental signal intensity ratio. ^{b} Population ratio after corrected for detection efficiency and electronic relaxation. See text for details. ^{c} From ref. 38. ^{d} From ref. 29.
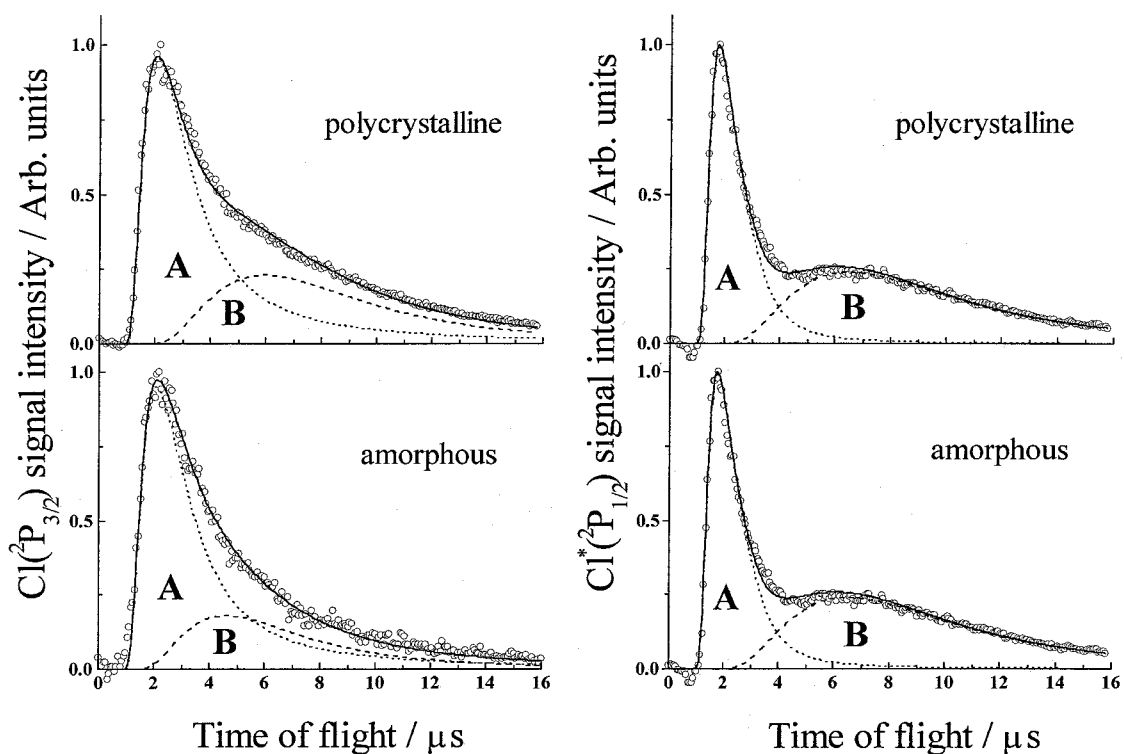
Figure 5.1 Time-of-flight spectra of $Cl(^2P_{3/2})$ and $Cl^*(^2P_{1/2})$ from the 193 nm photodissociation of $CFCl_3$ on a polycrystalline ice surface and an amorphous ice surface. Ice temperature $T = 90$ K, 1 L of $CFCl_3$. These spectra are resolved into two distributions: a Gaussian translational energy distribution marked by A with $<E_t>_{Cl} = 0.42 \pm 0.02$ eV and $<E_t>_{Cl^*} = 0.71 \pm 0.03$ eV for both amorphous and crystalline ice surfaces; a flux-weighted Maxwell-Boltzmann translational energy distribution marked by B with $T_{trans} = 540 \pm 50$ K for a crystalline ice surface and 1000 ± 50 K for an amorphous ice surface. The smooth solid curves correspond to the sum of these two distributions defined by eq 5.1. Details of curve fitting were described in ref. 20.
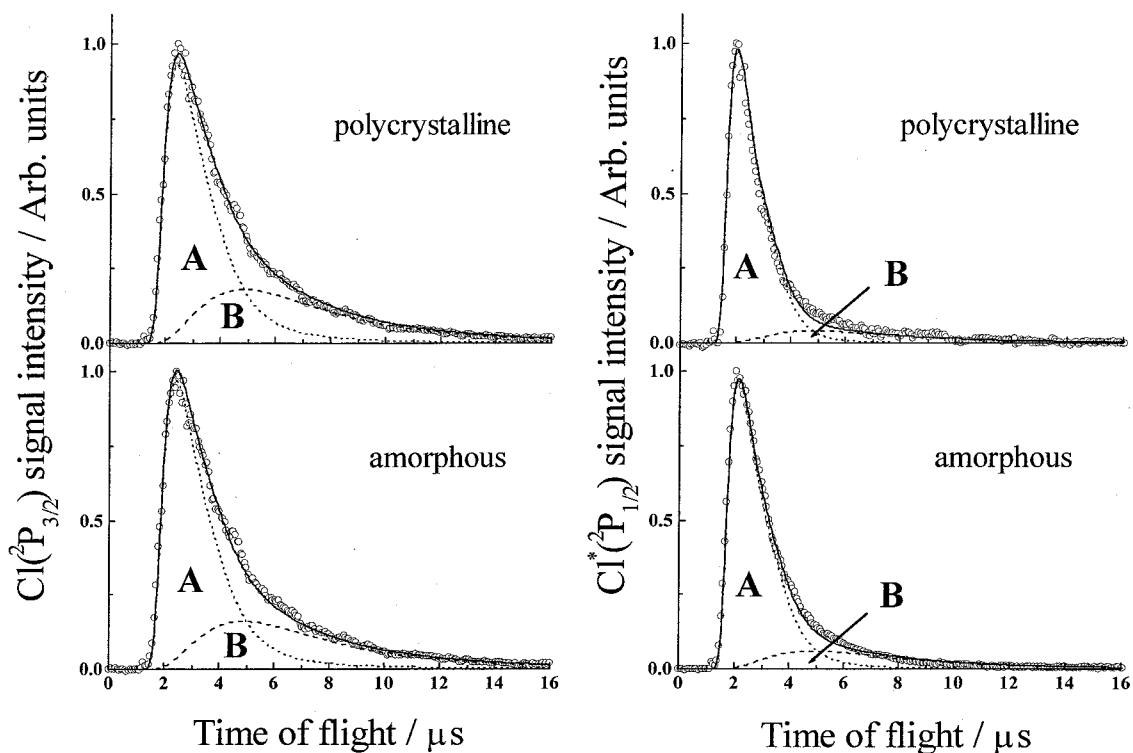
71

Figure 5.2 Time-of-flight spectra of $Cl(^2P_{3/2})$ and $Cl^*(^2P_{1/2})$ from the 351 nm photodissociation of Cl_2 on a crystalline ice surface and an amorphous ice surface. Ice temperature T = 86 K, 1 L of Cl_2 for crystalline and amorphous ice surfaces. Gaussian translational energy distribution marked by A is characterized with $<E_t>_{Cl}$ = 0.38 ± 0.04 eV, and a flux-weighted Maxwell-Boltzmann translational energy distribution marked by B with T_{trans} = 770 ± 40 K. The smooth solid curves are the sum of these two distributions. The TOF spectra for $Cl^*(^2P_{1/2})$, which consist mostly of channel A with $<E_t>_{Cl^*}$= 0.48 ± 0.04 eV.
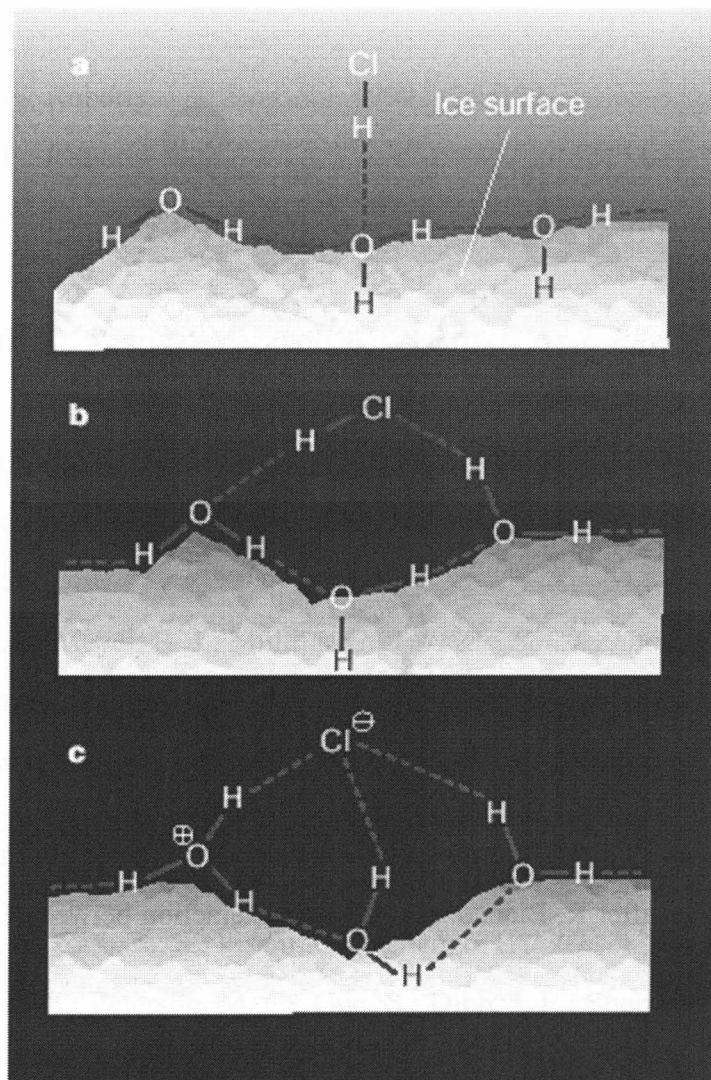
72

Figure 5.3 Dissociation of hydrogen chloride on the surface of ice.

a, First, a single strong hydrogen bonds forms, linking the HCl molecule to an oxygen atom on the ice. b, A second hydrogen bond forms between the Cl atom and a dangling OH group. c, Finally, a third hydrogen bond connects another dangling OH group to the Cl atom, followed by dissociation of HCl, leading to a contact ion pair of chloride ion and H_3O^+ ion. From ref. 31.
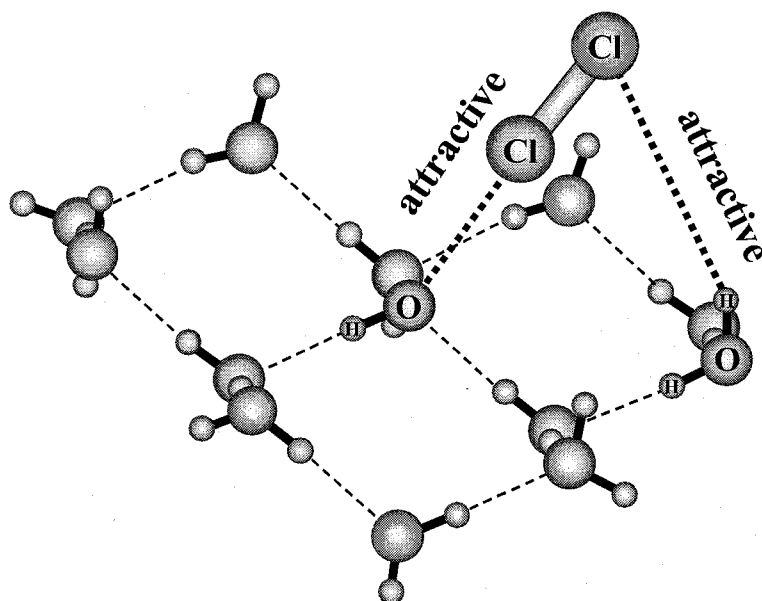
Figure 5.4 A schematic diagram of a chlorine molecule adsorbed on the surface water molecules after R. Bianco. ref. 42. The interaction between Cl_2 and H_2O is attractive.

References and Notes

(1) Schaff, J. E.; Roberts, J. T. *Surf. Sci.* **1999**, *426*, 384.

(2) Schaff, J. E.; Roberts, J. T. *J. Phys. Chem.* **1996**, *100*, 14151.

(3) Couturier-Tamburelli, I.; Chiavassa, T.; Pourcin, J. *J. Phys. Chem. B* **1999**, *103*, 3677.

(4) Chaabouni, H.; Schriver-Mazzuoli, L.; Schriver, A. *J. Phys. Chem. A* **2000**, *104*, 6962.

(5) Haberkern, H.; Haq, S.; Swiderek, P. *Surf. Sci.* **2001**, *490*, 160.

(6) Borget, F.; Chiavassa, T.; Allouche, A.; Marinelli, F.; Aycard, J. *J. Phys. Chem. A* **2000**, *104*, 6962.

(7) Safarik, D. J.; Meyer, R. J.; Mullins, C. B. *J. Vac. Sci. Technol. A* **2001**, *19*, 1537.

(8) Ogasawara, H.; Horimoto, N.; Kawai, M. *J. Chem. Phys.* **2000**, *112*, 8229.

(9) Ogasawara, H.; Kawai, M. *Surf. Sci.* **2002**, *502-503*, 285.

(10) Monca, C.; Allouche, A. *J. Chem. Phys.* **2001**, *114*, 4226.

(11) Picaud, S.; Toubin, C.; Girardet, C. *Surf. Sci.* **2000**, *103*, 178.

(12) Bussolin, G.; Casassa, S.; Pisani, C.; Ugliengo, P. *J. Chem. Phys.* **1998**, *108*, 9516.

(13) Honrath, R. E.; Peterson, M. C.; Guo, S.; Dibb, J. E.; Shepson, P. B., Campbell, B. *Geophys. Res. Lett.*, **1999**, *26*, 695.

(14) Honrath, R. E.; Guo, S.; Peterson, M. C.; Diiobak, M. P.; Dibb, J. E.; Arsenault, M. A. *J. Geophys. Res.* **2000**, *105*, 24183.

(15) Hudson, R. L.; Moore, M. H. *J. Geophys. Res-Planet* **2001**, *106 (E12)*, 33275

(16) Banham, S. F.; Horn, A. B.; Koch, T. G.; Sodeau, J. R. *Faraday Discuss.* **1995**, *100*, 3121.

(17) Graham, J. D.; Roberts, J. T. *J. Phys. Chem. B* **2000**, *104*, 978.

(18) Donsig, H. A.; Herridge, D.; Vickerman, J. C. *J. Phys. Chem. A* **1998**, *102*, 2302.

(19) Horn, A. B.; Chesters M. A.; McCoustra M. R. S.; Sodeau, J. R. *J. Chem. Soc. Faraday Trans.* **1992**, *88*, 1077.

(20) Yabushita, A.; Inoue, Y.; Senga, T.; Kawasaki, M.; Sato, S. *J. Phys. Chem. B* **2002**,

106, 3151.

(21) Kawasaki, M. *Appl. Surf. Sci.* **1998**, *135*, 1159.

(22) Kimmel, G. A.; Stevenson, K.P.; Dohnálek, Z.; Smith, R. S.; Kay, B. D. *J. Chem. Phys.* **2001**, *114*, 5284.

(23) Kimmel, G. A.; Dohnálek, Z.; Stevenson, K.P.; Smith, R. S.; Kay, B. D. *J. Chem. Phys.* **2001**, *114*, 5295.

(24) Stevenson, K. P.; Kimmel, G. A.; Dohnálek, Z.; Smith, R. S.; Kay, B. D. *Science* **1999**, *283*, 1505.

(25) Sato, S.; Yamaguchi, D.; Nakagawa, K.; Inoue, Y.; Yabushita, A.; Kawasaki, M. *Langmuir* **2000**, *16*, 9533.

(26) Regan, P. M.; Langford, S. R.; Ascenzi, D.; Cook, P. A.; Orr-Ewing, A. J.; Ashfold, M. N. R. *Phys. Chem. Chem. Phys.* **1999**, *1*, 3247.

(27) Zimmermann, F. M.; Ho, W. *Surf. Sci. Rep.* **1995**, *22*, 127.

(28) Giorgi, J. B.; Naumkin, F. Y.; Polanyi, J. C.; Raspopov, S. A.; Sze, N. S.-K. *J. Chem. Phys.* **2000**, *112*, 9569.

(29) Samartzis, P. C.; Bakker, B. L;. Rakitzis, T. P.; Parker, D. H.; Kitsopoulos, T. N. *J. Chem. Phys.* **1999**, *110*, 5201.

(30) Zhou, X.-L.; Zhu, X.-Y.; White, J. M. *Surf. Sci. Rep.* **1991**, *13*, 73.

(31) Leutwyler, S. *Nature* **2002**, 417, 230.

(32) Devlin, J. P.; Uras, N.; Sadlej, J.; Buch, V. *Nature* **2002**, 417, 269.

(33) Vakarin, E. V.; Badiali, J. P. *Surf. Sci.* **2002**, 513, 431.

(34) Buch, V.; Sadlej, J.; Uras, N.; Devlin, J. P. *J. Phys. Chem.* **2002**, 106, 9374.

(35) Felder, P.; Demuth, C. *Chem. Phys. Lett.* **1993**, *208*, 21.

(36) Yen, M.-W.; Johnson, P. M.; White, M. G. *J. Chem. Phys.* **1993**, *99*, 126.

(37) Polanyi, J. C.; Sze, N. S.-K.; Wang, J.-X. *J. Phys. Chem. A* **1997**, *101*, 6679.

(38) Matsumi, Y.; Tonokura, K.; Kawasaki, M.; Inoue, G.; Satyapal, S.; Bersohn, R. *J. Chem. Phys.* **1991**, *94*, 2669; **1992**, *97*, 5261.

(39) Lide, D. R.; Freerikse, H. P. R. *CRC Handbook of Chemistry and Physics, 76th edition*; CRC Press, Inc.: Boca Raton, FL, 1995.

(40) Warner, M. J.; Weiss, R. F. *Deep-Sea Res.* **1985**, *32*, 1485.

(41) Geiger, F. M.; Hicks, J. M.; de Dois, A. C. *J. Phys. Chem. A* **1998**, *102*, 1514.

(42) R. Bianco calculated the structure of $2Cl_2$ and $13H_2O$ at the MP2 level, using effective core potentials for all the heavy atoms. (private communication)

(43) Liu, Z. F.; Siu, C. K.; Tse, J. S. *Chem. Phys. Lett.* **1999**, *311*, 93.

(44) Sadtchenko, V.; Knutsen, K.; Giese, C. F.; Gentry, W. R. *J. Phys. Chem. B* **2000**, *104*, 2511.

(45) Alexander, A. J.; Kim, Z. H.; Kandel, S. A.; Zare, R. N.; Rakitzis, T. P.; Asano, Y.; Yabushita, S. *J. Chem. Phys.* **2000**, *113*, 9022.

(46) Singer, S. J.; Freed, K. F.; Band, Y. B. *Adv. Chem. Phys.* **1985**, *61*, 1.

(47) Asano, Y.; Yabushita, S. *J. Phys. Chem. A* **2001**, *105*, 9873.

(48) Bracker, A. S.; Wouters, E. R.; McCoustra M. R. S.; Suits, A. G.; Vasyutinskii, O. S. *J. Chem. Phys.* **1999**, *110*, 6749.

(49) Johnsson, K.; Engdahl, A.; Ouis, P.; Nelander, B. *J. Phys. Chem.*, **1992**, *96*, 5778.

Chapter 6

Adsorption States of NO$_2$ over Water Ice Films Formed on Au(111)

Abstract

The adsorption states of NO$_2$ over amorphous and crystalline water ice films formed on an Au(111) surface have been studied in an ultrahigh vacuum system by the TPD technique and IRAS. The ice films are prepared by deposition of gas phase water on the Au substrate at <100 K for amorphous ice and at 140 K for crystalline ice. The surface of amorphous ice is characterized by the high density of free OH, while that of crystalline ice is characterized by grain boundaries and the lack of free OH. TPD for pure ice shows only one desorption peak of H$_2$O, while after NO$_2$ adsorption on it an additional weak H$_2$O desorption peak appears at 185 K. This higher-temperature peak is attributable to decomposition of NO$_2$-H$_2$O adducts. IRAS measurements revealed that NO$_2$ adsorbs on ice surfaces as N$_2$O$_4$ with D_{2h} symmetry and that neither N$_2$O$_4$ isomers such as D-isomers nor NO$_x$ (x = 1, 2, and 3) species are produced in the temperature range of 90-140 K. Interaction of the ice surfaces with NO$_2$ (N$_2$O$_4$) as well as orientation of N$_2$O$_4$ adsorbed on the ice surfaces are investigated as a function of temperature. Thermal decomposition of NO$_2$ adsorbed on the water ice formed on an Au surface is reconfirmed, which has been reported before by Wang and Koel (*J. Phys. Chem. A* 1998, 102, 8573). A possible mechanism for the NO$_2$ decomposition is proposed.

6.1 Introduction

Heterogeneous reactions on water ice particles have attracted attention in atmospheric chemistry. Polar stratospheric clouds, which consist of nitric acid trihydrate (type I PSC) and water ice (type II PSC), have been implicated as playing a central role in the photochemical mechanism responsible for the yearly occurrence of the ozone hole.[1-3] Thus, a study of molecular adsorption on condensed water surfaces is important from an environmental chemistry point of view. We have recently studied the photodissociation dynamics of N_2O_4 adsorbed on amorphous and crystalline water ice films at 80-140 K using 193, 248, and 351 nm laser light.[4] We found that the photodissociation yield at 193 nm is much higher on amorphous ice than on crystalline ice. We assume that the large difference in the photodissociation yield between both ice film structures is due to a difference in the adsorption states of N_2O_4 on the ice films. Wang and Koel,[5,6] on the other hand, reported thermal decomposition of NO_2 coadsorbed with water ice on an Au(111) surface during TPD. This decomposition produces atomic oxygen on the Au surface, which desorbs at 510 K. They ascribed the NO_2 decomposition to the formation of D-isomers, ONO-NO_2, and nitrosonium nitrate, NO+NO3-, in the interface region between amorphous ice and the N_2O_4 layer.

A thin water ice film has been used as a model surface for type II PSC, because it can be prepared on various solid materials and facilitates sensitive spectroscopic methods to assign chemical species on the surfaces.[7-16] Especially, when a reflective metal is used as a substrate, IRAS and TPD techniques are utilized for characterization of water ice surfaces as well as for analysis of adsorbates on the surface.[15-19] Since IRAS has the surface selection rule, details of which are described in the Appendix, orientation of adsorbates can be determined.[20,21] In the present study, we have investigated interactions of NO_2 with amorphous and crystalline water ice films formed on an Au(111) surface, examining the adsorption states of NO_2 and precursor states for the NO_2 decomposition.

6.2 Experimental

All the experiments were carried out in an ultrahigh vacuum system (base pressure, 2 × 10^{-10} torr), details of which were described previously.[22,23] An Au(111) single crystal (10 mm in diameter) used as a substrate was cleaned by repeating cycles of Ar-ion sputtering and annealing at 800 K, followed by oxidation with O_3. Thermal desorption spectra (TDS) of adsorbates were obtained with a quadrupole mass spectrometer (ANELVA AQA-200), which was located at ~35° with respect to the substrate surface normal. For IRAS measurements, the IR beam from FTIR (BIO-RAD FTS-155) was focused by a BaF_2 lens onto the sample in the chamber through a BaF_2 window, the cutoff wavelength of which is ~900 cm^{-1}. The incident angle of the IR beam was ~85°. A wire grid polarizer was used to select p-polarized light, since only p-polarized light is effective for IRAS.[20,21] The paths of the IR beam were purged with dry air to reduce the effects of moisture. IRA spectra were recorded with 4 cm^{-1} resolution and 200 scans.

Water used was ultrapure Millipore water and outgassed by repeating a freeze-pumping-thaw cycle. The reservoir of water was immersed in a water ice mixture bath during experiments to keep its vapor pressure constant. NO_2 was stored in a glass reservoir in the presence of an excess of O_2 to prevent its decomposition to NO and O_2 during storage. The gas mixture was frozen at 77 K, and O_2 was pumped away before use. Since NO_2 was decomposed to some extent in the gas handling system, the inner wall of the stainless steel tube was passivated by exposing a relatively high pressure of NO_2 or O_3 for a prolonged time. Gases were introduced into the chamber through a nozzle, the end of which was ~1 cm away from the substrate. A pulsed valve (General Valve) was used to control exposures of gases. The NO_2 exposure necessary for a monolayer coverage (1 ML) of chemisorbed NO_2 on an Au(111) surface was determined previously at 160 K,[23] and the same exposure-coverage relation was applied for ice surfaces. Therefore, a real coverage for an amorphous ice surface could be different from the coverage indicated, since a roughness factor of the amorphous ice surface would be greater than unity.

6.3 Results and Discussion

6.3.1 Characterization of water ice films on Au(111).

The desorption temperature of H_2O from an Au(111) surface is raised from 150 to 160 K as H_2O coverages increases. This result is in agreement with a previous result for H_2O/Au(111).[24] IRA spectra of H_2O adsorbed on an Au(111) surface at 93 K are shown in Figure 6.1. The IRAS bands of a thin ice film have been assigned previously.[16,18] The sharp band at 3700 cm^{-1} is assigned to the stretching of free or dangling OH at the ice surface, the broad and strong band at 3389 cm^{-1} to OH stretching in bulk ice, and the weak band at 1654 cm^{-1} to HOH bending in bulk ice. The spectrum closely resembles the IR transmission spectrum of a water film at room temperature except for the 3700 cm^{-1} band,[25] indicating that the ice film on Au(111) is an amorphous ice layer.

When an ice film was formed at <100 K then heated, a significant change in the IRAS spectrum was observed, as shown in Figure 6.2. The bulk OH stretching band shifts to lower frequencies by >100 cm^{-1} at 140 K, while the bands of the free OH stretch and the HOH bend decrease in intensity. The spectrum at 140 K is basically identical to that of crystalline ice.[7] Since these spectral changes start at 120 K, the phase change of amorphous ice to crystalline ice occurs at >120 K. Thus, an amorphous ice film was prepared by deposition of gas-phase water on Au(111) at <100 K. A crystalline ice film was prepared by H_2O deposition at 140 K, followed by annealing at the same temperature for 10 min. Complete crystallization of the ice film deposited at 130 K needed >25 min of annealing at the same temperature. When the ice film was deposited at 130 K and annealed at the same temperature for 10 min, we refer to this film as semicrystalline ice film.

The degree of ice crystallinity was found to depend upon ice coverage. With decreasing amorphous ice coverage, growth of the bulk OH band of crystalline ice upon 130 K annealing becomes indiscernible as shown in Figure 6.3. This result implies that the thinner ice film on an Au(111) surface is hardly crystallized, in agreement with a recent STM study on H_2O/Au(111),[26] which show water first adsorbs as a planar,

amorphous, monolayer-high film.

Since TDS from $H_2O/Au(111)$ show no transient features with increasing H_2O coverage from monolayer to multilayer,[24] it is difficult to determine the monolayer coverage of the ice film from the TPD results alone. In the present study, we define the monolayer coverage of $H_2O/Au(111)$ as a maximum coverage at which ice crystallization does not occur at 130 K. We estimated the H_2O exposure necessary for 1 ML to be ~3 L (1 L = 1 × 10^{-6} Torr s).

6.3.2 Adsorption states of NO_2 on water ice films. Figure 6.4 shows TDS of NO^+, NO_2^+ and H_2O^+ from NO_2 adsorbed on amorphous ice. The spectra for NO_2^+ and NO^+ are very similar to those from $NO_2/Au(111)$.[6,23,27] The peak centered at 134 K is attributed to physisorbed N_2O_4, and the peak centered at 214 K to NO_2 chemisorbed on the Au surface (chemisorbed NO_2). Since chemisorbed NO_2 is not observed by IRAS at the initial stage of TPD, as will be described later, the presence of the chemisorbed NO2 peak indicates that part of the N_2O_4 adsorbed on the ice surface is held in the bulk of ice and then moves onto the Au surface upon heating. TDS for H_2O exhibit two desorption peaks in this case. The lower temperature peak (α peak) is identical to that from $H_2O/Au(111)$, and the higher temperature peak (β peak) is due to interaction of ice with NO_2, that is, adduct formation. The β peak is thus related to the formation of chemisorbed NO_2 on an Au surface. TDS from NO_2 adsorbed on crystalline ice showed very similar features to what was observed for amorphous ice. The fact that the β peak was observed for both amorphous and crystalline ice suggests that interaction of free OH with NO_2 is not related with formation of the NO_2-H_2O adduct.

Parts a and b of Figure 6.5 show IRA spectra of NO_2 adsorbed on crystalline and semicrystalline ice, respectively, as a function of NO_2 exposure. The assignments of IRAS bands for NO_2 adsorbed on a water ice film were reported by Rieley et al.:[18] the bands at ~1300 cm^{-1} and the bands at ~1750 cm^{-1} are attributed to the ONO symmetric stretching and the ONO asymmetric stretching of N_2O_4 with D_{2h} symmetry, respectively. Similarly to their results, the complete absence of the strong asymmetric stretching band of NO_2 at 1600-1650 cm^{-1} in Figure 6.5 indicates the absence of NO_2 monomer as well

as D-isomers, O=N-O-NO$_2$. When N$_2$O$_4$ coverage exceeds 4 ML, the band at 1180 cm^{-1} becomes discernible for crystalline ice, as shown in Figure 6.5a. This band is attributable to the ONO symmetric stretching of NO$_2$ adsorbed directly on the Au surface (chemisorbed NO$_2$). The formation of chemisorbed NO$_2$ implies that NO$_2$ or N$_2$O$_4$ can reach the Au surface through grain boundaries of crystalline ice. The result that the 1180 cm-1 band can be seen when N$_2$O$_4$ coverage exceeds 5 ML would be due to the time required for N$_2$O$_4$ to pass through the ice film, since the IRAS spectrum was recorded as N$_2$O$_4$ coverage was increased stepwisely. The ice coverage through which NO$_2$ can reach the Au surface was estimated to be <10 ML for crystalline ice. IRA spectra of N$_2$O$_4$ on semicrystalline ice are basically identical with those for crystalline ice, but both the ONO symmetric and the ONO asymmetric stretching bands become broader than those for crystalline ice. This band broadening may be ascribed to the appearance of new adsorption states caused by interaction of N$_2$O$_4$ with a semicrystalline ice surface. Semicrystalline ice also has grain boundaries, depth of which is ~4 ML thickness.

IRAS is selectively sensitive to the vibrational modes perpendicular to a surface (surface selection rule, details of which are described in the Appendix.),[20, 21] and therefore, we can obtain information about molecular orientation with respect to a metal surface. Figure 6.6 illustrates three orientations of N$_2$O$_4$ adsorbed on a surface. For orientation a, the ONO symmetric stretching parallel to the N-N bond axis is IRAS active but not the ONO asymmetric stretching. On the contrary, for orientation b, the asymmetric stretching perpendicular to the surface is IRAS active but not the symmetric stretching. For orientation c, both the vibrational modes are IRAS inactive. If the orientation of N$_2$O$_4$ adsorbed on a flat ice surface over a metal is determined, then information about three-dimentional configurations of a rough ice surface may be obtained from the IRA spectrum of adsorbed N$_2$O$_4$.

In Figure 6.5a and b, the bands at ~1266 cm^{-1} was ascribed by Rieley et al.[18] to the ONO symmetric stretching of the first-layer N$_2$O$_4$ on the ice surface and has an intensity comparable to that of the ONO asymmetric stretching bands. Since an IR transmission

spectrum of gas phase N_2O_4 exhibits both the symmetric and asymmetric ONO stretching bands in comparable intensities, the first-layer N_2O_4 should be randomly oriented. For crystalline ice of Figure 6.5a, the first-layer N_2O_4 bands in the symmetric and asymmetric ONO stretching regions grow slowly with increasing NO_2 exposure, and the growth stops virtually at ~5 ML. At the same time, the sharp band at 1297 cm^{-1} grows rapidly and becomes dominant at >5 ML. These results indicate that the formation of a disordered N_2O_4 layer is actually limited in the first 5 ML and that ordered N_2O_4 in orientation a of Figure 6.6 dominates in multilayers over 5 ML, provided that the surface of crystalline ice is flat and parallel to the Au surface. Since a randomly oriented N_2O_4 layer is less than 5 ML on the NO_2-covered Au(111) surface,[23] the crystalline ice surface may not be completely flat.

N_2O_4 adsorbed on semicrystalline ice shows a more complicated IRAS spectrum than that on crystalline ice, so that we applied curve fitting to analyze the spectra in Figure 6.5b on the assumption that the IRAS absorbance band shape is Lorenzian. The results show that the ONO symmetric stretching region consists of four bands typically at 1303, 1298, 1280, and 1266 cm^{-1}. The sharp bands at 1303 and 1298 cm^{-1} show a similar dependence on N_2O_4 coverage. Since the 1303 cm^{-1} band exhibits a much sharper bandwidth than the 1298 cm^{-1} band, the species giving the 1303 cm^{-1} band would be relatively free. We tentatively assign the 1298 cm^{-1} band to N_2O_4 in a multilayer N_2O_4 lattice and the 1303 cm^{-1} band to N_2O_4 just outside the lattice or in a loose lattice, both of which are in orientation a. The N_2O_4 species giving the 1280 cm^{-1} band is not observed for crystalline ice and, therefore, would interact strongly with the ice surface, but further details of this species are not understood well at present. The curve fitting analysis for adsorbed N_2O_4 is still under progress, and its details will be reported elsewhere.

When NO_2 was adsorbed on amorphous ice, its IRA spectra were basically similar to those for semicrystalline ice, as shown in Figure 6.7b. The frequencies, intensities, and assignments of N_2O_4 adsorbed on the ice surfaces are summarized in Table 6.1. The chemisorbed NO_2 band was not observed even for 1 ML amorphous ice coverage,

indicating that amorphous ice is continuous and has no grain boundaries. Although various kinds of NO_2 species are formed in a low temperature inert gas matrix[28] and on solid substrates,[29-33] NO_2 adsorption on amorphous and crystalline ice results in formation of a pure N_2O_4 layer. Also, D-isomers, nitrosonium nitrate, and HONO were not detected on any ice films used. It should be noted that failure in detecting D-isomers and nitrosonium nitrate is not due to insufficient sensitivity of IRAS, since these species have been detected by IRAS previously.[29-33]

After NO_2 adsorption on semicrystalline and amorphous ice at ~90 K, the substrate temperature was elevated to examine a change in the adsorption states of N_2O_4. Figure 6.8 shows a significant difference in temperature dependence between amorphous and semicrystalline ice. For N_2O_4 adsorbed on semicrystalline ice, the 1303 cm^{-1} band rapidly increases in intensity with increasing temperature with a band shift to lower frequencies, while the bands in the ONO asymmetric stretching region decrease. Curve fitting analysis revealed that the 1303 cm^{-1} band merges into the 1298 cm^{-1} band at 110 K, forming a sharp band at 1296 cm^{-1}. We assume that relatively free N_2O_4 in orientation a is involved in a well-ordered N_2O_4 lattice at > 110K. The 1280-cm^{-1} band grows with elevating temperature up to 120 K, while the 1266 cm^{-1} band remains virtually unchanged. The growth of the 1280 cm-1 band seems to be related to the decrease of the asymmetric stretching bands. Therefore, randomly oriented N_2O_4 may convert to some extent into ordered N_2O_4, giving the 1280 cm^{-1} band. For the amorphous ice case shown in Figure 6.7b, both the symmetric and asymmetric stretching bands increase in intensity at higher temperatures. It was shown by curve fitting that the 1302 cm^{-1} band also merges into the 1298 cm^{-1} band at 120 K, and the latter shifts significantly to lower frequencies at > 100 K. The 1280 cm^{-1} band decreases to some extent at 120 K, but the 1266 cm^{-1} band grows significantly at 120 K. These results are explained as follows: the multilayer N_2O_4 is crystallized and undergoes strong interaction with interlayer N_2O_4 at > 100 K, and the species giving the 1280 cm-1 band partly converts into disordered N_2O_4 at 120 K. In addition, the increase in the total area of the symmetric stretching as well as the asymmetric stretching bands upon

heating indicates that IRAS inactive species become IRAS active species at higher temperatures. As described below, amorphous ice has much higher densities of free OH and loosely bound H_2O molecules than crystalline ice. The surface of amorphous ice is known to interact strongly with compounds having hydrogen bond donors.[36] Such a reactivity of amorphous ice may produce various adsorption states of N_2O_4 on its surface. We also examined carefully if D-isomers and/or $NO^+NO_3^-$ are formed on amorphous ice at elevated temperatures, since Givan and Lowenschuss[33] reported that $NO^+NO_3^-$ is produced by temperature cycling from disordered N_2O_4 layers, in which D-isomers are involved. Our IRAS measurements could not detect any evidence for $NO^+NO_3^-$ as well as D-isomers.

The interaction of free OH on amorphous ice with adsorbed NO_2 can be examined by IRAS. Figure 6.8 shows the difference spectra of IRAS before and after N_2O_4 adsorption on amorphous ice at 100 K, followed by annealing at the indicated temperatures. Positive bands represent band intensity reduction compared to a bare ice surface. The free OH band at 3700 cm^{-1} decreases in intensity upon NO_2 adsorption at 100 K. This intensity decrease is equal to the band intensity of free OH before NO_2 adsorption, indicating that all free OH interact with adsorbed N_2O_4 and, hence, they are present on the surface. In addition, the wide positive band centered at 3480 cm^{-1} indicates that bulk OH also interacts with adsorbed N_2O_4. Since the center frequency of this bulk OH band is ~100 cm^{-1} higher than the peak frequency of the amorphous bulk-ice OH band, H_2O interacting with N_2O_4 would be surface H_2O molecules that are weakly bound to the bulk ice. When the sample is heated at 115-120 K, the 3700 and 3480 cm^{-1} bands remain almost unchanged, indicating that the interaction of $N2O4$ with the ice surface is not changed at these temperatures. The change at 3230-3300 cm^{-1} is observed when amorphous ice is crystallized.

Returning to Figure 6.7, all the bands attributed to adsorbed N_2O_4 disappear when the sample is annealed at 140 K. However, this result does not imply the complete desorption of all NO_x species from the ice surface, since TDS after annealing at 140 K shows the desorption peak of chemisorbed NO_2 at ~210 K (Figure 6.4). When NO_2 was

dosed on the ice film at 130-140 K, no bands assignable to NO_x species were observed, but chemisorbed NO_2 was also observed in TDS. In coincidence with the TPD results, the IRAS band of chemisorbed NO_2 appears at 190 K and disappears at 230 K, as shown in Figure 6.7a. Part of the N_2O_4 adsorbed on the ice surfaces at <130 K, therefore, undergoes a conformational change at 140 K to form IRAS inactive configurations such as orientation c. Formation of this IRAS inactive species would result from formation of the H_2O-NO_2 adduct, which is decomposed at ~185 K to produce gas phase H_2O (the β peak in TDS) and chemisorbed NO_2.

6.3.3 Thermal decomposition of NO_2 in the presence of water ice. Wang et al[5,6]
reported that when NO_2 co-adsorbed with H_2O on an Au(111) surface at <100 K, atomic oxygen was formed on the Au surface that functions as trapping sites. The atomic oxygen desorbed as molecular O_2 at ~520 K in TPD. They concluded that this NO_2 decomposition is not due to the catalytic effects of an Au surface but attributable to the formation of D-isomers and their conversion to $NO^+NO_3^-$ on the ice surface. We also found that O_2 desorption occurs during TPD for NO_2 adsorbed on an ice film formed on Au(111). We have already reported that NO_2 chemisorbed on an Au(111) surface is partly decomposed at 180-240 K during TPD to produce NO and atomic oxygen on the surface.[23] The measured ratios of NO over NO_2 were 26 % at 4.0 K·s^{-1} of TPD temperature ramp and 52 % at 1.0 K·s^{-1}.[22] This difference in NO ratio is due to that the decomposition of chemisorbed NO_2 competes with its desorption. Although NO was thus produced during TPD, O_2 desorption was hardly observed at <600 K. However, after the adsorption-desorption cycle of chemisorbed NO_2 was repeated a few times at <400 K, O_2 desorption did occur at 507 K in TPD.[23] These results show that an Au(111) surface is intrinsically active for NO_2 decomposition to produce NO and atomic oxygen at temperatures as low as 200 K. Therefore, it is reasonably assumed that coadsorbed water enhances the adsorption and decomposition of chemisorbed NO_2 through H_2O-NO_2 adduct formation. Figure 6.8a shows that the 1171 cm^{-1} band appears at 190 K and disappears at 230 K. This band is assigned to chemisorbed NO_2 formed by the decomposition of the H_2O-NO_2 adduct. The band is broad and shifted to lower

frequencies compared to the sharp 1182 cm^{-1} band of chemisorbed NO_2 that is directly formed from gas-phase NO_2. Both the broadening and the red shift of the band indicate strong interaction of chemisorbed NO_2 with the Au surface, which may lead to the NO_2 decomposition. Furthermore, TDS from $N_2O_4/H_2O/Au(111)$ (Figure 6.4) shows that the β peak overlaps with the desorption peaks of NO_2 and NO. This implies that NO_2 formed by the decomposition of the H_2O-NO_2 adduct is dosed to the surface where the NO_2 decomposition is occurring. The overlapping of the β peak with the NO_2 desorption peak is essential for the decomposition of NO_2 on an Au surface, because NO_2 must be supplied to a catalytically active Au surface for its decomposition. Thus, coadsorbed water plays a role to make the NO_2 desorption temperature higher than the temperature for NO_2 decomposition on an Au surface by forming the H_2O-NO_2 adduct.

6.4 Appendix

6.4.1 Principle of IRAS.
It is known that the IRA spectrum of an adsorbate covered substrate depends on the optical constants of the adsorbate and substrate and the angle of incidence and state of polarization of the incident infrared beam.[37] The specific details of the dependence can be obtained by applying the boundary conditions governing the passage of electromagnetic radiation from on continuous medium to another to obtain the reflection equations for a three phase system.

In order for light of wavenumber, ν, to be absorbed by a molecule, three conditions must be met;

1) the molecule must have a nonzero dipole transition moment at ν,

2) the magnitude of the electric vector of the light must be nonzero in the region of the molecule,

3) the molecule must have a nonzero component of its dipole transition moment along the direction of the electric vector of the light (This condition does not imply that the molecule is necessarily oriented along the electric field; it just requires the change in dipole moment during a particular vibrational mode to have a component along the

field).

When light is reflected from a surface the electric vector of the incident light suffers a phase change on reflection which depends on the angle of incidence and the state of polarization of the incidence light. The phase change for reflection from a typical metal as a function angle of incidence, θ_i, is shown in Figure 6.9 for the components of the incident light oriented parallel and perpendicular to the plane of reflection (the plane of reflection is the plane formed by the incident and reflected light beam). The phase shift for the perpendicular component, δ_s, is not a strong function of θ_i, remaining near 180°for all angle of incidence. The phase shift for the parallel component, δ_p, is a strong function of θ_i, however, varying from near 0° at small θ_i to 180°at grazing incidence.

Since the phase change on reflection for the perpendicular component is near 180° for all angles of incidence, the incident and reflected electric vectors very nearly cancel each other resulting in only a very small net electric field parallel to the metal. Thus one would expect very little absorption of this component of the incident light by an adlayer. At small angles of incidence (near normal incidence) the phase change for the parallel component, δ_p, is near 0° and again the two electric vectors very nearly cancel. However at larger angles of incidence, where δ_p is near 90°, the vector addition of the two electric vectors results in an electric field with a substantial component perpendicular to the metal. Note that at grazing incidence, 90°, the phase change, δ_p, is 180° and the incident and reflected electric vectors again cancel. The conclusion reached from this qualitative analysis is that only the parallel component of the incident infrared radiation at a near grazing incidence angle can be appreciably absorbed by the adlayer and that the absorbance will be largest at a high angle of incidence but not at grazing incidence.
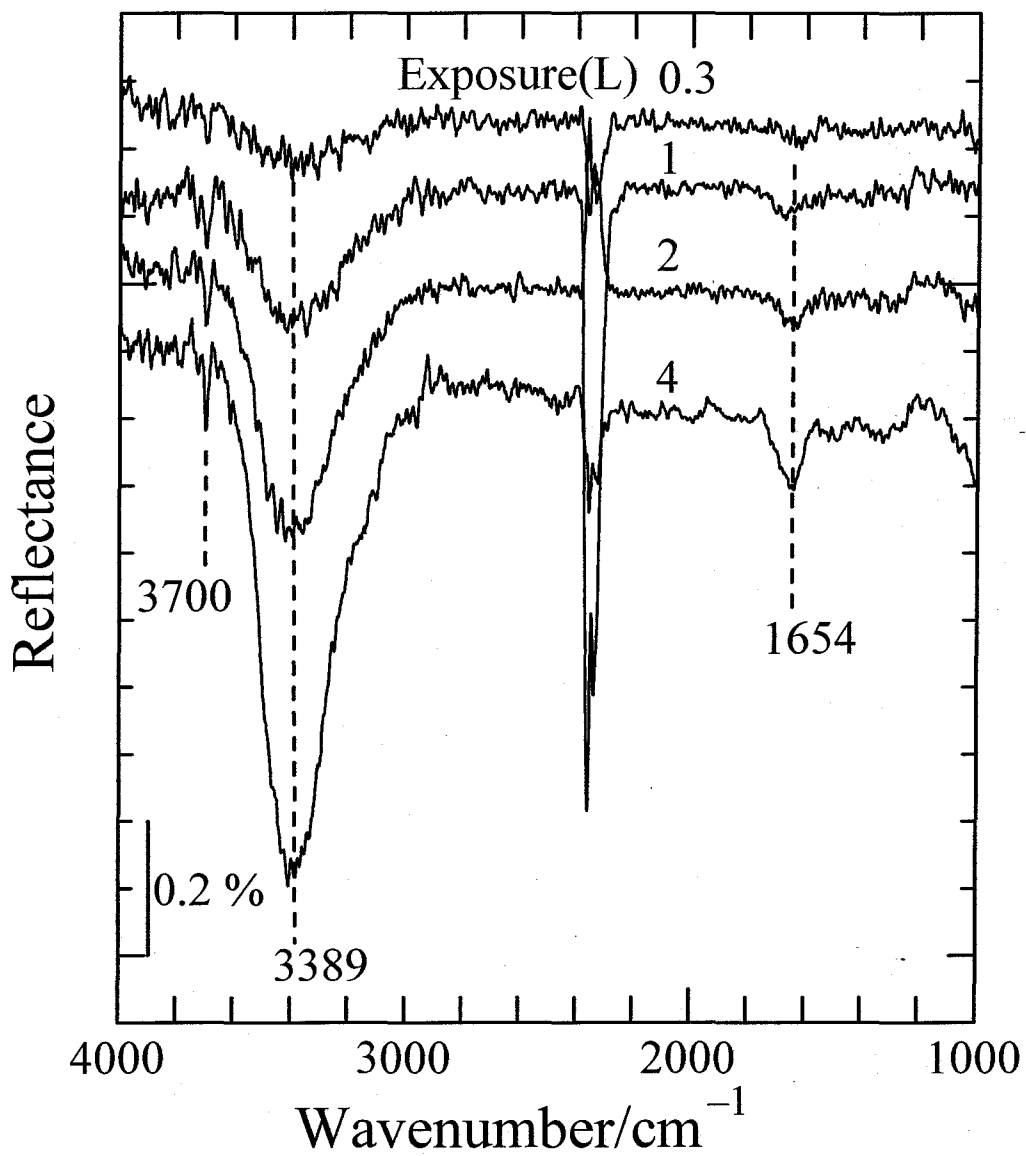
Figure 6.1 IR reflection absorption (IRA) spectra of H_2O adsorbed on an Au(111) surface at 93 K as a function of exposure.
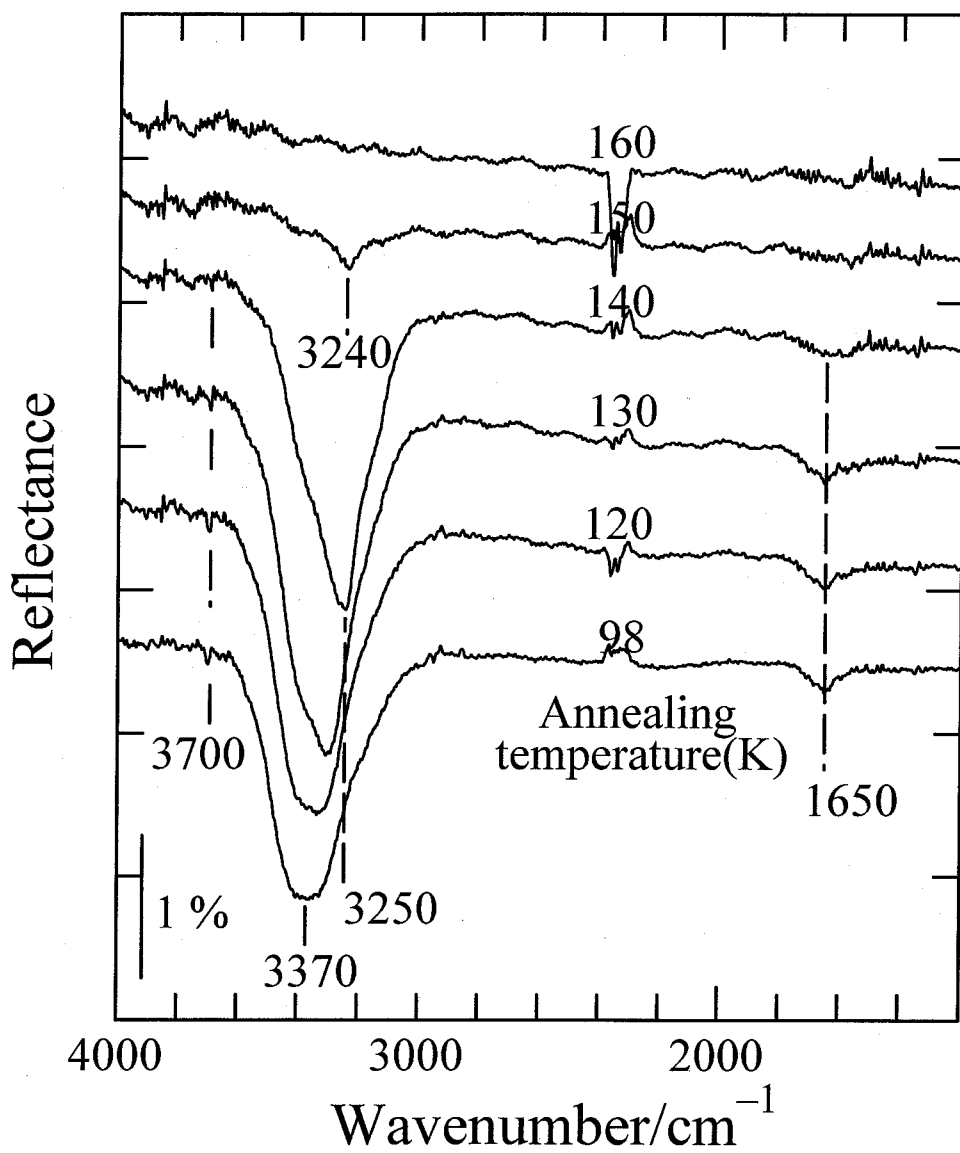
Figure 6.2 Temperature dependence of the IRA spectrum of H_2O adsorbed on an Au(111) surface. H_2O was first adsorbed at 98 K, and then the substrate was heated stepwisely to the indicated temperatures.
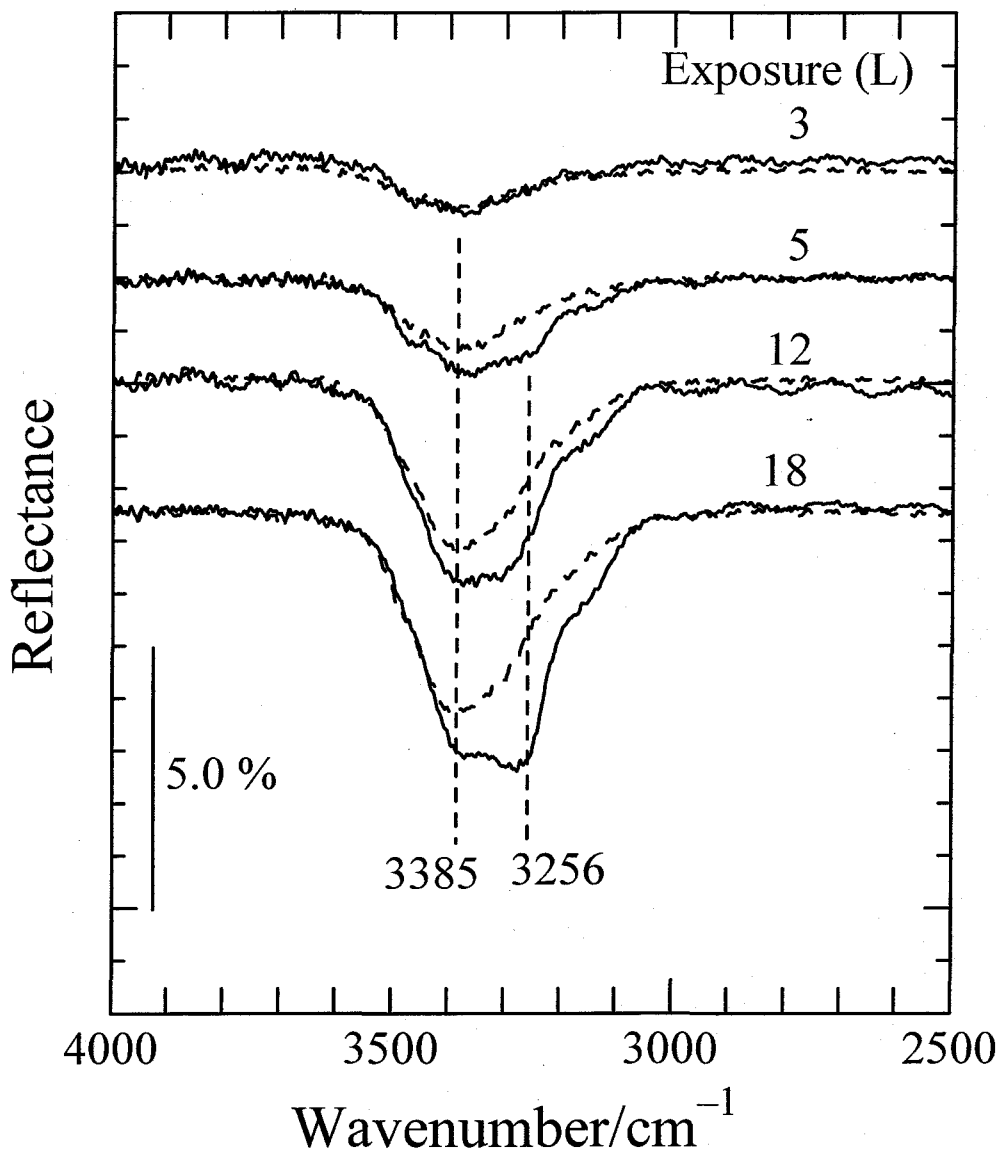
Figure 6.3 Coverage dependence of the crystallization of amorphous ice adsorbed on an Au(111) surface. H_2O was first adsorbed at 90 K (dotted line), followed by annealing at 130 K for 10 min (solid line).
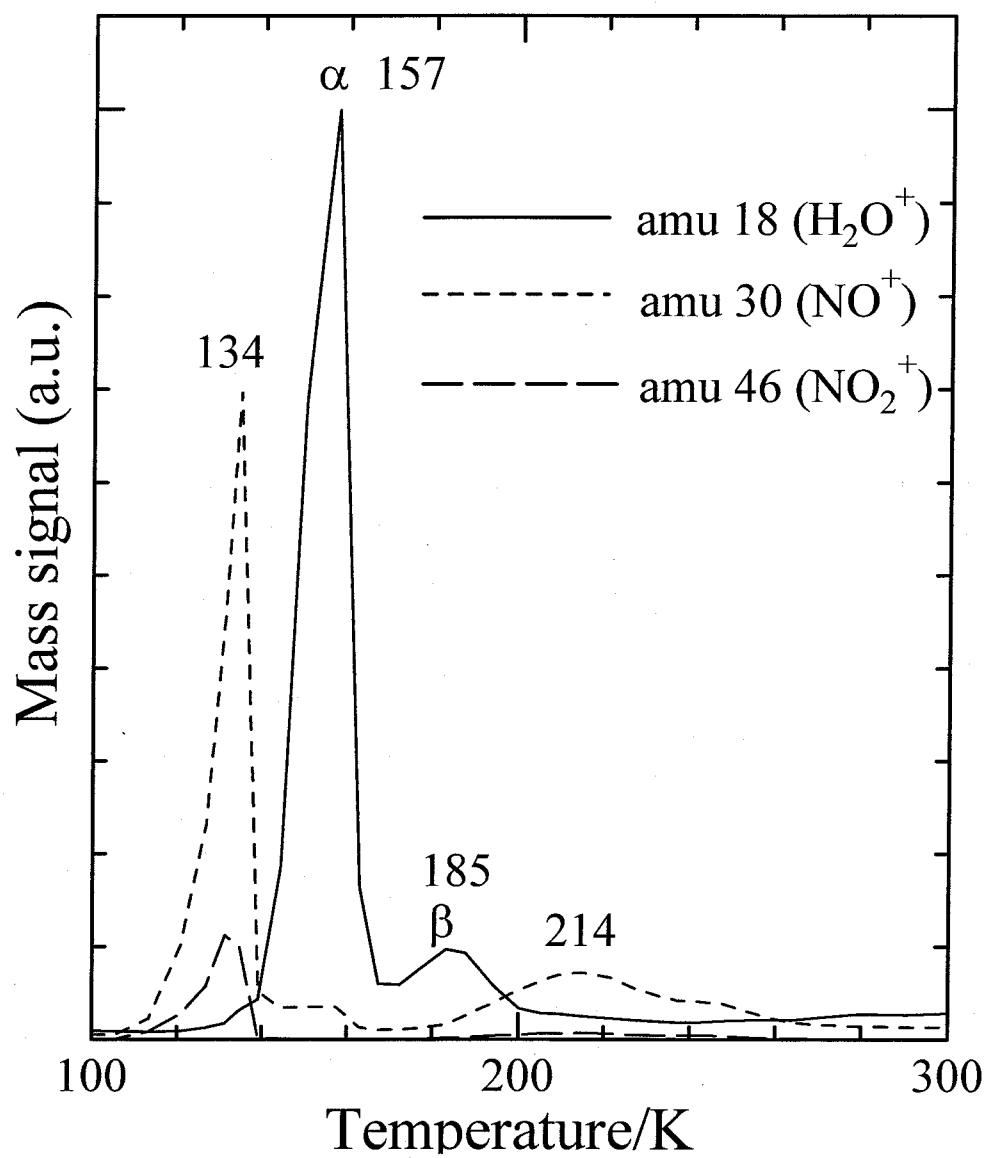
Figure 6.4 TDS from NO$_2$ adsorbed on amorphous ice. The temperature ramp was 4 K·s^{-1}.
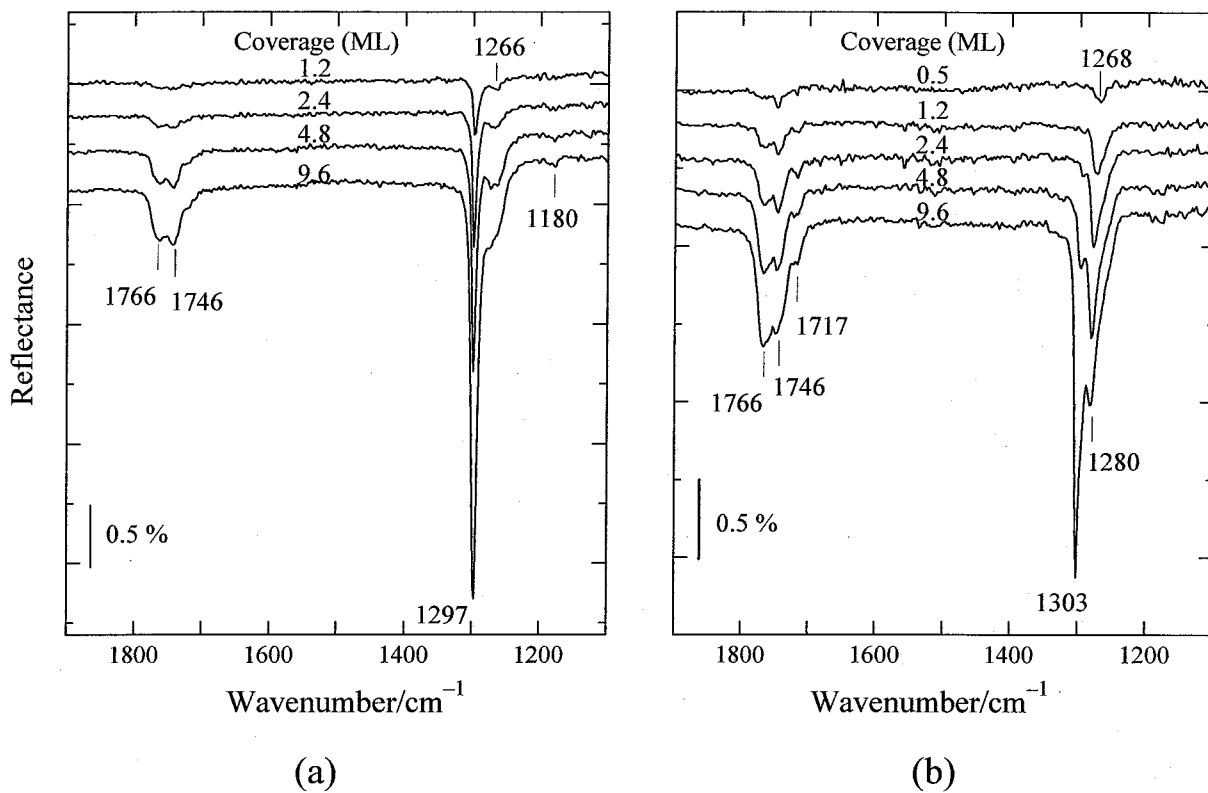
Figure 6.5 IRA spectra of N_2O_4 adsorbed at 91 K as a function of N_2O_4 coverage on (a) 8-ML crystalline ice and (b) 5-ML semicrystalline ice.
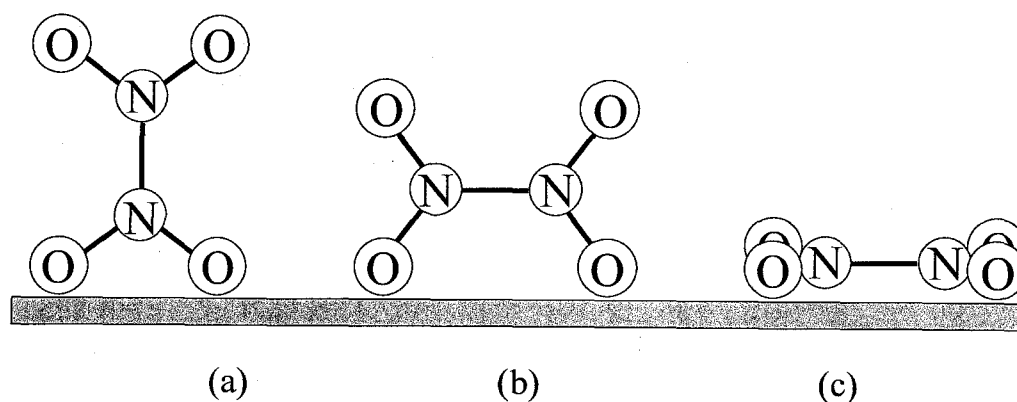
Figure 6.6 Orientations of N_2O_4 adsorbed on a surface.

Table 6.1: Vibrational Frequencies and Tentative Assignments of N_2O_4 (D_{2h}) Adsorbed on Water-Ice Surfaces at $\sim$2.4 ML

band (cm^{-1})	intensities[a]			tentative assignments[b]
	crystalline ice	semicrystalline ice	amorphous ice	
ν_{ssym} Region				
1256	none	none	W	D
1266−1271	W	W	W	B
1278−1285	none	M	S	C
1290−1303	S	W	S	A
ν_{assym} Region				
1712−1716	none	W	M	C
1735	none	none	M	D
1745−1746	W	M	S	B
1761−1772	W	M	S	B

[a] S, strong; M, medium; W, weak; VW, very weak. [b] A, N_2O_4 in a lattice or a loose lattice; B, randomly oriented N_2O_4; C, N_2O_4 interacted with the ice surface; D, N_2O_4 interacted strongly with the amorphous ice surface.
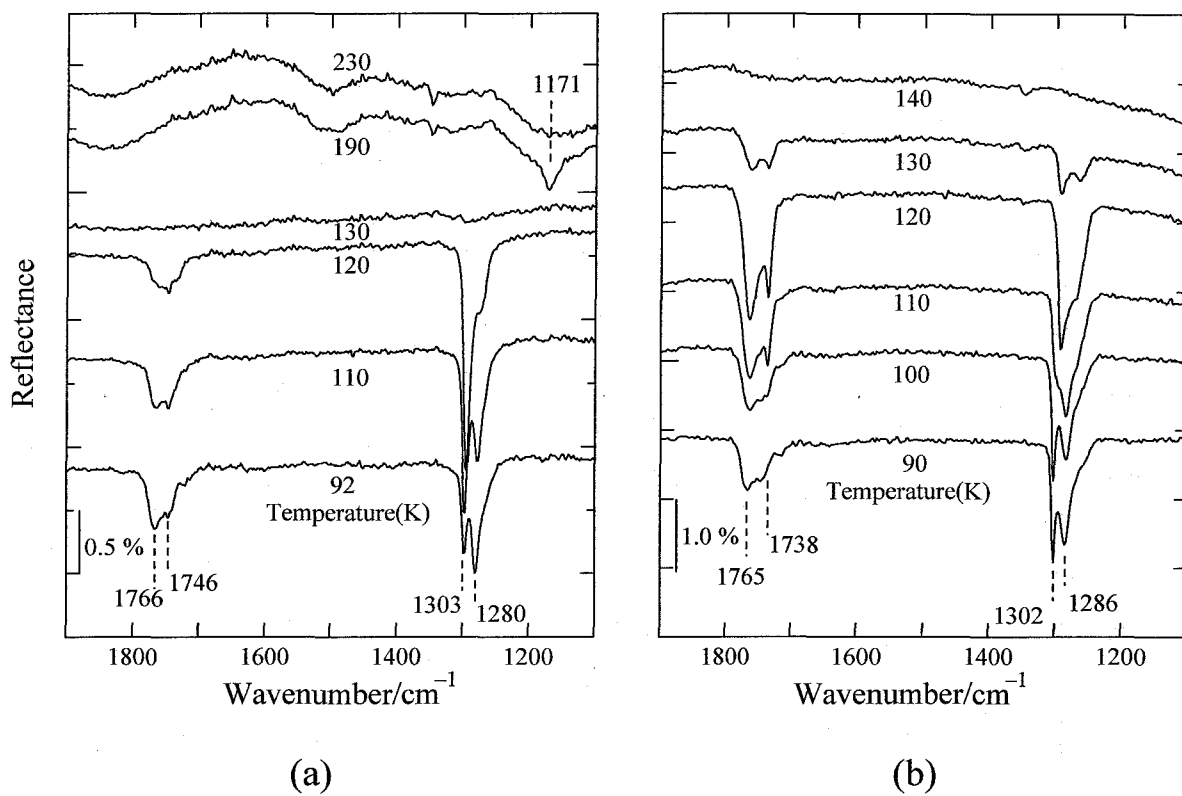
Figure 6.7 Temperature dependence of the IRA spectrum of N_2O_4 adsorbed on (a) 5 ML semicrystalline ice and (b) 3 ML amorphous ice. The substrate temperature was elevated stepwisely to the indicated temperatures.
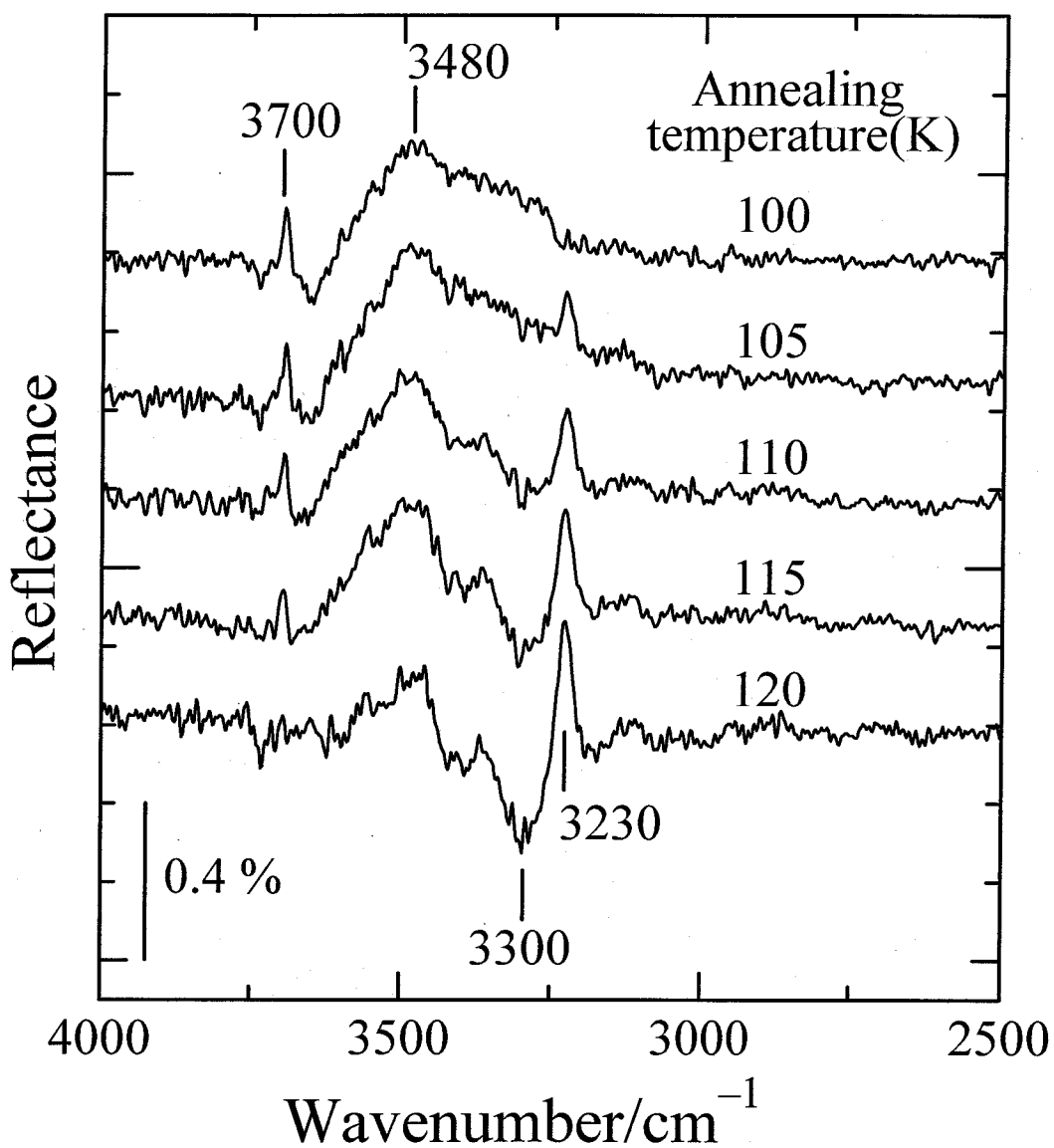
Figure 6.8 Difference spectra in the OH stretching region upon NO_2 adsorption on amorphous ice, followed by annealing at the indicated temperatures. The spectra are referred to that taken for pure ice deposited at 100 K. The coverages of H_2O and N_2O_4 were 5 and 1.5 ML, respectively.
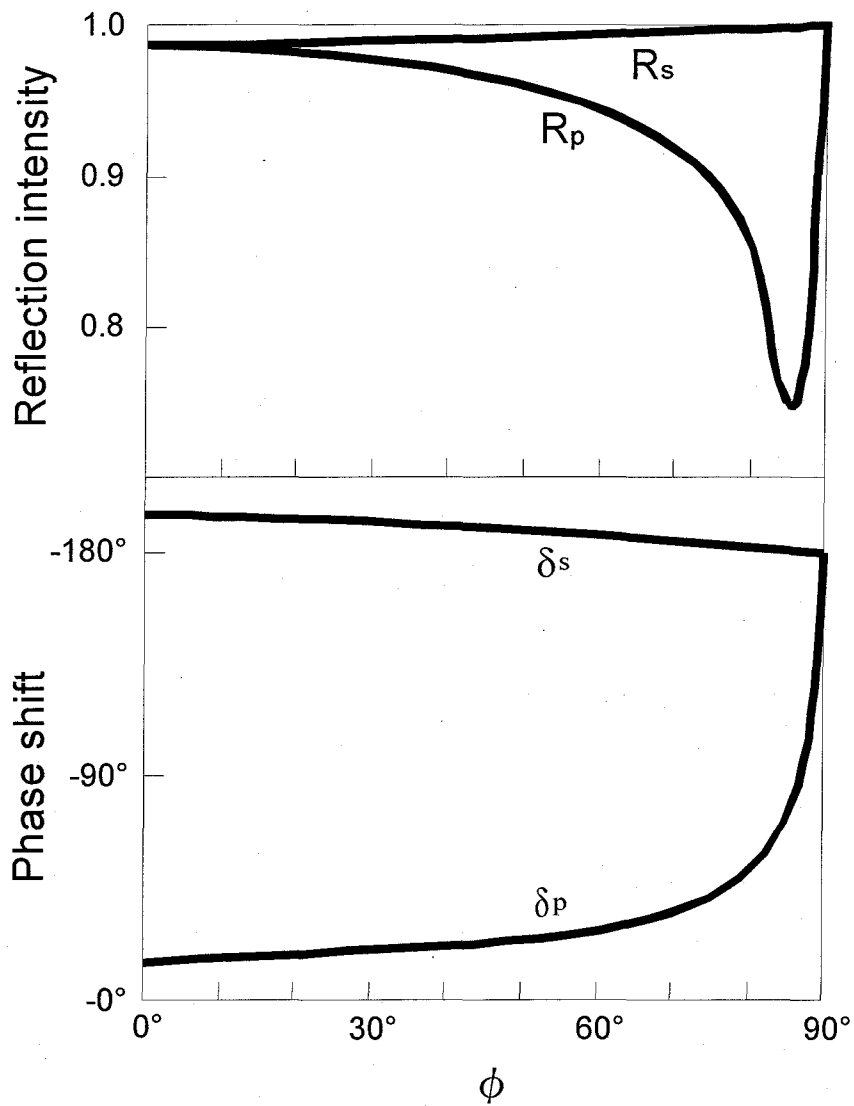
Figure 6.9 The reflectivity (upper panel) and the phase change (lower panel) on reflection from a typical metal for the parallel, R_P and δ_p, and perpendicular, R_S and δ_S, components of the incident light as a function of angle of incidence. From ref. 38.

References

(1) Solomon, S.; Garcia, R. R.; Rowland, F. S.; Wuebbles, D. J. *Nature* **1986**, *321*, 755.

(2) Toon, O. B.; Turco, R. P. *Scient. Amer.* **1991**, *264*, 68.

(3) Toon, O. B.; Tolbert, M. A. *Nature* **1995**, *375*, 218.

(4) Yabushita, A.; Inoue, Y.; Senga, T.; Kawasaki, M.; Sato, S. *J. Phys. Chem. B* submitted.

(5) Wang, J.; Voss, M. R.; Busse, H.; Koel, B. E. *J. Phys. Chem. B* **1998**, *102*, 4693.

(6) Wang, J.; Koel, B. E. *J. Phys. Chem. A* **1998**, *102*, 8573.

(7) Tolbert,M. A.; Middlebrook, A. M. *J. Geophys. Res.* **1990**, *95*, 22423.

(8) Middlebrook, A. M.; Tolbert, M. A. *Geophys. Res. Lett.* **1996**, *23*, 2145.

(9) Koehler, B. G.; Middlebrook, A. M.; Tolbert, M. A. *J. Geophys. Res.* **1992**, *97*, 8065.

(10) Kehler, B. G.; McNeil, L. S.; Middlebrook, A. M.; Tolbert, M. A. *J. Geophys. Res.* **1993**, *98*, 10563.

(11) Middlebrook, A. M.; Iraci, L. T.; McNeil, L. S.; Koehler, B. G.; Wilson, M. A.; Saastad, O. W.; Tolbert, M. A. *J. Geophys. Res.* **1993**, *98*, 20473.

(12) Middlebrook, A. M.; Berland, B. S.; Georg, S. M.; Tolbert, M. A. *J. Geophys. Res.* **1994**, *99*, 25655.

(13) Graham, J. D.; Roberts, J. T. *Geophys. Res. Lett.* **1995**, *22*, 251.

(14) Graham, J. D.; Robert, J. T. *J. Phys. Chem.* **1994**, *98*, 5974.

(15) Horn, A. B.; Banham, S. F.; McCoustra, M. R. S. *J. Chem. Soc., Faraday Trans.* **1995**, *91*, 4005.

(16) Horn, A. B.; Koch, T.; Chester, M. A.; McCoustra, M. R. S.; Sodeau, J. R. *J. Phys. Chem.* **1994**, *98*, 946.

(17) Koch, T. G.; Banham, S. F.; Sodeau, J. R.; Horn, A. B.; McCoustra, M. R. S.; Chesters, M. A. *J. Geophys. Res.* **1997**, *102*, 1513.

(18) Rieley, H.; McMurray, D. P.; Haq, S. *J. Chem. Soc., Faraday Trans.* **1996**, *92*, 933.

(19) Rieley, H.; Colby, D. J.; McMurray, D. P.; Reeman, S. M. *J. Phys. Chem. B* **1997**, *101*, 4982.

(20) Greenler, R. G,; Rahn, R. R.; Schwartz, J. P. *J. Catal.* **1971**, *23*, 42

(21) Suetaka, W. *Surface Infrared and Raman Spectroscopy*, Prenum Press: New York and London, 1995; p13.

(22) Sato, S; Suzuki, T. *J. Phys. Chem.* **1996**, *100*, 14769.

(23) Sato, S.; Senga, T.; Kawasaki, M. *J. Phys. Chem. B* **1999**, *103*,5063.

(24) Kay, B. D.; Lykke, K. R.; Creighton, J. R.; Ward, S. J. *J. Chem. Phys.* **1989**, *91*, 5120.

(25) Ataka, A.; Yotsuyanagi, T.; Osawa, M. *J. Phys. Chem.* **1996**, *100*, 10664.

(26) Ikeyama, N.; Gewirth, A. A. *J. Am. Chem. Soc.* **1997**, *119*, 9919.

(27) Bartram, M. E.; Koel, B. E. *Surf. Sci.* **1989**, *213*, 137.

(28) Bandow, H.; Akimoto, H.; Akiyama, S.; Tezuka, T. *Chem. Phys. Lett.* **1984**, *111*, 496.

(29) Fateley, W. G.; Bent, H. A.; Crawford, Jr., B. *J. Chem. Phys.* **1939**, *31*, 204.

(30) Hisatsune, I. C.; Devlin, J. P.; Wada, Y. *J. Chem. Phys.* **1960**, *33*, 714.

(31) Varetti, E. L.; Pimentel, G. C. *J. Chem. Phys.* **1971**, *55*, 3813.

(32) Givan, A.; Loewenschuss, A. *J. Chem. Phys.* **1989**, *90*, 6135.

(33) Givan, A.; Loewenschuss, A. *J. Chem. Phys.* **1989**, *91*, 5126.

(34) Givan, A.; Loewenschuss, A. *J. Chem. Phys.* **1990**, *93*, 7592.

(35) Givan, A.; Loewenschuss, A. *J. Chem. Phys.* **1991**, *94*, 7562.

(36) Schaff, J. E.; Roberts, J. T. *J. Phys. Chem.* **1996**, *100*, 14151.

(37) Born, M; Wolf, E. *Principle of Optics*, Pergamon Press Inc., New York, 1959

(38) Hayden, B. E. *Vibrational Spectroscopy of Molecules on Surfaces*, Plenum, 267, 1987

Chapter 7

Photodissociation of N_2O_4 Adsorbed on Amorphous and Crystalline Water Ice Films

Abstract

The photodissociation dynamics of N_2O_4 adsorbed on amorphous and polycrystalline water ice films at 80-140 K was investigated at 193, 248 and 351 nm. Firstly, the adsorbed states of ice on an Au substrate and N_2O_4 on the ice films were investigated by IRA and TPD spectroscopic measurement. Secondly, TOF spectra of the photofragments were measured by probing REMPI signals of $NO(v = 0)$ and $O(^3P_2)$. On both amorphous and crystalline ice films, internally relaxed NO was observed, while internally hot NO was probed from the photodissociation of N_2O_4 adsorbed directly on an Au substrate. The TOF distributions of $NO(v = 0)$ for the ice experiment consist of fast and slow components. The slow component is much stronger than the fast one. A large difference in the apparent dissociation yields between amorphous and crystalline ice films was observed. A combination of TPD and REMPI detection of photofragments (temperature-programmed photodetachment spectroscopy) reveals the difference and similarity in adsorption states and photodissociation dynamics between N_2O_4 adsorbed on crystalline and amorphous ice films.

7.1 Introduction

Observations of photochemical reactions in or on water ice have been reported for several molecules. The 193 nm photodissociation of NH_3 co-adsorbed with water ice on a quartz substrate produces fast and slow H atoms.[1] The fast H atoms were attributed to the photodissociation of NH_3 adsorbed on the ice surface, while the slow H atoms to the atomic hydrogen scattered on a rough ice surface. Upon UV irradiation in the gas phase, OClO decomposes to O + ClO or Cl + 2 O. However, when irradiated in polycrystalline ice, it decomposed to Cl + O_2 at 300 and 235 nm, followed by migration of the Cl atom to a non-photolyzed OClO to form Cl-(OClO).[2] It has been proposed that OClO adsorbs to ice under stratospheric conditions, though in very low concentrations.[3] The photochemistry of ozone in excess ice has been previously investigated using 266 nm laser irradiation.[4] At low temperatures, H_2O_2 is formed through the hydrogen-bonded complex between ozone and the free OH bond of ice. At higher temperature, H_2O_2 is produced by the reaction of the electronically excited oxygen atom $O(^1D)$ with the nearest water molecule. These results suggest a unique character of heterogeneous chemical reactions on water ice surface.

Ball predicted the stabilization energies by interaction with water molecules to be on the order of 0-8 kJ mol^{-1} based on his quantum mechanical calculations.[5] The adsorption states of NO_2 on amorphous and crystalline ice surface were studied experimentally. On crystalline ice, N_2O_4 form a tightly packed ordered layers with the N-N axes canted at 10° to the surface normal.[6,7] Two thermal reaction paths of N_2O_4 with ice are found by using IRAS and TPD techniques.[8] One path produces gas phase HONO and HNO_3 below 150 K, independent of both the crystallinity of the ice film and the exposure of NO_2. In contrast, another reaction pathway depends strongly on these variables and was monitored by the formation of oxygen atoms on a Au(111) substrate surface. The latter reaction only occurs following multilayer adsorption of NO_2 (present as N_2O_4) and only if the adsorption is on amorphous ice clusters and not crystalline ice. Formation of NO_2-H_2O adducts was observed in TPD spectra.[7] Rieley et al. prepared ordered

monolayers of N_2O_4 by adsorption of NO_2 on an ice surface of about 30 ML held on a Cu(100) substrate at 100 K. NO_2 was observed as a product of photodissociation at 355 nm.[9,10] The translational temperature of the NO_2 photofragments is low due to rapid relaxation by the ice bath. On the contrary, when the surface is an insulator substrate or a metal substrate, internally hot $NO(v = 0-9)$ as well as NO_2 are produced from N_2O_4 at 248 and 193 nm.[11-13] Under atmospheric conditions, according to Honrath et al., NO_x levels in the interstitial air of surface snow in the polar regions are of magnitude 3 to 10 times those in the ambient air.[14] The high level NO_x comes from the solar photochemical reaction of NO_3^- in snow.[15] Dubowski et al. quantify the NO_2 fluxes released into the gas phase during the continuous $\lambda \sim 300$ nm photolysis of NO_3^- in sub-millimeter ice layers produced by freezing aqueous KNO_3 sprays on cold surfaces.[16,17]

In this study we have investigated the UV photodissociation dynamics of N_2O_4 adsorbed on amorphous and crystalline water ice films by measuring the translational and internal energy distributions of the NO photofragments with photofragment TOF spectroscopy. TPD spectroscopy and IRAS were used for the surface adsorbed species on ice. Existence of the free OH groups on an amorphous ice surface and the grain boundaries on a crystalline ice film govern the adsorption state, photodissociation quantum yield, and dissociation dynamics of N_2O_4 on the ice films.

7.2 Experimental

Two sets of experiments were performed. The TOF of the photofragments from the photodissociation of N_2O_4 on a water ice film was conducted and IRAS measurements were carried out.

7.2.1 Measurement of TOF of the photofragment NO. The examination of the dynamics of surface photodissociation of N_2O_4 on a water ice film prepared on a cooled polycrystalline Au substrate with (111) domains was performed in combination with a pulsed molecular beam, an excimer laser and a dye laser. The experimental technique

and details have been given previously.[18] NO_2 gas was prepared from the mixture of NO (300 Torr) with O_2 (610 Torr), which was deposited on a water ice film by expanding the gas with a pulsed molecular beam head (General Valve) every 100 ms, which was synchronized with dissociation laser triggers. A typical stagnation pressure of the gas valve was 100 Torr. The delay between the molecular beam and photolysis laser triggers was typically set to 50 ms. Since signal intensity did not depend on the delay for 10-90 ms, unwanted gas-phase photodissociation was completely avoided. Only the photofragments from the surface photodissociation were observed by the REMPI detection.[19]

We have tested the effect of deposition method of NO_2 on the TOF spectra by changing the direct exposure with the pulsed molecular collimated effusive beam to the indirect deposition with the backfill method. The experimental results were essentially the same. Therefore in this paper, the results with the direct deposition method are reported unless otherwise noted.

7.2.1.1 Preparation of ice layers.
Details of water ice films are described in chapter 3. The polycrystalline Au substrates with (111) domains were prepared by dc glow-discharge sputtering, in which Ar^+ bombardment with low energy leads to atomic surface flatness of the sputtered films.[20] It was cleaned by oxygen atoms produced from the 193 nm or 351 nm photodissociation of gaseous NO_2 at substrate temperature $T =$ 520 K for 60 min. After this procedure, the Au substrate was annealed at 570 K for 5 min and then cooled to $ca.$ 80 K with liquid nitrogen (LN_2). Layers of water were then condensed on the Au surface. The preparation of water ice films and their characteristics have been previously described.[18] Depending on pressure, temperature, the substrate lattice structure and the angular distribution of incident H_2O flux, water ice on a cold substrate can exist in a number of structurally different forms.[21-28] There are many known phase of ice that can be classified roughly into three types: porous amorphous solid water (P–ASW), amorphous solid water (ASW), and crystalline ice (CI). We prepared these types of water ice films by two different methods: collimated effusive H_2O beam method (direct deposition) and background deposition (backfilling). The

direct deposition was performed without a shutter in front of the pulse nozzle head while backfilling was conducted with the shutter. ASW was prepared by deposition of water on the polycrystalline Au substrate with (111) domains at 85 K with a pulsed molecular beam at the angle of incidence of 45 deg. The stagnation pressure was 20 Torr of neat water vapor. We prepared the P-ASW by backfilling at 90 K for 60 min on the polycrystalline Au substrate, which is characterized by a high surface area and low density. The porosity of P-ASW prepared by backfilling has been reported to be higher than the ASW prepared by direct deposition.[21-23] The difference is caused by the pore structures. Ikemiya and Gewirth observed the cross-sectional view of P-ASW on Au(111).[24] The H_2O islands have no atomically flat surfaces. The height of the planar monolayer water film is about 0.15 nm directly above the Au surface, while the cluster reaches to 0.45 nm. The H_2O clusters appear only atop the amorphous film and not on the bare Au(111) surface. Sato et al. estimated that the exposure of H_2O necessary to obtain 1 ML of ice film on an Au(111) substrate was 3 L at 90 K.[7] In our experiment, the exposure was 1800 L, which resulted in formation of 600 ML of H_2O on Au for background deposition, and more than 90 ML for direct adsorption by the molecular beam method. A polycrystalline ice film was prepared by annealing the ASW at $T = 130$ K for > 5 min for direct deposition. Annealing of ASW, which is a metastable state of ice, forms a polycrystalline ice (PCI) film. For backfilling deposition, polycrystalline ice (PCI) film is prepared by depositing water vapor at 130 K for 60 min and annealing for 25 min. Since Au(111) has a lattice mismatch to crystalline ice, deposition does not lead to an oriented epitaxial crystalline ice film.[29] On Au(111), sphere-like three dimensional nanoclusters were found.[30]

7.2.1.2 Adsorption of NO_2 on ice films. The chamber pressure was $P = 0.5 \times 10^{-8}$ Torr without gas injection and $1–10 \times 10^{-8}$ Torr with sample gas injection, which was monitored 50 cm away from the substrate with a cold cathode pressure gauge. Under these pressure conditions, a few monolayers of N_2O_4 were formed on the substrate. The number of monolayers depends on both the substrate temperature and the effective exposure of NO_2. Pulsed exposures of NO_2 do not form a completely uniform layer of

N_2O_4 on the substrate during 50 ms annealing time when the ice temperature was kept below the annealing temperature of N_2O_4. Sato et al. estimated that NO_2 exposure necessary for one monolayer of coverage of NO_2 was 4 L for crystalline ice film, 16 L for amorphous ice film and 2 L for the Au substrate. The ratio of surface area of the Au substrate to crystalline ice, and to amorphous ice is 1 to 2, and to 8. This ratio is corresponded to roughness factor of surface. In our previous experiment with the pulsed molecular beam of NO_2,[13] the intermittent exposure of NO_2 on a cooled Au substrate formed 5 ML of N_2O_4 at $P = 5 \times 10^{-8}$ Torr and $T = 80$ K. On both the Au substrate and the amorphous ice film, the signal intensity of NO increased linearly up to $P = 10 \times 10^{-8}$ Torr. Thus, we assume that an average coverage, in units of ML, of N_2O_4 on amorphous ice at 80 K can be approximated by using the chamber pressure P in units of 10^{-8} Torr. As the substrate temperature increases above 80 K, the coverage decreases due to lowering of the sticking probability as discussed below.

7.2.1.3 Photolysis of N_2O_4 adsorbed on ice films. Ultraviolet radiation from a pulsed excimer laser (Lambda Physik, COMPex) was used as a dissociation laser, which was incident 45° from the surface normal. Laser output intensities were typically set to $I_{laser} = 0.1$-0.5 mJ cm^{-2} at 193 nm, 1 mJ cm^{-2} at 248 nm, and 0.3 mJ cm^{-2} at 351 nm. Above these laser intensities signal intensities were saturated. Probe pulse laser light (0.1 mJ/pulse) intersected the flux of the photofragments (NO and O) at a distance, d, from the ice surface. d was changeable from 2 to 5 mm. For most of the experiments, d was set to 3 mm. The one-photon transition of $NO(A^2\Sigma - {}^2\Pi_{3/2}, v" = 0, J")$ was monitored by REMPI at 226 nm. $O({}^3P_j, j = 0,1,2)$ atoms were monitored by the two-photon resonant REMPI transition of $O({}^3D_{j'} - {}^3P_{j"})$ at 225.7-226.2 nm. The TOF spectra of NO and O were taken as a function of time delay, t, between the photolysis and probe laser pulses.

When TOF spectra were transformed to translational energy distributions, it was assumed that a) photofragments are detected at a point REMPI detection region, b) photofragments come into the gas phase from a round substrate area (diameter = 12 mm) with a $\cos^n\theta$ distribution where θ is the departing polar angle from the ice surface.

The distance between the detection region and the substrate was set to 3 mm. The diameter of the effective ice surface for photoirradiation was determined by a round slit in front of the chamber window for the dissociation laser beam. In order to simulate the TOF spectra, two different kinds of energy distributions were used; a Gaussian and a flux weighted Maxwell-Boltzmann. Conversion from the energy distribution to the TOF distribution was performed using the Jacobian.[31] However, it was found that the TOF distributions, which consist of a fast and a slow photofragments, did not fit properly to a Gaussian distribution. Hence, we used a composite of two Maxwell-Boltzmann distributions for both the fast and slow photofragments with translational temperatures, T_{trans}.

7.2.2 IRA and TPD measurement of adsorbed molecules on ice.

IRAS measurements were performed in an ultrahigh vacuum system which has been described previously.[32] An Au(111) single crystal (12 mm dia., 1.5 mm thick, 99.999% purity) substrate was cleaned by repeated Ar^+ sputtering at 800 K and annealing at 900 K. Ozone was used for surface cleaning. For IRAS measurements, the IR beam from a FTIR spectrometer (BIO-RAD FTS-155) was p-polarized by a wire grid polarizer, and then, was introduced into the vacuum chamber through a BaF_2 window with the incident angle of the IR beam of 85°. IRA spectra were recorded with 4 cm^{-1} resolution and 200 scans. Based on measurement of the IRAS absorption, the film thickness of N_2O_4 and water ice was estimated.

When water was deposited at temperatures below $T = 100$ K, amorphous ice film was formed on Au(111). After heating, the IRAS spectrum of the ice changed significantly. The bulk OH stretching band shifts to lower frequencies by more than 100 cm^{-1} at 140 K, while the bands of both free OH group and HOH bending decreases in intensity. The spectrum at 140 K is nearly identical to that of crystalline ice.[33] Since these spectral changes start at 120 K, the phase change of amorphous ice to crystalline ice occurs above 120 K. Thus, in the present experiment, an amorphous ice film was prepared by deposition of water on Au at <100 K. A crystalline ice film was prepared by annealing an amorphous ice film at 130 K for > 25 min and then cooling down to an appropriate

temperature T. Wang and Koel also measured IRA spectra of water films on Au(111).[8] The free OH peak decreased as the annealing temperature was increased, disappearing between 110 and 135 K. However, according to Jenniskens et al., the crystallization is not complete and the amorphous component is still intimately mixed with the cubic state in the crystallites.[34] The interfaces of crystallites were disordered and grain boundaries were formed. Sadtchenko et al. observed grain boundaries in crystalline ice films by observing uptake behavior of HCl.[28] Those researchers report that the ratio of the net surface area of the grain boundaries to the net open area of the crystalline ice film is quite low, and that the average size of the grain boundaries is small while their density is high. In this experiment, crystalline ice film was prepared by annealing the amorphous ice film at 130 K. Therefore, the structure of our crystalline ice film had some grain boundaries.

7.3 Results

7.3.1 TOF spectra and rotational spectra of NO($v = 0$, J) photofragments from N_2O_4 on amorphous ice at 80 K. 7.3.1.1 TOF spectra. TOF spectra of NO($v = 0$, Q-head) from the photodissociation of N_2O_4 multilayers on amorphous ice at 193, 248 and 351 nm were measured for various chamber pressures ($P = 1-10 \times 10^{-8}$ Torr) and T = 80 K. Vibrationally excited NO($v \geq 1$) was not observed. The translational and rotational energy distributions of NO photofragments are almost independent of the morphology of ice surface. When the TOF spectra of NO were transformed to translational energy frame, a very slow TOF component ($T_{trans} = 11 \pm 3$ K) appeared after $t = 30$ μs with a small contribution while t stands for TOF. This component was considered to be an artifact caused by the NO photofragments that were scattered once and bounced back to the REMPI detection region. Similar results concerning a very slow feature in TOF spectra has been reported.[9] However, this slowest component was not observed in the TOF spectrum for vibrationally excited NO($v = 3$) from the 193 nm photodissociation of N_2O_4 on Au.[13] Thus, the slowest component with $T_{trans} = 11 \pm 3$ K

was subtracted from the TOF spectrum of NO($v = 0$) from the photodissociation of N$_2$O$_4$ on ice.

7.3.1.2 Effect of dissociation wavelength. Typical TOF spectra $S(t)$ of NO are shown in Figure 7.1 for $P = 5 \times 10^{-8}$ Torr on amorphous ice. This pressure condition corresponds to an average number of layers of 0.6 ML of N$_2$O$_4$. The TOF spectrum is fitted to a composite of flux-weighted Maxwell-Boltzmann translational energy distributions $P_{MB}(E_t)$ with a different translational temperature T_{trans}, which is characterized by the average energy $<E_t> = 2k\ T_{trans}$:[31]

$$S(t,r) = r^3 t^{-4} \exp\{-mr^2/(2k_B T_{trans} t^2)\},\qquad(7.1)$$

$$P_{MB}(E_t) = (k_B T_{trans})^{-2}\ E_t \exp[-E_t/(k_B T_{trans})],\qquad(7.2)$$

where r is a flight length for photofragment, k_B is the Boltzmann constant and t the time of flight of the photofragment. The TOF distributions consist of a fast component T_{trans} = 850 ± 50 K and a slow component with T_{trans} = 70 ± 5 K(crystalline) and 55 ± 5 K(amorphous). The angular distribution of the photofragments from the substrate, $\cos^n\theta$, $n = 0$, was adopted for both components, because the value, $n = 0$, was best fitted to the TOF distributions. The value of n is very sensitive to the profile of $P_{MB}(E_t)$. No noticeable change was observed for the three different dissociation laser wavelengths, 193, 248 and 351 nm. For comparison purposes, the inset of Figure 7.1 shows a typical TOF spectrum of NO($v = 0$) from the 193 nm photodissociation of N$_2$O$_4$ adsorbed on a polycrystalline Au substrate, which consists of a fast component (a) with T_{trans} = 670 ± 70 K and a slow one (b) with T_{trans} = 80 ± 10 K. The relative contributions of the fast and slow ones depend on the dissociation laser wavelength. In addition, a higher vibrational state, NO($v = 3$), was also produced from N$_2$O$_4$ on Au at 193 and 248 nm.

7.3.1.3 Effect of N$_2$O$_4$ coverage. When the total TOF intensity was measured as a function of the chamber pressure P at 193 nm, the intensity increased linearly with P. Figure 7.2 shows TOF spectra for $P = 1\text{-}5 \times 10^{-8}$ Torr or 0.1-0.6 ML. The observed

spectra consist mostly of a slow component with T_{trans} = 70 ± 5 K(crystalline) and 55 ±

5 K(amorphous)with a small contribution (about 10 %) of a fast component with T_{trans} =

850 ± 50 K. Up to P = 5 × 10^{-8} Torr, no noticeable change in the TOF profiles was

observed. For comparison purposes the inset shows TOF spectra of NO(v = 0) from the

193 nm photodissociation of N_2O_4 adsorbed on a polycrystalline Au substrate, which

consists of the fast component (T_{trans} = 670 ± 70 K) and slow component (T_{trans} = 80 ±

10 K). On Au the contribution of the fast component increased as a function of the N_2O_4

coverage (P = 1-10 × 10^{-8} Torr). These results suggest that the fast component comes

from the photodissociation of the outermost adsorbate layer of the multilayered

N_2O_4.[35,36]

In the present ice surface photodissociation, the fast component with T_{trans} = 850 ± 50

K may be attributed due to the photodissociation of the outermost adsorbate layers of

the multilayered N_2O_4, hence the observed translational temperature T_{trans} = 850 ± 50 K

is close to what we observed for the Au substrate experiment T_{trans} = 670 ± 70 K.

7.3.1.4 Rotational spectra. Figure 7.3 shows a typical rotational spectrum of

NO($A^2\Sigma$, v' = 0, J' - $X^2\Pi_{3/2}$, v''=0, J'') from the 193 nm photodissociation of N_2O_4 on

amorphous ice at T = 80 K. This spectrum was measured for t = 13 μs. The rotational

temperature is estimated T_{rot} = 175 ± 25 K. Vibrationally excited NO($v \geq$ 1) was not

found. For 248 nm and 351 nm the results are essentially the same.

7.3.2 Effect of adsorbed states of N_2O_4 on TOF spectra at 193 nm. Figure 7.4

shows TOF spectra of NO(v = 0) from N_2O_4 on amorphous and crystalline ice films at T

= 120 K and P = 10 × 10^{-8} Torr. At this temperature and pressure, the thickness of the

N_2O_4 layer on amorphous, and crystalline is estimated to be 0.6 ML and 2.5 ML. There

is no noticeable difference between the two TOF spectra.

In a separate experiment, the physisorbed states of N_2O_4 (1-5 ML) on amorphous and

crystalline ice films were investigated with IRAS. N_2O_4 layer directly adsorbed on

crystalline ice film at 91 K exhibited both the 1303 cm^{-1} symmetric and 1750 cm^{-1}

asymmetric ONO stretching bands in comparable intensities. An IR transmission

spectrum of gas-phase N_2O_4 also shows a similar intensity profile. Thus, it is concluded

that the N_2O_4 layer directly adsorbed on the ice film should be randomly oriented on the ice surface. When N_2O_4 coverage exceeds a monolayer the symmetric band became discernible, which grew rapidly compared to slow increase of the asymmetric stretching band. Therefore, the ordered orientation with the N-N bond perpendicular to the surface is most likely for the N_2O_4 multilayered on crystalline ice. Thus, the annealing process from 91 K to 120 K converts disordered N_2O_4 to the ordered N_2O_4 on crystalline ice. When N_2O_4 adsorbed on amorphous ice at 91 K, the symmetric band increased in intensity upon heating, but the change was not as significant as observed for the crystallized ice. However, the asymmetric stretching band at 1750 cm^{-1} grows markedly on amorphous ice. These results imply that disordered N_2O_4 on amorphous ice undergoes rearrangement toward an orientation of the N-N bond parallel to the Au surface rather than the perpendicular one, because the amorphous ice surface has higher densities of free OH than the crystalline ice surface. This active surface can interact strongly with N_2O_4.[37]

7.3.3 Resonance enhanced multiphoton ionization detection of NO photofragments for temperature-programmed photodetachment spectroscopy.

Photodesorbed NO signal intensities for $P = 1.5 \times 10^{-8}$ Torr or 1.5 ML for Au, 0.8 ML for crystalline ice and 0.2 ML for amorphous ice of N_2O_4 were measured as a function of the substrate temperature T. We refer to this measurement as REMPI-TPPS, in which photodesorbed NO was probed by the REMPI method with increasing T at a rate of 2 K s^{-1}. Note that this TPD is different from an ordinary TPD in that the ice surface was exposed to an NO_2 molecular beam between the photodissociation laser shots. Figure 7.5 shows REMPI-TPPS spectra of NO from the 193 nm photodissociation of N_2O_4 on amorphous and crystalline ice films. For the amorphous ice, a monotonic decrease of the signal intensity was observed with increasing T. Since our IRAS measurement indicates that the phase change of amorphous ice to crystalline ice occurs at $T > 120$ K.[7], the signal intensity is not associated with the free OH concentration on the amorphous ice surface. The signal intensity is related to the sticking probability of NO_2 on water ice films, which is a function of the substrate temperature. The details of this are described

in the section of 1 of Discussion.

Figure 7.5 also shows a REMPI-TPPS spectrum for N_2O_4 on a polycrystalline Au substrate for $P = 1.5 \times 10^{-8}$ Torr. The REMPI-TPPS profiles of NO for the crystalline ice film and the Au are similar in the temperature range $T = 80$–150 K. These results suggest that the adsorbed states of N_2O_4 on the surfaces are similar. At > 150 K, these two TPD spectra are considerably different. For the crystalline ice film, the spectrum is characterized by two peaks of NO at 155 and 173 K. These peaks of NO correspond to those of H_2O at 157 and 187 K. Shown in the inset is a conventional TPD spectrum of N_2O_4 (1.6 ML) on a ice film.[7] The 157 K peak was assigned to ordinary H_2O desorption. The 187 K peak to adduct formation of H_2O with NO_2. Because N_2O_4 retained in the grain boundaries of the PCI films become free at the ice-sublimation temperature and the dissociation quantum yield increases. The signal enhancement, however, has another plausible explanation. That is, since water ice films are transparent at 193 nm, a) NO could be produced by the photodissociation of N_2O_4 trapped in the ice grain boundaries during the irradiation at 193 nm before the substrate temperature was increased up to 155 K, and b) NO thus produced and trapped in the grain boundaries were released into the gas phase upon melting the ice. In order to check if this process could have caused the 157 K peak of the REMPI-TPPS, the 193 nm irradiation was kept continuous from $T = 80$ to 150 K, and then, was turned off as marked by the arrow in Figure 7.5. When the substrate temperature was increased with the laser irradiation turned off, the 157 K peak did not appear. These results suggest that even if N_2O_4 trapped in the grain boundaries is irradiated at 193 nm, NO is not produced.

7.3.4 Dependence of signal intensity on polarization of the incident light. On amorphous and crystalline ice, the effect of polarization of the incident 193 nm laser light, s- and p-polarized light was measured for the signal intensity of NO as a function of various substrate temperatures ($T = 90, 100, 110,$ and 120 K) . The 193 nm laser light was linearly polarized by a stuck of quartz plates and the Is/Ip data were corrected for imperfect polarization of the laser light. For amorphous ice film, the Is/Ip ratios were unity, because adsorbed N_2O_4 are randomly oriented on the surface. However, on

crystalline ice films the ratios were $I_s/I_p = 0.78$ at T = 90 K, 0.71 at 100 K, 0.60 at 110 K, and 0.53 at 120 K. Since the electronic transition of N_2O_4 in the gas phase at 185 nm is along the N-N axis,[38-40] N_2O_4 tends to orient as the N_2O_4 layer is annealed at the higher temperatures. In this consideration, we neglect the standing wave effect at the water ice film surface by the reflected light from the Au substrate. This interference effect is a function of the ice film thickness as discussed previously.[18] Under the present experimental condition, the incident and reflected light are nearly in the same phase condition. These results are in agreement with the partially oriented adsorption state that is confirmed by our IRAS measurement described below.

7.3.5 Detection of $O(^3P_j)$ atoms. Two-photon REMPI signal of $O(^3P_j)$ atoms from N_2O_4 photodissociation at 193 and 248 nm for two different methods was found: direct deposition and backfilling, while not at 351 nm. It has been speculated that a part of the oxygen atoms produced on the ice surface remain trapped in the layers as reported by Sato et al.[32] The oxygen atoms that reach the Au substrate appeared as surface oxygen molecules in their TPD spectra. Compared to the $O(^3P_j)$ signals from N_2O_4 on Au,[13] the j-level of the $O(^3P_j)$ in the present experiment is mostly populated in $j = 2$.

7.3.6 IRA spectroscopic measurement. The IRA spectra of N_2O_4 on ice resemble those of N_2O_4 adsorbed on Au(111) except for the absence of the chemisorbed NO_2 band on Au at 1182 cm^{-1}.[32,41] When the thickness of crystalline ice was less than 4 ML, however, the band ascribed to the chemisorbed NO_2 was observed in the IRAS spectra, indicating that NO_2 or N_2O_4 can reach the Au surface through grain boundaries of the crystalline ice film. These results contrast with the fact that the chemisorbed NO_2 band was not observed for 1-ML coverage amorphous ice at 91 K.

The assignments of IRAS bands for N_2O_4 adsorbed on ice film were reported by Rieley et al.[6] The two bands at ~1300 cm^{-1} are attributed to the ONO symmetric stretching, and the three bands at ~1750 cm^{-1} to the ONO asymmetric stretching of N_2O_4 with D_{2h} symmetry. Similar to their results, the complete absence of the strong asymmetric stretching band of NO_2 at 1600-1650 cm^{-1}, shown in the inset of Figure 7.4, indicates the absence of NO_2 monomer, other NO_x, and HONO on ice. N_2O_4 isomers

such as D-isomers, O=N-O-NO$_2$ and nitrosonium nitrate, NO$^+$NO$_3^-$, were not detected in IRAS. When NO$_2$ was adsorbed on amorphous ice, similar results were obtained as on crystallized ice. Although various kinds of NO$_2$ species are formed in a low temperature inert gas matrix[42] and on substrates,[43-47] NO$_2$ adsorption on amorphous and crystalline ice films below 130 K results in formation of *pure* N$_2$O$_4$ (D$_{2h}$) layers. Since IRAS measurement cannot probe surface species that have no IR transition moments perpendicular to the Au surface, N$_2$O$_4$ may not be a sole species on the ice surface. However, search for other NO$_x$ species was unsuccessful even under the conditions of random orientation of N$_2$O$_4$. Thus, we think no other species exist on the ice surface. Hereafter, we use N$_2$O$_4$ as the surface species on and in the ice films.

Figure 7.6 shows IRA spectra of amorphous ice adsorbed on Au(111) at 93 K. The IRAS bands of a thin ice film have been assigned previously.[6,48] The sharp band at 3700 cm^{-1} is assigned to the stretching mode of free OH at the ice surface, the broad and strong band at 3389 cm^{-1} to OH stretching in bulk ice, and the weak band at 1654 cm^{-1} to HOH bending in bulk ice. The IRA spectrum resembles the IR transmission spectrum of a water film at room temperature except for the 3700 cm^{-1} band,[49] indicating that the ice film on Au(111) is an amorphous ice layer.

The interaction of the free OH groups of amorphous ice surfaces with adsorbed N$_2$O$_4$ can be examined by IRAS. The inset of Figure 7.6 shows intensity differences in IRA spectra before and after N$_2$O$_4$ adsorption at each temperature. Positive bands represent intensity reduction compared to the pure ice film case. The free OH band at 3700 cm^{-1} disappeared completely upon N$_2$O$_4$ adsorption at 100-115 K, because all free OH groups interact with adsorbed N$_2$O$_4$. In addition, the wide positive band centered at 3480 cm^{-1} indicates that bulk OH groups also interact with N$_2$O$_4$ at T = 100-115 K. Since the center frequency of this bulk OH band is higher than the peak frequency of the pure amorphous bulk ice band by ~ 100 cm^{-1}, N$_2$O$_4$ interacts with also the bulk ice. The loss of the free OH band upon N$_2$O$_4$ adsorption at T < 100 K was not observed for crystalline ice, but the loss at the bulk OH band occurred to some extent. This is because the crystalline ice surface has a low density of free OH groups and large amount of bulk

OH.

IRAS is selectively sensitive to a vibrational mode perpendicular to a reflective metal surface due to surface selection rules,[50] hence we can obtain information about molecular orientation with respect to surface.

Figure 6.6 shows, schematically, three possible orientations of N_2O_4 adsorbed on surface. For orientation (a) in which N_2O_4 is aligned with the N-N axis perpendicular to the ice-Au(111) surface., ONO symmetric stretching parallel to the N-N bond axis is IRAS active but not ONO asymmetric stretching. On the contrary, for orientation (b) in which N_2O_4 is aligned with the N-N axis parallel along the ice-Au(111) surface, the molecular plane is not on the surface. The asymmetric stretching perpendicular to the surface is active but not symmetric stretching. For orientation (c), in which the plane of N_2O_4 is on the ice-Au(111) surface, both vibrational modes are inactive. When the IRAS spectrum of the first-layer N_2O_4 on crystalline ice was measured, the 1300 cm^{-1} band of ONO symmetric stretching, which was ascribed to the first-layer N_2O_4 on ice surface,[15] has an intensity comparable to the 1750 cm^{-1} band of ONO asymmetric stretching. Since an IR transmission spectrum of gas-phase N_2O_4 exhibits both the symmetric and asymmetric ONO stretching bands in comparable intensities, the first-layer N_2O_4 on crystalline ice should be randomly oriented. With increasing N_2O_4 coverage for > 2.4 ML, the spectral intensity of the first-layer N_2O_4 increases with a small shift of the symmetric ONO stretching from 1270 cm^{-1} to 1280 cm^{-1}. In addition, the 1303 cm^{-1} band becomes discernible when N_2O_4 coverage exceeds a monolayer and becomes dominant at N_2O_4 coverage of 9.6 ML. This 1303 cm^{-1} symmetric band grows rapidly, compared to slow increase of the asymmetric stretching band at 1750 cm^{-1}. Therefore, orientation (a) is most likely for the multilayered N_2O_4 on crystalline ice.

After adsorption on crystalline and amorphous ice at T <100 K, the IRA spectra of N_2O_4 were measured when the substrate temperature was elevated up to 230 K. A significant difference of temperature behavior between amorphous and crystalline ice was observed. For N_2O_4 adsorbed on 5-ML crystalline ice, the intensity of the 1303 cm^{-1} band rapidly increases at >110 K and becomes maximum around 120 K, while that of

the asymmetric stretching bands decreases. These results suggest that the annealing process converts disordered N_2O_4 to ordered N_2O_4 of orientation (a) on crystalline ice. When N_2O_4 is adsorbed on 3-ML amorphous ice, the 1302 cm^{-1} band increases in intensity upon heating, but the change is not as significant as observed for the crystallized ice. However, the asymmetric stretching bands grow markedly on amorphous ice. These results imply that disordered N_2O_4 on amorphous ice undergoes rearrangement toward orientation (b) rather than orientation (a). Amorphous ice surface has higher densities of free OH and loosely bound H_2O molecules than crystalline ice surface. This active surface can interact strongly with N_2O_4.[37] Therefore, amorphous ice surface is favorable for orientation (b). Although Givan and Lowenschuss[47] reported that temperature cycling produces $NO^+NO_3^-$ from disordered N_2O_4 layers through D-isomers, our IRAS results show that neither $NO^+NO_3^-$ nor D-isomers are present in the N_2O_4 layer during annealing.

7.4 Discussion

7.4.1 Adsorption of N_2O_4 on water ice films. The upper surface of an amorphous ice film is characterized by free OH groups, which are detected by IRAS measurement at 3700 cm^{-1}. Graham and Roberts[51] reported that the difference in adsorption probabilities of HCl on amorphous and crystalline ice films is attributed to a lower coverage of dangling OH groups at the crystalline ice surface. Schaff and Roberts[37] investigated the difference in surface chemical behavior between amorphous and crystalline ice. Adsorption and desorption behaviors of polar and nonpolar molecules strongly depend on hydrogen donor ability of the ice surfaces. Porosity and surface area differences are not significant factors in the interaction of adsorbates with ice surfaces. They found two different desorption states of acetone on amorphous ice films; hydrogen-bonded and physisorbed ones.[52] Only the physisorbed one was observed on crystalline ice films. Their FTIRAS measurements show that the free OH coverage on the surface of crystalline ice is approximately one-sixth of that on amorphous ice. This may be the
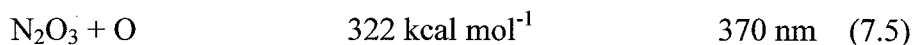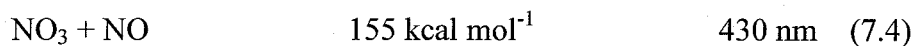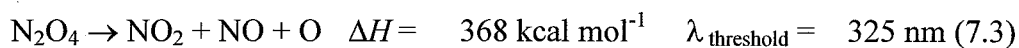
case for N_2O_4 on the ice films in the present experiment. As shown in the REMPI-TPPS spectra of Figure 7.5, the signal intensity on the crystalline ice is much weaker than on the amorphous ice. The substrate temperature dependence of the signal intensity for the amorphous ice may be explained by the decrease of the free OH group concentration on the surface. However, our IRAS measurements indicate the phase change of amorphous ice to crystalline ice occurs at $T > 120$ K.[7] Therefore, the decrease of the signal intensity at $T < 120$ K is not associated with the free OH concentration on the amorphous ice surface. Consequentially two other possible explanations are considered. One is the decrease of the sticking probability of N_2O_4 with increasing the substrate temperature. TPD experiments were performed after the ice surface was exposed with NO_2 gas (32 L) at each temperature (90, 100, 110 and 120 K).[53] The amount of N_2O_4 adsorbed at each temperature is proportional to the total intensity of the corresponding TPD spectrum. Due to the change in sticking probabilities of NO_2 on the ice films, the TPD intensity decreased as increasing the ice temperature. These results are in agreement with what was observed in our REMPI-TPPS experiment. The other possible explanation is the effect of adsorption states of NO_2 on photodissociation dynamics. Our IRAS measurements show the randomly-oriented N_2O_4 is photodissociated more efficiently than the ordered N_2O_4 because the ordered N_2O_4 after photoexcitation can be energetically relaxed by the neighboring N_2O_4. Thus, the photodissociation rate of the ordered N_2O_4 is suppressed. According to our IRAS measurements, the multiplayer N_2O_4 on crystalline ice forms an ordered layer, while the surface N_2O_4 is randomly oriented on ice. In addition, our IRAS measurements indicate the surface area of crystalline ice is approximately at least one-fourth of that of amorphous ice. Therefore, on crystalline ice, ordered N_2O_4 should exist more than on amorphous ice.

After the amorphous ice surface was exposed with NO_2 gas, a TPD spectrum was measured by Rieley et al.[6] and Sato et al.[7] The TPD peak of NO_2 in the inset of Figure 7.5 at 134 K is attributed to sublimation of physisorbed N_2O_4 on the ice film. At 214 K, another TPD peak of NO_2 appears. The 214 K peak comes from the fact that a part of N_2O_4 adsorbed on ice film is held in the bulk phase of ice, and then moves onto the Au

surface upon heating. The TPD of H_2O exhibits two peaks at 157 and 185 K. The 157 K is identical to that from pure $H_2O/Au(111)$, while the 185 K peak is due to the adduct formation of H_2O with NO_2. When the thickness of crystalline ice was less than 4 ML, the band ascribed to the NO_2 chemisorbed directly on Au was observed in IRAS, indicating that NO_2 or N_2O_4 can reach the Au surface through grain boundaries of the crystalline ice film.[7] In the present experiment, the ice film was so thick that N_2O_4 were retained only in the ice bulk. Thus, REMPI-TPPS spectra on the ice films showed no peak at 214 K, while there is a wide peak at 214 K for TPD on the Au.

Our IRAS measurements revealed a) NO_2 adsorb on amorphous and crystalline ice surfaces as N_2O_4 with D_{2h} symmetry, and b) neither N_2O_4 isomers such as D-isomers nor NO_x (x = 1, 2, and 3) species are observed on ice at 90-190 K.[7]

7.4.2 Primary processes of N_2O_4 photodissociation on ice. 7.4.2.1 Photodissociation at 193 and 248 nm. The following channels are plausible primary processes from an energetic point of view. The IRAS measurement shows no presence of NO_3 or N_2O_3 on the Au surface during the irradiation at 260-420 nm.[32] Thus, process (1) is the most plausible process for the formation of NO for the 193 nm photodissociation of N_2O_4 on the ice film:

$$N_2O_4 \rightarrow NO_2 + NO + O \quad \Delta H = \quad 368 \text{ kcal mol}^{-1} \quad \lambda_{threshold} = \quad 325 \text{ nm} \quad (7.3)$$

$$NO_3 + NO \quad\quad\quad 155 \text{ kcal mol}^{-1} \quad\quad\quad 430 \text{ nm} \quad (7.4)$$

$$N_2O_3 + O \quad\quad\quad 322 \text{ kcal mol}^{-1} \quad\quad\quad 370 \text{ nm} \quad (7.5)$$

The energetics are calculated from the gas-phase thermodynamic values. The photon energies at 193 and 248 nm are above the threshold energy of reaction 7.3. The linear increase of the NO signal intensity for 193 nm suggests the photodissociation of the outermost adsorbate layer.

7.4.2.2 Photodissociation at 351 nm. The photon energy of 351 nm is below the

gas-phase thermodynamic threshold of 325 nm for the formation of NO in reaction 7.3. The formation of NO from N_2O_4 on metal surfaces at 351 nm, which is attributed to the electron-mediated process, was reported by Hasselbrink et al.[12] and Sato et al.[32] In their experiment, a fall-off of the signal intensity was observed for the high coverage region. Their results indicate that the photoproducts only from the layers near the N_2O_4-Au interface are released by the irradiation at ~350 nm. Since electron transfer from a metal surface through the water layer is prohibited,[54] it is unlikely in the present experiment that the dissociation takes place via surface mediated processes. Since the signal intensity of NO increased linearly with the pressure P in the present experiment, the photoproducts come from the outermost and near-outermost layers.

Rieley et al.[9] investigated the photodissociation of N_2O_4 multilayers on water layers (30 ML)/Cu at 355 nm. The direct photoabsorption process of N_2O_4 generates NO_2 due to N-N bond scission. No desorption of N_2O_4 occurred at this wavelength. NO_2 desorption followed by its one-color dissociation process at the probe laser wavelength 226 nm could give the signal in the present experiment. However, we can eliminate this possibility, because a) $O(^3P_j)$ was not detected in our experiment and b) abrupt increase of the NO signal intensity was not found upon evaporation of NO_2 at 134 K (see the inset of Figure 7.5).

Involvement of HNO_3 and HONO on the ice surface can be eliminated because our IRAS measurement showed no presence of these species, although Wang and Koel [55] reported that a small amount of these species were formed from the co-adsorbed layers of NO_2 on H_2O below 145 K. Only at room temperature, NO_2 on H_2O suspended in silica is easily converted to these species.[56, 57] Since our experimental temperature is as 80-120 K, N_2O_4 is only species involved in the present photolysis.

A possible explanation for the formation of NO via reaction 7.3 at 351 nm is the change in the electronic structures of N_2O_4 upon adsorption on ice. The formation of hydrogen bonds with free OH groups may reduce the effective bond energy for N_2O_4 to dissociate into NO_2 + O + NO. This hydrogen bonding induces the change in the electronic structure. Actually, the dissociation cross section of N_2O_4 prepared on water

ice at 351 and 355 nm is larger than the gas phase one by an order of magnitude.

7.4.3 Effect of adsorption states of N_2O_4 on dissociation dynamics at 193 nm. The adsorption state of N_2O_4 is "random" on amorphous ice, and partially "ordered" on crystalline ice. As shown in Figure 7.1, however, we found no appreciable difference in the TOF spectra for the two different adsorption states of N_2O_4, since the ice film serves as a thermal bath to relax the translational and internal energies of nascent NO and $O(^3P_j)$. As a reference experiment, N_2O_4 (5 ML) adsorbed on the Au(111) substrate was irradiated at 193, 248 and 351 nm.[13] The effect of the dissociation wavelengths and the adsorption states of N_2O_4 on the Au was obvious on the TOF spectra. At 193 nm, the fast ($T_{trans} = 670 \pm 70$ K) component was dominant, compared to the slow ones ($T_{rans} = 80 \pm 10$ K). In addition, the abundance of the $j = 0$ level in the $O(^3P_0)$ photofragment was appreciable. The 670 ± 70 K component was attributed to the photodissociation of the outermost adsorbate layers, while the 80 ± 10 K components to those of the inner layers or the surface layer attached to Au. On the ice films, the energy distributions of the NO and O are totally relaxed. A slow component with $T_{trans} = 70 \pm 5$ K(crystalline), or 55 ± 5 K(amorphous) for ice cooled at 80 K is dominant. The rotational temperature is also as low as 175 K. The j level in the $O(^3P_j)$ photofragments is mostly populated in the lowest level $j = 2$. Since the lower coverage of N_2O_4 on ice gives only the slow component, this signal comes from the photodissociation of the N_2O_4 attached directly on ice surface and its translational temperature corresponds to the ice temperature. The fast component comes from the photodissociation of the outermost and the near-outermost layers. Even when the outermost layer is dissociated, efficient relaxation induced by the ice layers slowed down the TOF distributions.
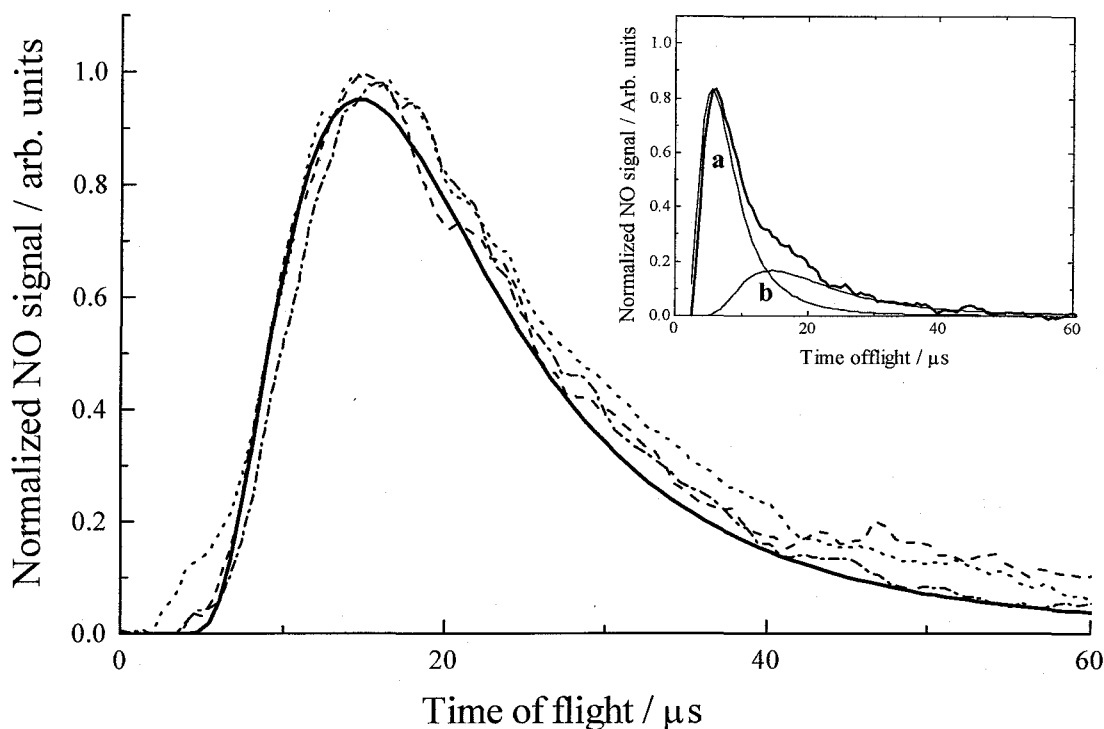
Figure 7.1 Time-of-flight (TOF) spectra of $NO(A^2\Sigma, v' = 0, J' - X^2\Pi_{3/2}, v''=0$, Q-head) from the photodissociation of N_2O_4 on an amorphous ice film as a function of delay time between dissociation and probe laser pulses. Dissociation laser wavelengths λ = 193 nm (solid line), 248 nm (broken line) and 351 nm (dotted line). Ice temperature T = 80 K and chamber pressure P = 5 × 10^{-8} Torr. This pressure corresponds to N_2O_4 coverage of about 0.6 ML. The smooth solid curves correspond to a Maxwell-Boltzmann energy distribution defined in Eq. 7.1 with T_{trans} = 110 K. The inset shows a REMPI-TOF spectrum of $NO(v = 0)$ from the 193 nm photodissociation of N_2O_4 multilayer adsorbed on Au, which consists of two components a (T_{trans} = 600 K) and b (T_{trans} = 85 K). The substrate temperature and the chamber pressure are the same.
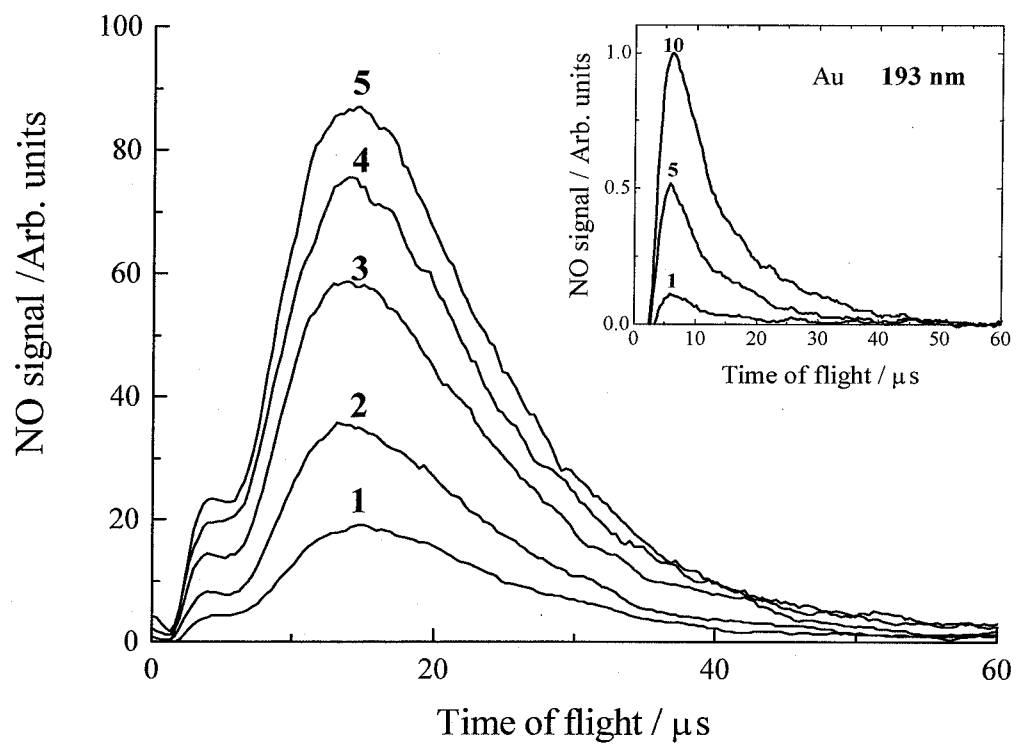
Figure. 7.2 Effect of chamber pressure, P, on time-of-flight spectra of NO($v = 0$, Q-head) from the photodissociation of N_2O_4 on amorphous ice at 193 nm. Ice temperature $T = 80$ K. The numbers indicated are the chamber pressures in units of 10^{-8} Torr.

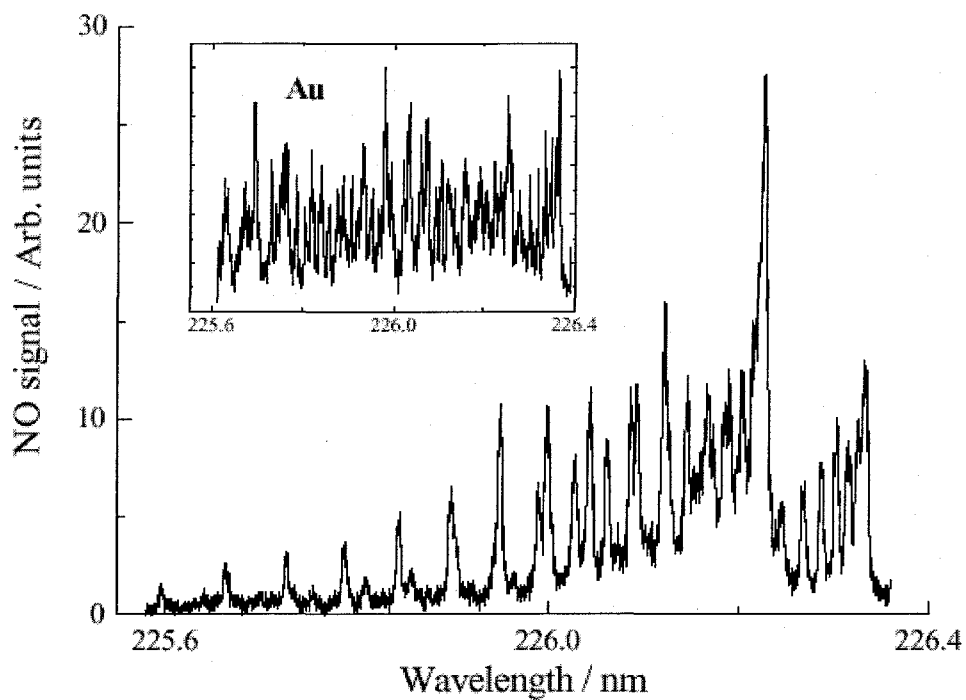Figure 7.3 Rotational spectra of NO($A^2\Sigma$, $v' = 0$, J' - $X^2\Pi_{3/2}$, $v''=0$, J'') from the photodissociation of N_2O_4 on amorphous ice at 193 nm. TOF position $t = 5$ μs, $T = 85$ K and $P = 5 \times 10^{-8}$ Torr. (0.6 ML of N_2O_4).
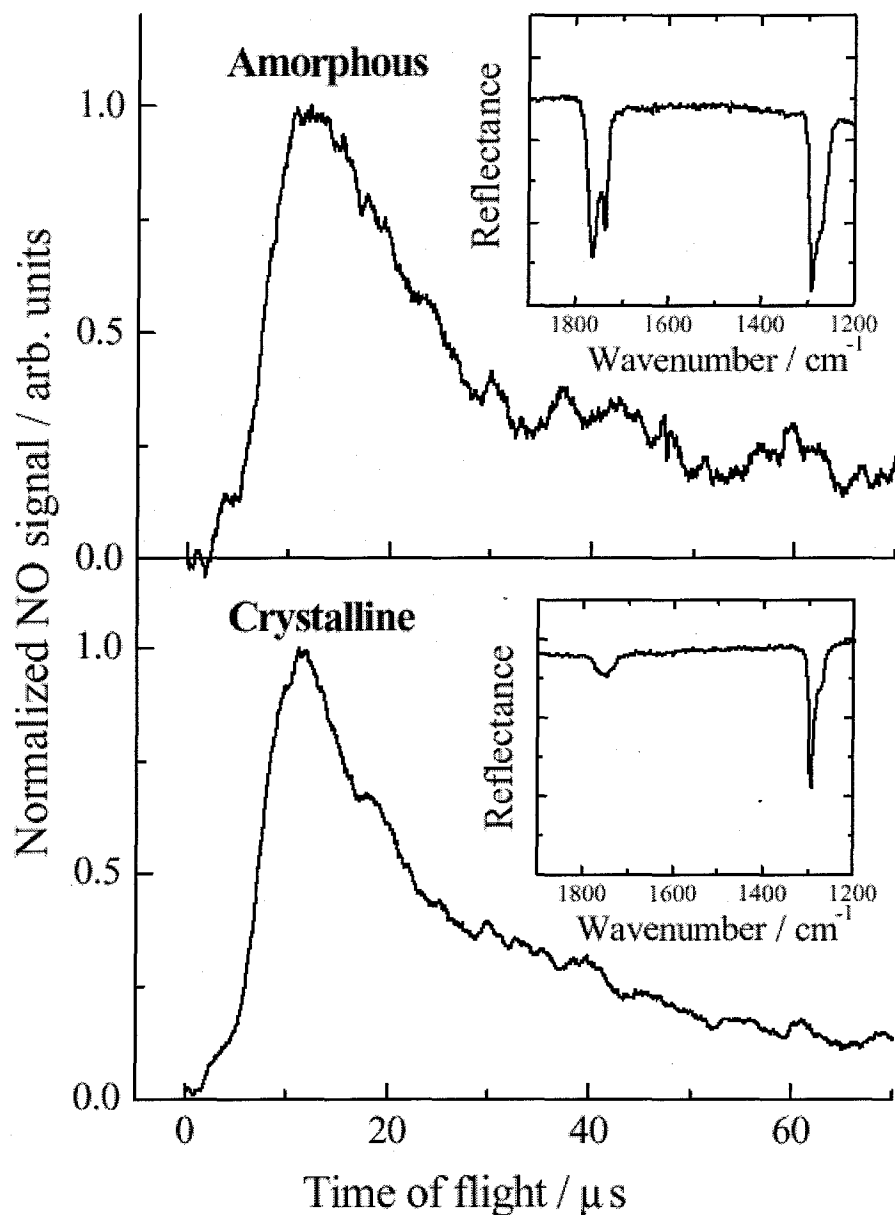
Figure 7.4 Time-of-flight (TOF) spectra of NO(X, $v = 0$, Q-head) from the 193 nm photodissociation of N_2O_4 adsorbed on amorphous and crystalline ice films. $T = 120$ K and $P = 10 \times 10^{-8}$ Torr. The insets show the infrared reflection absorption spectra of N_2O_4 on 3 ML amorphous and 5 ML crystalline ice films at $T = 120$ K. The ONO symmetric band appears at 1303 cm^{-1} and the asymmetric stretching band at 1750 cm^{-1}.
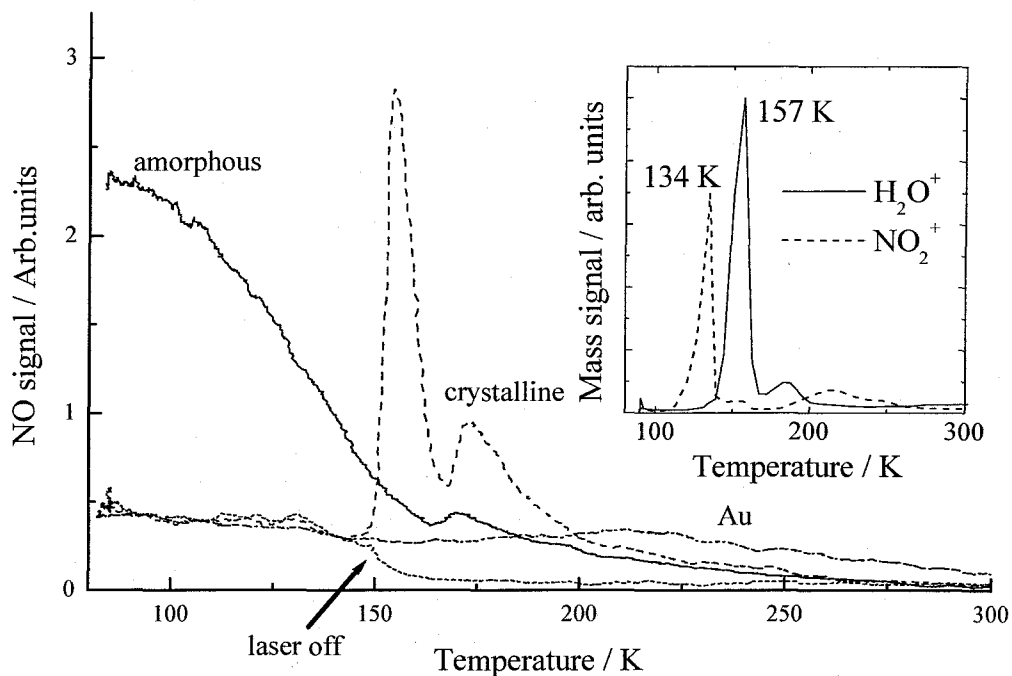
Figure 7.5 The REMPI signal intensities of NO(v=0, Q-head) from N_2O_4 on amorphous and crystalline ice films for temperature-programed photodetachment spectroscopy (TPPS). $P = 1.5 \times 10^{-8}$ Torr, $\lambda = 193$ nm and $I_{laser} = 1.5$ mJ cm^{-2}pulse^{-1}. The substrate temperature was increased at a rate of 2 K s^{-1}. The curves of the inset shows a conventional temperature programmed desorption spectrum of NO_2 and H_2O from N_2O_4 (1.6 ML) on ice film without photon irradiation, using a mass spectrometer.[32] The allow (laser off) shows the position at which the laser light was shut off for the crystalline film. See text for details.
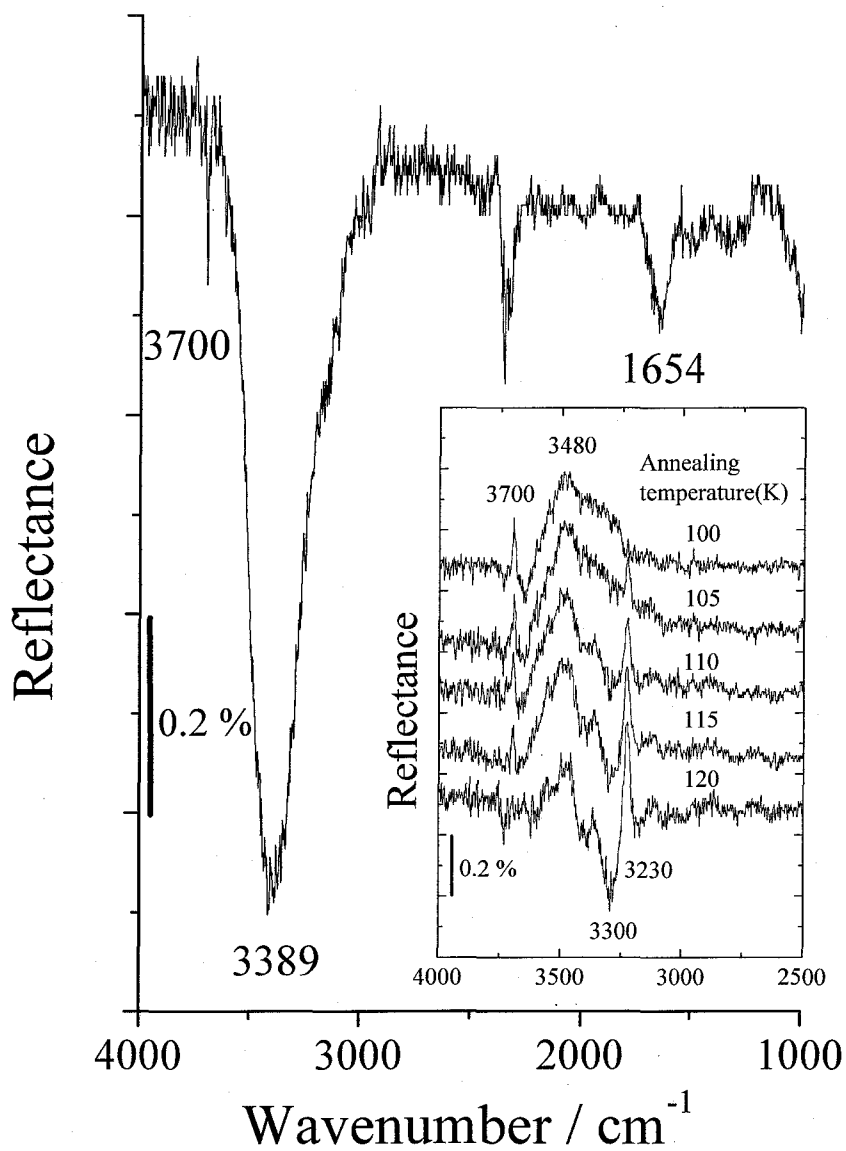
Figure 7.6 IR reflection absorption spectra of H_2O adsorbed on an Au(111) surface at 93 K for 4 L exposure. The inset shows a difference spectrum in the OH stretching region upon NO_2 adsorption on amorphous ice at 100 K. The difference spectrum is referred to that taken for bare ice. The coverages of H_2O and N_2O_4 were 5 and 1.5 ML, respectively.

References

(1) Nishi, N.; Shinohara, H.; Okuyama, T. *J. Chem. Phys.* **1984**, *80*, 3898.

(2) Pursell, C. J.; Conyers, J.; Denison, C. *J. Phys. Chem.* **1996**, *100*, 15450.

(3) Graham, J. D.; Roberts, J. T.; Brown, L. A.; Vaida, V. J. *J. Phys. Chem.* **1996**, *100*, 3115.

(4) Chaabouni, H.; Schriver-Mazzuoli, L.; Schriver, A. *Low Temp. Phys.* **2000**, *26*, 712.

(5) Ball, D. W. *Chem. Phys. Lett.* **1999**, *312*, 306.

(6) Rieley, H.; McMurray, D. P.; Haq, S. *J. Chem. Soc. Faraday Trans.* **1996**, *92*, 933.

(7) Sato, S.; Yamaguchi, D.; Nakagawa, K.; Inoue, Y.; Yabushita, A.; Kawasaki, M. *Langumuir* **2000**, *16*, 9533.

(8) Wang, J.; Koel, B. E. *Surf. Sci.* **1999**, *436*, 15.

(9) Rieley, H.; Colby, D. J.; McMurray, D. P.; Reeman, S. M. *J. Phys. Chem. B* **1997**, *101*, 4982.

(10) Rieley, H.; Colby, D. J.; McMurray, D. P.; Reeman, S. M. *Surf. Sci.* **1997**, *390*, 243.

(11) Dixon-Warren, St. J.; Jackson, R. C.; Polanyi, J. C.; Rieley, H.; Shapter, J. G.; Weiss, H. *J. Phys. Chem.* **1992**, *96*, 10983.

(12) Hasselbrink, E.; Jakubith, S.; Nettesheim, S.; Wolf, M.; Cassuto, A.; Ertl, G. *J. Chem. Phys.* **1990**, *92*, 3154.

(13) Senga, T.; Yabushita, A.; Inoue, Y.; Kawasaki, M.; Sato, S. *Bull. Chem. Soc. Jpn.* **2001**, *74*, 689.

(14) Honrath, R. E.; Peterson, M. C.; Guo, S.; Dibb, J. E.; Shepson, P. B., Campbell, B. *Geophys. Res. Lett.*, **1999**, *26*, 695.

(15) Honrath, R. E.; Guo, S.; Peterson, M. C.; Diiobak, M. P.; Dibb, J. E.; Arsenault, M. A. *J. Geophys. Res.* **2000**, *105*, 24183.

(16) Dubowski, Y.; Colussi, A. J.; Hoffmann, M. R. *J. Phys. Chem. A* **2001**, *105*, 4928.

(17) Dubowski, Y.; Colussi, A. J.; Boxe, C.; Hoffmann, M. R. *J. Phys. Chem. A* **2002**, *106*, 6967.

(18) Yabushita, A.; Inoue, Y.; Senga, T.; Kawasaki, M.; Sato, S. *J. Phys. Chem. B* **2002**,

106, 3151.

(19) Masson, D. P.; Lanzendorf, E. J.; Kummel, A. C. *J. Chem. Phys.* **1995**, *102*, 9096.

(20) Kawasaki, M. *Appl. Surf. Sci.*, **1998**, *135*, 1159.

(21) Kimmel, G. A.; Stevenson, K.P.; Dohnálek, Z.; Smith, R. S.; Kay, B. D. *J. Chem. Phys.* **2001**, *114*, 5284.

(22) Kimmel, G. A.; Dohnálek, Z.; Stevenson, K.P.; Smith, R. S.; Kay, B. D. *J. Chem. Phys.* **2001**, *114*, 5295.

(23) Stevenson, K. P.; Kimmel, G. A.; Dohnálek, Z.; Smith, R. S.; Kay, B. D. *Science* **1999**, *283*, 1505.

(24) Ikemiya, N.; Gewirth, A. A. *J. Am. Chem. Soc.* **1997**, *119*, 9919.

(25) Zondlo, M. A.; Onasch, T. B.; Warshawsky, M. S.; Tolbert, M. A.; Mallick, G.; Arentz, P.; Robinson, M. S. *J. Phys. Chem. B* **1997**, *101*, 10887.

(26) Sadtchenko, V.; Knutsen, K.; Giese, C. F.; Gentry, W. R. *J. Phys. Chem. B* **2000**, *104*, 2511.

(27) Sadtchenko, V.; Knutsen, K.; Giese, C. F.; Gentry, W. R. *J. Phys. Chem. B* **2000**, *104*, 4894.

(28) Sadtchenko, V.; Giese, C. F.; Gentry, W. R. *J. Phys. Chem. B* **2000**, *104*, 9421.

(29) Sieger, M. T.; Orlando, T. M. *Surf. Sci.* **2000**, *451*, 97.

(30) Smith, R. S.; Huang, C.; Wong, E. K. L.; Kay, B. D. *Surf. Sci.* **1996**, *367*, L13.

(31) Zimmermann, F. M.; Ho, W. *Surf. Sci. Rep.* **1995**, *22*, 127.

(32) Sato, S.; Senga, T.; Kawasaki, M. *J. Phys. Chem. B* **1999**, *103*, 5063.

(33) Tolbert, M. A.; Middlebrook, A. M.; *J. Geophys. Res.* **1990**, *95*, 22423.

(34) Jenniskens, P.; Banham, S. F.; Blake, D. F.; McCoustra, M. R. S. *J. Chem. Phys.* **1997**, *107*, 1232.

(35) Kawasaki, M.; Sato, H.; Nishi, N. *J. Appl. Phys.* **1989**, *65*, 792.

(36) Zhao, W.; Kim, C.; White, J. M. *Surf. Sci.* **2000**, *451*, 267.

(37) Schaff, J. E.; Roberts, J. T. *J. Phys. Chem.* **1996**, *100*, 14151.

(38) Mason, J. *J. Chem. Soc. Dalton Trans.* **1985**, *1*, 19.

(39) Sisk, W. N.; Miller, C. E.; Johnston, H. S. *J. Phys. Chem.* **1993**, *97*, 9916.

(40) Kawasaki, M.; Kasatani, K.; Sato, H.; Shinohara, H.; Nishi, N. *Chem. Phys.* **1983**, *78*, 65.

(41) Bartram, M. E.; Koel, B. E. *Surf. Sci.* **1989**, *213*, 137.

(42) Bandow, H.; Akimoto, H.; Akiyama, S.; Tezuka, T. *Chem. Phys. Lett.* **1984**, 111, 496.

(43) Fateley, W. G.; Bent, H. A.; Crawford, Jr. B. *J. Chem. Phys.* **1939**, *31*, 204.

(44) Hisatsune, I. C.; Devlin, J. P.; Wada, Y. *J. Chem. Phys.* **1960**, *33*, 714.

(45) Varetti, E. L.; Pimentel, G. C. *J. Chem. Phys.* **1971**, *55*, 3813.

(46) Givan, A.; Loewenschuss, A. *J. Chem. Phys.* **1989**, *90*, 6135.

(47) Givan, A.; Loewenschuss, A. *J. Chem. Phys.* **1989**, *91*, 5126.

(48) Horn, A. B.; Koch, T.; Chester, M. A.; McCoustra, M. R. S.; Sodeau, J. R. *J. Phys. Chem.* **1994**, *98*, 946.

(49) Ataka, A.; Yotsuyanagi, T.; Osawa, M. *J. Phys. Chem.* **1996**, *100*, 10664.

(50) Greenler, R. G.; Rahn, R. R.; Schwartz, J. P. *J. Catal.* **1971**, *23*, 42.

(51) Graham, J. D.; Roberts, J. T. *Geophys. Res. Lett.* **1995**, *22*, 251.

(52) Schaff, J. E.; Roberts, J. T. *Langmuir* **1998**, *14*, 1478.

(53) Sato, S. (unpublished data)

(54) Cowin *J. Phys. Chem.* **1989**, *91*, 1937.

(55) Wang, J.; Koel, B.E. *J. Phys. Chem.* **1998**, *102*, 8573.

(56) Goodman, A. L.; Underwood, G. M.; Grassian, B. H. *J. Phys. Chem.* **1999**, *103*, 7217.

(57) Barney, W. S.; Finlayson-Pitts, B. J. *J. Phys. Chem.* **2000**, *104*, 7217.

Chapter 8

Summary

In this thesis, ultraviolet photodissociation dynamics of small molecules adsorbed on water ice surfaces have been studied by measuring TOF spectra of the state resolved photofragments. The adsorbed states of ice on an Au substrate and small molecules on the ice films were investigated by IRA and TPD spectroscopic measurement.

In chapter 4, interaction of surface-adsorbed Cl_2 molecules and a water ice surface has been investigated for amorphous and crystalline water ice, observing the photodissociation dynamics of Cl_2 at 351 nm. The photodissociation mechanism of Cl_2 is independent of photolysis laser intensity, adsorbate coverage, and the states of ice films. However, the dissociation quantum yield on an amorphous ice film is much less than on a crystalline ice film, because the free OH groups on an amorphous ice surface interact with Cl_2. The measurement of the polarization effect of the dissociation laser beam supports the strong influence of the morphology on the dissociation dynamics of Cl_2 adsorbed on water ice films. The formation of HCl molecules from the reaction of the photofragment Cl atoms with water molecules was not confirmed in the present experiment.

In chapter 5, Cl_2 and $CFCl_3$ are adsorbed at 86-99 K on two different states of ice surfaces, porous amorphous solid water (P-ASW) and polycrystalline ice (PCI). $Cl(^2P_{3/2})$ and $Cl^*(^2P_{1/2})$ photofragments have been measured to investigate the dissociation mechanisms of Cl_2 at 300-414 nm and $CFCl_3$ at 193 nm as a function of photolysis laser intensity, coverage of the adsorbates, and the states of the ice surfaces. The kinetic energy distributions of the chlorine atom photofragments are explained by a combination of the direct photodissociation process and relaxation processes. For $CFCl_3$ the absorption cross sections were similar on both P-ASW and PCI surfaces. The relative quantum yield for the formation of Cl on P-ASW is, however, weaker less than on PCI by an order of magnitude. The electronic quenching occurs efficiently for $CFCl_3$

due to nucleation of the adsorbates. The spin-orbit branching ratio of the $Cl(^2P_{3/2})$ and $Cl^*(^2P_{1/2})$ photofragments on PCI is essentially the same as that in the gas phase photodissociation, suggesting a weak interaction of $CFCl_3$ with surface water molecules. For Cl_2, the branching ratios at 300-414 nm are completely different from those reported in the gas phase photodissociation. Along with those results, the fact that the signal intensity on P-ASW is weaker than on PCI by an order of magnitude suggests a relatively strong interaction between chlorine molecules and the OH groups of the surface water molecules on P-ASW.

In chapter 6, the adsorption states of NO_2 over amorphous and crystalline water-ice films formed on an Au(111) surface have been studied in an ultrahigh vacuum system by the TPD technique and IR absorption-reflection spectroscopy (IRAS).The conclusion is specified below.

1. An amorphous ice film was prepared by deposition of gas-phase water on an Au(111) surface at <100 K, and a crystalline ice film was prepared at 140 K, followed by annealing at the same temperature for 10 min. The amorphous and the crystalline ice surfaces are characterized by rich and poor densities of free OH, respectively.

2. TDS from NO_2 adsorbed on amorphous and crystalline ice shows two H_2O desorption peaks at 157 and 185 K, the former being attributed to H_2O adsorbed on the Au surface and the latter to the decomposition of a H_2O-NO_2 adduct. The same TDS exhibits two NO_2 desorption peaks at 134 and 214 K, the former being ascribed to physisorbed N_2O_4 on the ice and the latter to NO_2 chemisorbed on the Au surface. Chemisorbed NO_2 is produced from the H_2O-NO_2 adduct. No difference between TDS features for amorphous and crystalline ice suggests that interaction of free OH with NO_2 is not related with formation of the NO_2-H_2O adduct.

3. IRAS shows that NO_2 is adsorbed as N_2O_4 with D_{2h} symmetry on crystalline and amorphous ice, and no other NO_x ($X = 1, 2,$ and 3) species were detected. On crystalline ice, a disordered N_2O_4 layer is formed within ~5 ML, while ordered N_2O_4 with its N-N bond axis perpendicular to the surface dominates at > >5 ML. On amorphous ice, a new IRAS band of N_2O_4 is observed in the ONO symmetric stretching region but is not

characterized well. N_2O_4 and/or NO_2 can reach to the Au surface through the grain boundaries of a <10 ML crystalline ice film, but can not pass through the amorphous ice film even at 1 ML.

4. All free OH and part of the bulk OH interact with adsorbed N_2O_4. H_2O molecules interacting with N_2O_4 would be surface H_2O molecules that are weakly bound to the bulk ice.

5. When NO_2 is co-adsorbed with H_2O on Au(111), O_2 desorption occurred in TPD at ~510 K. Since an Au(111) surface is catalytically active for NO_2 decomposition at 180-240 K, coadsorbed H_2O makes the NO_2 desorption temperature higher than 180 K by forming the H_2O-NO_2 adduct.

In chapter 7, the photodissociation dynamics of N_2O_4 adsorbed on amorphous and polycrystalline water ice films at 80-140 K was investigated at 193, 248 and 351 nm by measuring the REMPI-TOF spectra of NO($v = 0$) and O($^3P_2$). The adsorbed states of ice on an Au substrate and N_2O_4 on the ice films were investigated by IRA and TPD spectroscopic measurement. The conclusion is specified below.

1. At 193, 248 and 351 nm, the NO photofragment comes from the dissociation path: N_2O_4 + hv $\rightarrow$ NO_2 + NO + O.

2. The ice film acts as an efficient thermal bath for energy relaxation processes. Thus, the photofragments have almost the same translational and internal energy distributions for the dissociation laser wavelengths at 193, 248 and 351 nm. There is no noticeable change in the dissociation dynamics of N_2O_4 on amorphous and crystalline ice films although there is a difference in the adsorption states of N_2O_4.

3. The TOF distribution of NO($v = 0$) consists of the translational temperatures, 850 ± 50 K and T_{trans} = 70 ± 5 K(crystalline) and 55 ± 5 K(amorphous). The former component is assigned to the fragment directly released to the gas phase from the outermost adsorbate layer of N_2O_4, while the latter to that from the inner layers. Compared to the previous study on the N_2O_4 photodissociation on an Au substrate the present results on ice suggest an efficient relaxation process on the ice films.

4. The amorphous ice surface is characterized by free OH groups on its surface, while

the crystalline ice film by much less OH on its surface and grain boundaries in the bulk. Temperature-programmed photodetachment measurement and IRA measurement show the substrate temperature dependence of the signal intensity for both ice films. The surface area and the sticking probability decrease as the substrate temperature increasing. The yield of NO from N_2O_4 adsorbed on the polycrystalline ice (PCI) film peaks at 157 K. This abrupt increase of the photodissociation yield is due to loss of the electronic quenching effect for the trapped N_2O_4 in the grain boundaries of the PCI film.

Acknowledgements

List of Publications

Chapter 4

Akihiro Yabushita, Yoshihiko Inoue, Takehito Senga, Masahiro Kawasaki, Shinri Sato "Photodissociation of Chlorine Molecules Adsorbed on Amorphous and Crystalline Water Ice Films" *J. Phys. Chem. B*, **2002**, *106*, 3151-3159

Chapter 5

Akihiro Yabushita, Masahiro Kawasaki, Shinri Sato "Ultraviolet Photodissociation Dynamics of Cl_2 and $CFCl_3$ Adsorbed on Water Ice Surfaces" *J. Phys. Chem. A*, (in press)

Chapter 6

Shinri Sato, Dai Yamaguchi, Kikuko Nakagawa, Yoshihiko Inoue, Akihiro Yabushita, Masahiro Kawasaki "Adsorption States of NO_2 and N_2O_4 Over Water Ice Films Formed on Au(111)" *Langmuir*, **2000**, *16*, 9533-9538

Chapter 7

Akihiro Yabushita, Yoshihiko Inoue, Takehito Senga, Masahiro Kawasaki, Shinri Sato "Photodissociation of N_2O_4 Adsorbed on Amorphous and Crystalline Water Ice Films." *J. Phys. Chem. A*, (submitted)

The following papers are not included in this thesis

Takehito Senga, Akihiro Yabushita, Yoshihiko Inoue, Masahiro Kawasaki, Shinri Sato "Photodissociation of N_2O_4 Adsorbed on Polycrystalline Au(111)" *Bull. Chem. Soc. Jpn.*, **2001**, *74*, 689-697

Keiichi Yokoyama, Junkei Kou, Akihiro Yabushita, Hidetaka Yamada, Yuji Fukuda, Makoto Aoyama, Yutaka Akahane, Norihiro Inoue, Hideki Ueda, Koichi Yamakawa, Atsushi Yokoyama "Feedback Control of Acousto-optic Programmable Dispersive Filter" *Opt. Commun.*, (submitted)